Structures Research
Report 2016/114986-
114987

University of Florida
Civil and Coastal Engineering

University of Florida
Civil and Coastal Engineering

Final Report November 2016

Scaling and validation of breakaway connection for multi-post ground signs

Principal investigator:
Gary R. Consolazio, Ph.D.

Graduate research assistant:
Douglas G. Innocent

Department of Civil and Coastal Engineering
University of Florida
P.O. Box 116580
Gainesville, Florida 32611

Sponsor:
Florida Department of Transportation (FDOT)
William Potter, P.E. – Project manager

Contract:
UF Project Nos. 00114986 & 00114987
FDOT Contract No. BDV31-977-24

DISCLAIMER

The opinions, findings, and conclusions expressed in this publication are those of the authors and not necessarily those of the State of Florida Department of Transportation.

SI (MODERN METRIC) CONVERSION FACTORS

*APPROXIMATE CONVERSIONS **TO** SI UNITS*

SYMBOL	WHEN YOU KNOW	MULTIPLY BY	TO FIND	SYMBOL
LENGTH				
in	inches	25.4	millimeters	mm
ft	feet	0.305	meters	m
yd	yards	0.914	meters	m
mi	miles	1.61	kilometers	km
AREA				
in^2	square inches	645.2	square millimeters	mm^2
ft^2	square feet	0.093	square meters	m^2
yd^2	square yard	0.836	square meters	m^2
ac	acres	0.405	hectares	ha
mi^2	square miles	2.59	square kilometers	km^2
VOLUME				
fl oz	fluid ounces	29.57	milliliters	mL
gal	gallons	3.785	liters	L
ft^3	cubic feet	0.028	cubic meters	m^3
yd^3	cubic yards	0.765	cubic meters	m^3
NOTE: volumes greater than 1000 L shall be shown in m^3				
MASS				
oz	ounces	28.35	grams	g
lb	pounds	0.454	kilograms	kg
T	short tons (2,000 lb)	0.907	Megagrams	Mg (or "t")
TEMPERATURE (exact degrees)				
^oF	Fahrenheit	5(F-32)/9 or (F-32)/1.8	Celsius	^oC
FORCE and PRESSURE or STRESS				
kip	1,000 pound force	4.45	kilonewtons	kN
lbf	pound force	4.45	newtons	N
lbf/in^2	pound force per square inch	6.89	kilopascals	kPa
ksi	kips force per square inch	6.89	Megapascals	MPa

TECHNICAL REPORT DOCUMENTATION PAGE

1. Report No.	2. Government Accession No.	3. Recipient's Catalog No.

4. Title and Subtitle	5. Report Date
Scaling and Validation of Breakaway Connection for Multi-post Ground Signs	November 2016
	6. Performing Organization Code
	8. Performing Organization Report No.
7. Author(s)	
Gary R. Consolazio, Douglas G. Innocent	2016/114986-114987
9. Performing Organization Name and Address	10. Work Unit No. (TRAIS)
University of Florida Department of Civil and Coastal Engineering 365 Weil Hall, P.O. Box 116580 Gainesville, FL 32611-6580	11. Contract or Grant No. BDV31-977-24
12. Sponsoring Agency Name and Address	13. Type of Report and Period Covered
Florida Department of Transportation Research Management Center 605 Suwannee Street, MS 30 Tallahassee, FL 32399-0450	Final Report
	14. Sponsoring Agency Code

15. Supplementary Notes

16. Abstract

Multi-post ground signs installed adjacent to Florida roadways must be designed for both hurricane wind loading and vehicle collision loading. With respect to hurricanes, all structural sign components must be designed to survive applicable code-specified wind loading conditions. In contrast, during vehicle impact (collision), the design goal is not structural survivability, but rather vehicle-occupant survivability, i.e., prevention of serious occupant injury. In a previous FDOT study (BDK75-977-40), an innovative breakaway system referred to as the 'moment-resisting collar connection' was developed for use in large roadside sign structures. Conservative selections of design parameters such as sign size and design life (50 years instead of the typical 10 years) yielded a relatively heavy structural system that was indeed capable of surviving hurricane wind loading, but which also exhibited occupant risk values that approached the maximum limits permitted by AASHTO MASH.

With the introduction of an FDOT policy requiring that supplementary exit number markings be painted on the shoulders of major highways (i.e., post-hurricane emergency responder routes), it was no longer deemed critical that breakaway signage be designed for a 50-year life. In the present study, therefore, the design life was reduced to 10 years, hurricane wind loads were recomputed, and an updated 'high-capacity' moment collar breakaway connection was designed. Development of this optimized and simplified connection led to reductions in sign post weight, breakaway connection weight, fabrication complexity, fabrication cost, and occupant risk. Moreover, to address the fact that most roadside sign structures are smaller in size than the 'practical maximum' structure size adopted in BDK75-977-40, the present study also included development of scaled-down 'medium-capacity' and 'low-capacity' moment-collar connections. All three systems (high-, medium-, and low-capacity) were designed to meet the applicable AASHTO standards for flexural strength and impact performance. Demonstration of adequate structural performance was achieved using a combination of finite element simulation techniques (quasi-static and impact) and physical validation testing (static flexural capacity testing and AASHTO MASH-compliant 1100C surrogate vehicle pendulum impact testing).

17. Key Words	18. Distribution Statement
Roadside sign structure, breakaway, wind load, vehicle impact, collision, finite element simulation, pendulum impact testing, occupant risk, fuse plate, hinge plate	No restrictions.

19. Security Classif. (of this report)	20. Security Classif. (of this page)	21. No. of Pages	22. Price
Unclassified	Unclassified	---	

Form DOT F 1700.7 (8-72). Reproduction of completed page authorized

ACKNOWLEDGEMENTS

The authors thank the Florida Department of Transportation (FDOT) for providing the funding that made this research possible. Additionally, the authors acknowledge the significant contributions made by personnel of the FDOT Structures Research Center in providing technical insights and suggestions, fabricating and constructing testing-systems and test-articles, providing data acquisition, and conducting impact tests.

EXECUTIVE SUMMARY

Multi-post ground signs installed adjacent to Florida roadways must be designed for both hurricane wind loading and vehicle collision loading. With respect to hurricanes, all structural sign components must be designed to survive applicable code-specified wind loading conditions. In contrast, during vehicle impact (collision), the design goal is not structural survivability, but rather vehicle-occupant survivability, i.e., prevention of serious occupant injury. In a previous FDOT study (BDK75-977-40), an innovative breakaway system referred to as the 'moment-resisting collar connection' was developed for use in large roadside sign structures. Conservative selections of design parameters such as sign size and design life (50 years instead of the typical 10 years) yielded a relatively heavy structural system that was indeed capable of surviving hurricane wind loading, but which also exhibited occupant risk values that approached the maximum limits permitted by AASHTO MASH.

With the introduction of an FDOT policy requiring that supplementary exit number markings be painted on the shoulders of major highways (i.e., post-hurricane emergency responder routes), it was no longer deemed critical that breakaway signage be designed for a 50-year life. In the present study, therefore, the design life was reduced to 10 years, hurricane wind loads were recomputed, and an updated 'high-capacity' moment collar breakaway connection was designed. Development of this optimized and simplified connection led to reductions in sign post weight, breakaway connection weight, fabrication complexity, fabrication cost, and occupant risk. Moreover, to address the fact that most roadside sign structures are smaller in size than the 'practical maximum' structure size adopted in BDK75-977-40, the present study also included development of scaled-down 'medium-capacity' and 'low-capacity' moment-collar connections. All three systems (high-, medium-, and low-capacity) were designed to meet the applicable AASHTO standards for flexural strength and impact performance. Demonstration of adequate structural performance was achieved using a combination of finite element simulation techniques (quasi-static and impact) and physical validation testing (static flexural capacity testing and AASHTO MASH-compliant 1100C surrogate vehicle pendulum impact testing).

TABLE OF CONTENTS

LIST OF FIGURES

Figure Page

LIST OF TABLES

Table Page

CHAPTER 1
INTRODUCTION

1.1 Background

Multi-post ground signs installed adjacent to roadways in Florida must be designed for hurricane wind loading as well as for vehicle impact loading. With respect to hurricane wind loads, all structural components in a sign structure—support posts, base connections, etc.—must be designed to resist (i.e., survive without failing) the applicable code-specified wind loads. For design purposes, wind loading is treated as a static-equivalent pressure applied to the sign panel (Figure 1.1a). Due to the significant vertical offset that typically exists between the center of wind pressure, and the base of the support posts, wind loads generally produce large flexural moments that must be resisted both by the sign posts as well as by the base connections.

In contrast, under vehicle impact conditions, where an errant passenger vehicle leaves the roadway and strikes a roadside sign structure, the intended design goal is not structural survivability, but rather vehicle occupant survivability—or more specifically, prevention of serious occupant injury. Contact between the front bumper of a vehicle and a sign post typically occurs at a relatively low vertical elevation (~18 in. from the ground plane), thus application of vehicle impact loading (Figure 1.1b) causes large shear forces in the support posts and base connection components, but not significant flexural moments.

To limit the risk of injury to vehicle occupants, loads associated with vehicle collision can be employed to break (i.e., disengage) selected structural components in the base connections of a sign structure (Figure 1.2). Once the base connection components 'break away', flexural moment is transmitted along the length of the support post, in turn causing tension loading of a perforated steel 'fuse plate' located just below the sign panel. At a sufficiently high tension level, the fuse plate ruptures allowing the lower segment of the post to rotate out of the path of the vehicle. A hinge plate on the non-impact (downstream) side of the posts keeps the lower segment connected to the rest of the sign structure during rotation. (In Figure 1.3, an illustration of this overall process is shown, with rendering of the vehicle omitted).

Risk of injury to vehicle occupants during a collision is primarily associated with either vehicle decelerations or with parts of the sign structure deforming the vehicle compartment (e.g., causing roof intrusion). Regarding the former, abrupt vehicle deceleration can cause occupants to strike interior portions of the vehicle compartment at a velocity referred to as the 'occupant impact velocity' (OIV). Reducing the potential for occupant injury is achieved by limiting the OIV. Limiting the OIV is in turn achieved—from a structural design perspective—by designing a sign post system that 'breaks away' during impact, thus reducing inertial post resistance and, accordingly, reducing vehicular deceleration. With respect to vehicle compartment intrusion, limiting the associated risk can be achieved by ensuring that the lower segment of the post swings out of the path of the vehicle during collision. Both OIV and compartment intrusion can be mitigated by reducing the weight (i.e., mass) of the components that make up a breakaway sign post. Therefore, a key focus of the present study was to develop sign support systems that minimize post weight and breakaway connection weight while still providing adequate strength to resist hurricane force wind loads.

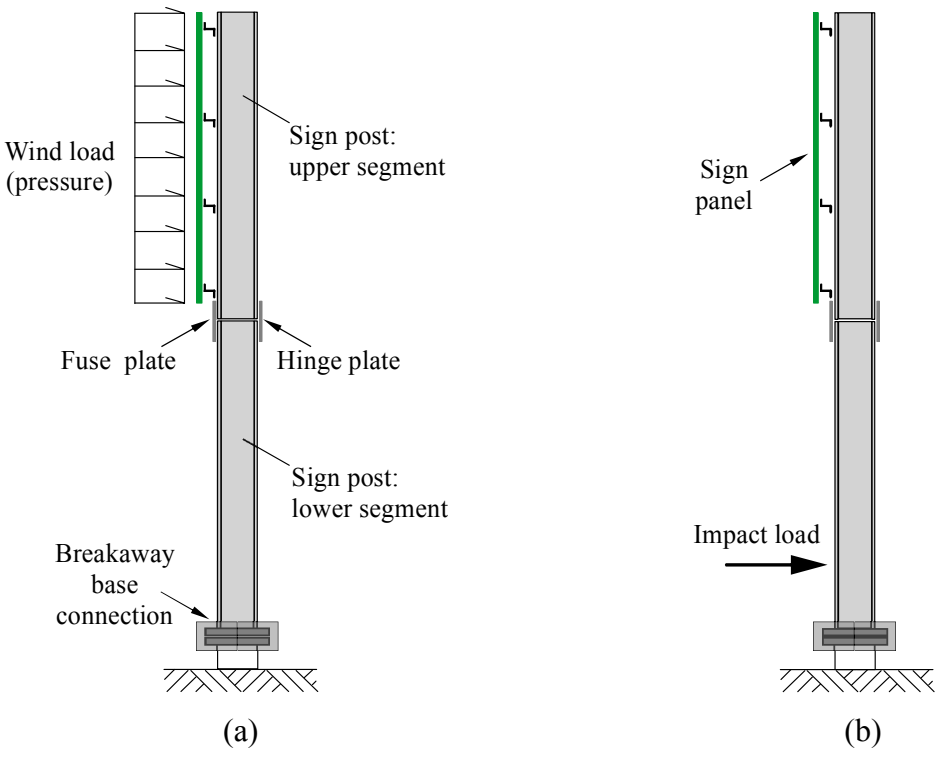

Figure 1.1 Design loading conditions on a roadside sign structure:
(a) Wind loading applied to sign panel; (b) Vehicle impact loading applied to post

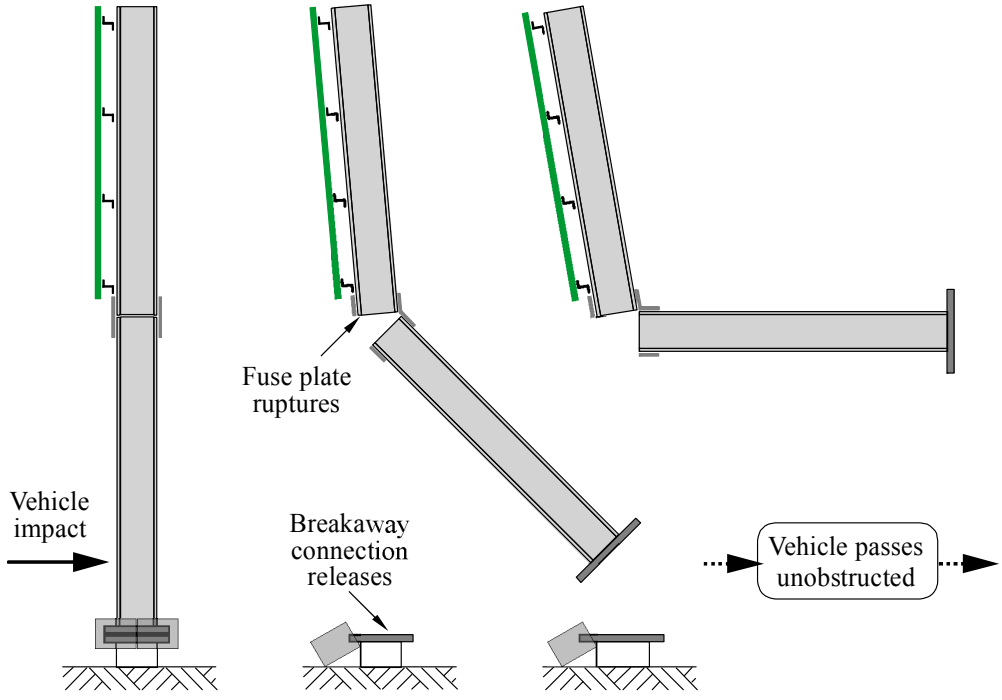

Figure 1.2 Intended breakaway behavior under vehicle impact loading conditions

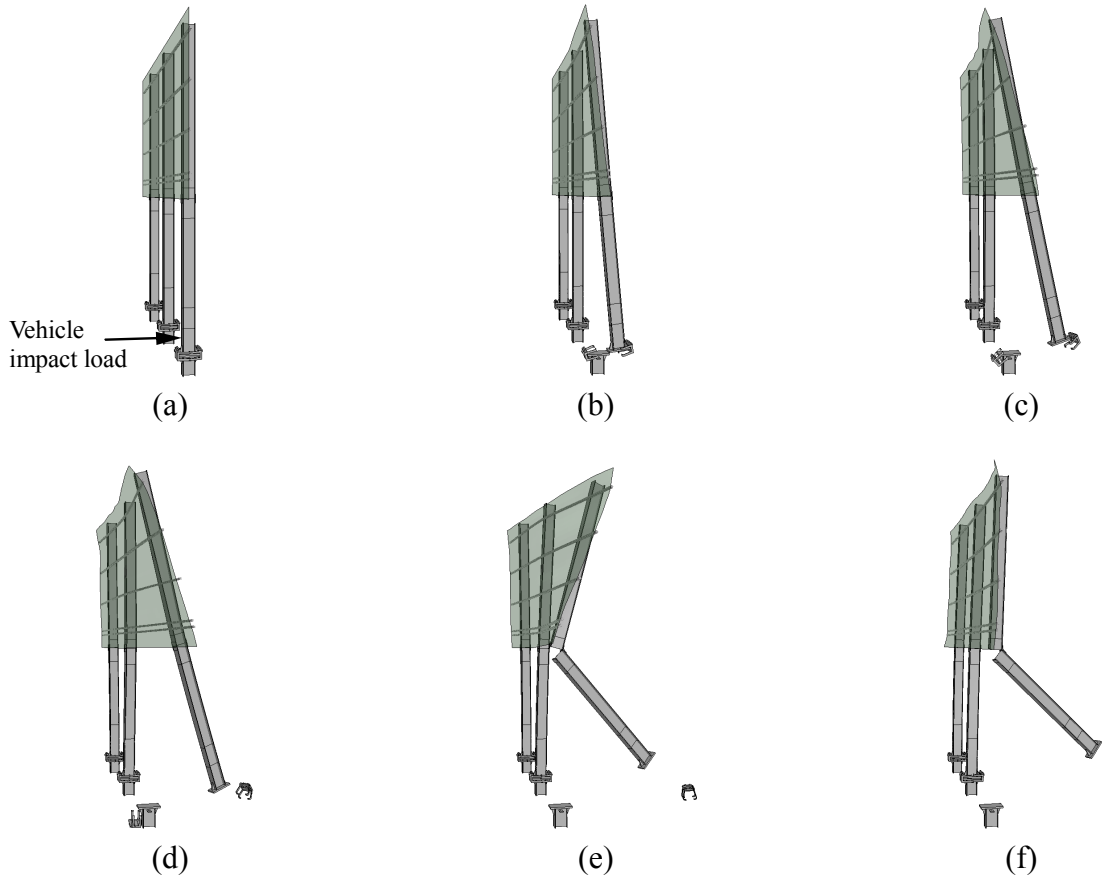

Figure 1.3 Intended system behavior of a three-post sign structure:
(a) Impact load from vehicle (not shown) is applied to right most column; (b) Breakaway base connection disengages; (c-d) Fuse plate at top of lower segment is loaded; (e) Fuse plate ruptures; (f) Lower-segment of post rotates out of path of vehicle

In a previous FDOT study (BDK75-977-40, Consolazio et al., 2012), a new type of high-capacity breakaway connection system (Figure 1.4) was developed for use in large roadside sign structures that employ steel 'wide flange' sections as posts. In designing this new breakaway connection (referred as a 'shear-controlled moment-resisting collar'—or more simply a 'moment collar'), the required static wind load capacity of the connection was established based on a 50 year design life (rather than the 10 year design life that is typically used for such structures), a 'practical-maximum' sign panel size of 12 ft x 20 ft, and a clearance height of 11 ft. These conservative parameter selections produced a breakaway connection that was capable of resisting severe wind loads on large sign panels. However, the same parameter selections also necessitated a relatively heavy structural steel post size (W12x40), relatively heavy breakaway connection components (e.g., plates), and fabrication requirements that were undesirably complex (e.g., the need for collar plate stiffeners).

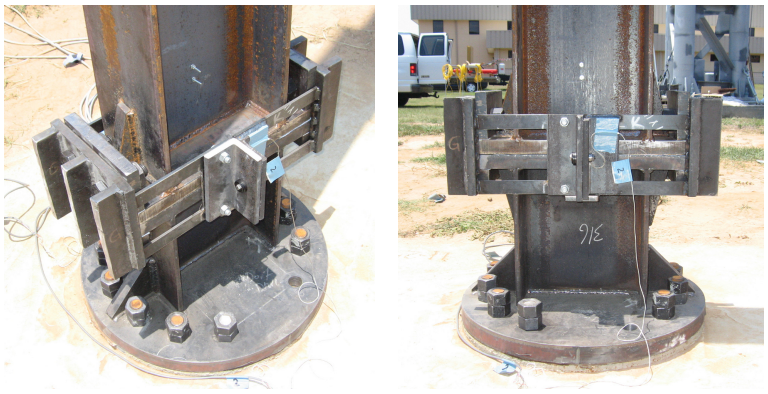

Figure 1.4 High-capacity moment collar breakaway connection developed in FDOT project BDK75-977-40

1.2 Objectives

A primary objective of the present study was to update the moment collar breakaway connection system from BDK75-977-40 (Consolazio et al., 2012) in such a manner that post weight, connection weight, fabrication complexity, fabrication cost, and occupant risk (e.g., OIV) were all reduced (i.e., improved). Implementation of an FDOT policy requiring that exit numbers be painted directly on the paved shoulders of major roadways—to assist emergency responders in exit number identification after a storm—aided in this connection update effort. As a consequence of implementation of this policy, it was no longer deemed critical that breakaway signage be capable of surviving a 50 year hurricane wind event. Instead, use of a shorter 10 year design life, which is consistent with the recommendations of AASHTO LTS-6 (2013), was deemed suitable.

In AASHTO LTS-6 (2013), design wind pressure, P_Z (in units of psf) is computed as:

$$P_Z = 0.00256\, K_Z G V^2 I_r C_D \tag{1.1}$$

where K_Z is the height and exposure coefficient, G is the gust effect factor, V is the basic wind speed (mph), I_r is the importance factor, and C_D is the drag coefficient. For hurricane regions where V>100 mph (e.g., Florida), the importance factor decreases from I_r =1.0 for a 50 year design life to I_r =0.54 for a 10 year design life (a 46% reduction). Per Eqn.(1.1), wind pressure on a sign panel will accordingly decrease by 46%, as will the required flexural capacity of a breakaway base connection. Therefore, the objective of developing an updated moment collar connection—i.e., a connection both 'optimized' (relative to weight) and 'simplified' (relative to fabrication and assembly)—was aided by adoption of the 10 year design life.

Moreover, for sign panels that are smaller in size than the 'practical maximum' panel size assumed in FDOT study BDK75-977-40 (i.e., 12 ft x 20 ft), the associated wind loads—and therefore the required breakaway connection flexural capacities—are further reduced. Additional objectives of the present study were therefore to develop 'scaled-down' versions of the updated moment-resisting collar connection, suitably sized (and optimized) for use with smaller sign panels. By developing scaled-down systems, post weight, connection weight, and occupant risk would be reduced, along with material and fabrication costs.

1.3 Scope of work

- Establish design basis for revised breakaway connections: A review of pertinent literature, design specifications, and FDOT signage inventory was conducted to establish a suitable design basis for developing updated moment-collar breakaway connection systems. Specifications published by AASHTO and FDOT were used to perform wind load calculations and steel post capacity calculations over a range of different sign structure configurations. Calculation results were then used to define three discrete sizes of breakaway connection: high-, medium-, and low-capacity. Applicable AASHTO requirements relating to ultimate flexural strength and impact performance were also identified.
- Design and test high-capacity breakaway system: Using the moment collar connection developed in BDK75-977-40 as an initial starting point, multiple approaches to designing an updated high-capacity breakaway connection system were evaluated analytically. Principal goals in the design-iteration process included optimizing component weights, and simplifying the connection fabrication- and assembly-processes. Quasi-static finite element simulations were used to assess ultimate flexural strength, whereas dynamic simulations were used to assess impact performance. Subsequently, experimental test articles were fabricated and subjected to static flexural capacity testing and pendulum impact testing so that design adequacy, per AASHTO LTS-6 and AASHTO MASH, could be confirmed. Impact tests included head-on (0 deg.) surrogate-vehicle testing, oblique (25 deg.) testing, as well as isolated fuse plate and hinge plate testing.
- Design and test scaled-down (medium- and low-capacity) breakaway systems: Quasi-static and dynamic-impact finite element simulations were used to analytically assess the performance of candidate scaled-down medium-capacity and low-capacity connection system designs. General principles employed in the scale-reduction process were: maintaining commonality of design concepts and system components across all sizes of connection; maintaining uniformity of key component dimensions; and balancing the optimization of component dimensions against the availability of materials and components. Medium-capacity and low-capacity experimental test articles were subsequently fabricated and subjected to head-on (0 deg.) surrogate-vehicle testing, and oblique (25 deg.) impact testing so that adequacy per AASHTO MASH could be confirmed.

CHAPTER 2
DESIGN BASIS AND DESIGN APPROACH

2.1 Review of technical literature

In Consolazio et al. (2012), a thorough review of technical literature pertaining to breakaway connection design was presented. In the present study, the moment-resisting collar developed in BDK75-977-40 was updated through optimization and down-scaling. Consequently, a targeted literature review was conducted to determine if recently published breakaway connection concepts might be identified which would be applicable in the connection updating process. A range of pertinent transportation- and structural-engineering related technical journals were reviewed. Technical articles presenting recently developed breakaway concepts (published since the BDK75-977-40 study was conducted) were found to focus nearly exclusively on deformable barrier (railing) systems, and the relatively short breakaway posts (e.g., timber posts) that are typically used in such systems. In contrast, articles focusing on the design of relatively tall, high-capacity metallic (steel, aluminum) breakaway sign support posts were not identified (aside from those previously documented in Consolazio et al., 2012).

2.2 Review of design specifications

2.2.1 Specifications relating to vehicle impact load and breakaway connection performance

All moment-resisting collar connections developed in the present study were subjected to crushable-nose (deformable) surrogate vehicle pendulum impact testing in a manner compliant with the requirements of AASHTO MASH (2009). As such, a comprehensive review of AASHTO MASH was conducted to establish design, testing, and performance requirements for the breakaway connections that were developed. Additionally, a review of breakaway sign support requirements set forth in AASHTO LTS-6 (2013, 2015), was conducted. On several important items, the requirements set forth in AASHTO LTS-6 for breakaway supports (e.g., Chapter 12) complement those contained in AASHTO MASH. For example, the factor of safety required from breakaway connection ultimate strength testing; treatment of dead and wind load combinations; permissible residual breakaway stub height; post hinge elevation; maximum post weight; etc. are all specified in AASHTO LTS-6.

It is also important to note that in regard to ‘breakaway connection dynamic performance’ (i.e., vehicle impact loading), AASHTO LTS-6 references older vehicle impact test requirements from NCHRP 350 (Ross et al., 1993) rather than newer requirements contained in AASHTO MASH (2009). To ensure that the updated moment-resisting collar connections developed and tested in this study meet the most up-to-date impact performance requirements, all breakaway connections were designed to meet the more stringent AASHTO MASH requirements rather than the NCHRP 350 requirements. Specific aspects relating to this choice of design basis are documented in more detail later in this report.

2.2.2 Specifications relating to wind load and steel component capacity

To ensure that the moment-resisting collar connections developed in this study will be applicable to a wide range of sign structural configurations (i.e., combinations of sign panel size, sign panel clearance height, number of sign posts, and structural post size), wind load and post-

sizing (capacity) calculations were performed for a variety of different hypothetical sign structure configurations. Prior to implementing the calculation procedures used in this process, a thorough review of pertinent design specifications was performed. Specifically, all AASHTO LTS-6 (2013, 2015) design requirements relating to wind load, load combinations, and steel post design (capacity evaluation) were reviewed in detail. In addition, the FDOT LTS-6 (2015) requirements, i.e., the FDOT modifications to AASHTO LTS-6, were also reviewed as were the FDOT SDG (2015) requirements, as they relate to wind load determination.

2.3 Review of FDOT signage

Key components of this study involved designing 'discrete' scaled-down versions of the moment-resisting collar connection. The term 'discrete' is meant to indicate 'pre-configured' breakaway connections with specific, pre-defined geometric dimensions. Each of these discrete, pre-configured breakaway connections needed to possess sufficient strength so as to be applicable over a range of different sign structure configurations (i.e., different combinations of sign panel size, sign panel clearance height, number of sign posts, and structural post size).

A review of FDOT signage was therefore conducted to assess the range of sign structure configurations currently in use in Florida. In prior study BDK75-977-40, the sign structure size selected for use in designing the original moment-resisting collar was: panel depth=12 ft, width=20 ft, and clear height=11 ft. This size was based on a review of the work of Pinelli and Subramanian (1999) who, among other tasks, cataloged the sizes of representative sign structures located primarily along the central Atlantic coast of Florida. Among the sign structures documented by Pinelli and Subramanian, the panel dimensions (depth, height), clear heights, and number of support posts varied considerably.

To update this information and to generate a wider (statewide) geographic sampling, a review of current FDOT signage was conducted using the FDOT video log viewer (`https://fdotwp1.dot.state.fl.us/videolog`) that is maintained by the FDOT Transportation Statistics Office. The FDOT video log viewer provides a means of reviewing up-to-date video logs—including roadside signage—for virtually all of Florida's major roadways. Reviews of video logs for I-10, I-75, I-4/I-275, and I-95 were conducted for a half dozen Florida counties.

Representative samples of roadside sign structures identified through this review process are provided in Figure 2.1 – Figure 2.6. In each figure, the sign structures shown are ordered approximately from largest panel size to smallest going from 'a' to 'd'. Observed panel sizes varied from large (Figure 2.1a, Figure 2.3a) to small (Figure 2.4d, Figure 2.5c-d); post cross-sectional sizes varied from large (Figure 2.1b) to small (Figure 2.4d); post arrangements (count and spacing) varied considerably; and clear heights range from minimal (far posts of Figure 2.1a and Figure 2.2a) to significant (Figure 2.1b, Figure 2.3c, Figure 2.6a).

Results from the signage review demonstrated that wide ranging combinations of panel size, clear height, and post configuration were possible, all dictated by local site requirements (quantity of information to be displayed on the sign, roadside slope, wind loading severity, etc.). Consequently, it was not deemed feasible to uniquely map from a particular sign panel size to a specific size of scaled-down moment-resisting collar. For example, sign panels of roughly equal size (area) but with different clear heights would produce significantly different wind-induced base moments, thereby necessitating different sizes of moment-resisting collar connection. Attempting to uniquely map from sign panel size to corresponding moment-resisting collar size would only serve to constrain the designers decision making process.

(a) (b) (c) (d)

Figure 2.1 Sign structures located along I-4/I-275 in Hillsborough County, FL

(a) (b) (c) (d)

Figure 2.2 Sign structures located along I-10 in Jackson County, FL

(a) (b) (c) (d)

Figure 2.3 Sign structures located along I-10 in Leon County, FL

(a) (b) (c) (d)

Figure 2.4 Sign structures located along I-75 in Alachua County, FL

(a) (b) (c) (d)

Figure 2.5 Sign structures located along I-75 in Hernando County, FL

(a) (b) (c) (d)

Figure 2.6 Sign structures located along I-95 in Brevard County, FL

Instead, to preserve maximum flexibility in the design process, a different approach was employed. Selection of the appropriate size of moment-resisting collar connection is to be based on the cross-sectional size of the sign post, and the wind-induced base moment. Each discrete size of scaled-down moment-resisting collar developed in this study is suitable for use over a specific range of post cross-sectional sizes (e.g., 'depths from 9 – 12 in.') and wind-induced base moments up to a specified maximum limit. The maximum permissible base moment for each discrete size of breakaway connection (documented later in this chapter) was established based on calculated demands (moment, shear) for sign structures covering the range of configurations typically found in the field (as indicated by the results of the FDOT signage review).

2.4 Design basis

2.4.1 Vehicle impact load and breakaway connection performance

Impact design requirements for the breakaway sign structures developed in this study were based on vehicle impact conditions and breakaway performance criteria set forth in AASHTO MASH (2009) and AASHTO LTS-6 Chapter 12 (2013, 2015). Requirements from these specifications that were pertinent to the present study are summarized in Table 2.1. Structural adequacy under impact conditions requires that breakaway supports shall readily fail in a predictable manner by breaking, fracturing, or yielding when struck head-on (or at an angle of 25 degrees) by a standard vehicle with a mass of 1100 kg (2420 lbf) at a nominal speed of 30 kph (19 mph) for a low-speed impact. The 1100 kg mass specified by MASH is representative of passenger cars such as the Kia Rio or Toyota Yaris.

In regard to occupant risk factors, AASHTO MASH limits the longitudinal occupant impact velocity (OIV) with respect to the interior surface of the passenger compartment to no greater than 16 ft/sec, with values less than 10 ft/sec being preferred. Maximum allowable occupant ridedown acceleration (ORA) is limited to 20.49 g, but preferably should not exceed 15 g. Detached elements (debris) from the breakaway support are not permitted to penetrate, or show potential for penetrating, the vehicle occupant compartment or present an undue hazard to other traffic, pedestrians, or personnel in a nearby work zone. Potential for serious injury to vehicle occupants, due to deformation of the occupant compartment, is not acceptable. In addition to the AASHTO MASH criteria cited above, AASHTO LTS-6 provides additional requirements to ensure predictable and safe breakaway structural performance. For example, to prevent a vehicle from snagging after breaking a support post away from the base, AASHTO LTS-6 limits the maximum residual stub height to 4 in.

2.4.2 Wind load and steel component capacity

Structural selection and design of breakaway base connection components (plates, bolts, etc.), steel sign posts, and related additional components (e.g., fuse plates and hinge plates), were based on the wind load and flexural capacity specifications contained in AASHTO LTS-6 (2013, 2015), FDOT LTS-6 (2015), and FDOT SDG (2015). In Table 2.2, a summary is provided of the design parameters from these specifications that were most pertinent to the present study.

2.5 Discrete connection sizes

To establish discrete sizes of moment-resisting collars that would be suitable for use in conjunction with typical FDOT signage, wind load, and steel post capacity calculations were performed for sign structures having various panel heights, panel widths, clear heights, and numbers of posts (2 or 3). For each structural configuration considered, the provisions of FDOT SDG (2015), FDOT LTS-6 (2015), and AASHTO LTS-6 (2013, 2015) were used to select an efficient steel wide-flange post cross-sectional shape. Calculations of this type were performed for more than fifteen (15) different hypothetical sign structure configurations. (In Appendix A, the complete wind load and steel post capacity calculation procedure is presented, in detail, for a single sign structure.)

Table 2.1 Vehicle impact load and breakaway connection performance requirements

AASHTO document	Section	Parameter	Requirement
MASH	2.1.1	Passenger car (1100C) mass	2420 ± 55 lbf (1100 ± 25 kg)
MASH	2.2.4.1	Test 3-60 impact speed	19 mph (30 kph)
MASH	2.2.4.1	Test 3-60 kinetic energy	$\leq$ 34 kip-ft ($\leq$ 20% in excess of target)
MASH	2.2.4.1	Evaluation criteria	B, D, F, H, I, N in MASH Section 5.3
MASH	2.2.4.1	Impact angles, min. and max.	θ = 0 deg. and θ = 25 deg.
MASH	2.2.4.1	Impact location	At transverse centerline of crushable nose
MASH	4.2.2	Surrogate vehicle type	Crushable nose impactor based on Kia-Rio
MASH	4.2.2	Roof/windshield impact	Will be assessed via impact test and FEA simulation
MASH	5.3	Table 5-1, Criteria B	Breakaway connection shall readily activate
MASH	5.3	Table 5-1, Criteria D	Detached fragments will not show potential for danger
MASH	5.3	Table 5-1, Criteria F	Vehicle shall remain upright after collision
MASH	5.3	Table 5-1, Criteria H	Occupant impact velocity $\leq$ 10 ft/sec (preferred)
MASH	5.3	Table 5-1, Criteria H	Occupant impact velocity $\leq$ 16 ft/sec (maximum)
MASH	5.3	Table 5-1, Criteria I	Occupant ridedown acceleration $\leq$ 15 g (preferred)
MASH	5.3	Table 5-1, Criteria I	Occupant ridedown acceleration $\leq$ 20.49 g (maximum)
MASH	5.3	Table 5-1, Criteria N	Acceptable vehicle trajectory behind test article
MASH	A5.3	Flail-space model	Longitudinal occupant flail distance = 2 ft
LTS-6	12.5.1	Impact test criteria	NCHRP 350 indicated but MASH will be used instead
LTS-6	12.5.3	Residual stub height	Stub height after connection 'breakaway' $\leq$ 4 in.
LTS-6	12.5.3	Sign post hinge elevation	Shall be $\geq$ 7 ft above ground
LTS-6	12.5.3	Sign post weight (per ft)	If post spacing $\geq$ 7 ft , max post weight = 45 lbf/ft
LTS-6	12.5.3	Sign post weight (total)	Total post weight, from slip plane to hinge, $\leq$ 600 lbf

Table 2.2 Determination of wind load and steel component capacity

Document	Section	Parameter	Design basis
FDOT LTS-6	3.8.3	Design life	Table 3-3, roadside sign structures: 10 year
FDOT LTS-6	3.8.2	Basic wind speed	FDOT LTS-6 cites FDOT SDG for wind speed
FDOT SDG	2.4.1	Basic wind speed	FL coastal county wind speed chosen: V = 150 mph
AASHTO LTS-6	3.4	Group II loads (DL+W)	Allowable stress increase for post = 33%
AASHTO LTS-6	Ch. 5	Factor of safety: post	Based on provisions in AASHTO LTS-6 Ch. 5
AASHTO LTS-6	12.4	Group II loads (DL+W)	Allowable load increase for connection = 0%
AASHTO LTS-6	12.4	Factor of safety: connection	FS $\geq$ 1.5 for ultimate strength from flexural testing
N/A	N/A	Number of sign posts	Sign structures with 2 or 3 posts will be considered
N/A	N/A	Steel yield strength	Fy = 50 ksi

For each structural configuration considered, the wind-induced flexural moment acting on the breakaway connection, and the cross-sectional dimensions (section depth and flange width) of the steel post were recorded. Based on the collected data, it was determined that three (3) discrete sizes of moment-resisting collar would span typical FDOT signage needs: low-capacity, medium-capacity, and high-capacity (Table 2.3). Each discrete connection size is applicable up to a specified maximum moment, and over a specified range of post section depths. Noteworthy is the fact that the section depth ranges defined in Table 2.3 for low-, medium-, and high-capacity connections span the entire range of section depths used in the FDOT Design Standards, Index 11200—wherein depths range from 6 in. to 12 in.

To demonstrate the range of applicability of the proposed discrete connection sizes, a series of example sign structure configurations are presented in Table 2.4. For each of these cases, calculations of the type presented in Appendix A were conducted, and a suitable breakaway connection capacity (high, medium, low) was selected based on the wind-induced moment and steel post section depth.

Table 2.3 Discrete sizes of moment-resisting collar connection

Moment-resisting collar capacity	Maximum design flexural moment	Post cross-sectional depth range (d)	Maximum post flange width (b_f)
High (H)	80 kip-ft	9 in. – 12 in.	8.0 in.
Medium (M)	55 kip-ft	6 in. – 9 in.	8.0 in.
Low (L)	30 kip-ft	3 in. – 6 in.	8.0 in.

Table 2.4 Example sign structure configurations for each proposed discrete size of moment-resisting collar connection

Moment-resisting collar capacity	Vertical panel depth	Horizontal panel width	Clearance height	Number of posts	Steel post section
High (H)	10 ft	12 ft	15 ft	2	W10x26
	12 ft	12 ft	15 ft	2	W10x30
	12 ft	20 ft	11 ft	3	W10x26
Medium (M)	6 ft	19.5 ft	13 ft	2	W8x21
	6 ft	19.5 ft	15 ft	2	W8x24
	10 ft	10 ft	15 ft	2	W8x24
Low (L)	5 ft	8 ft	12 ft	2	W4x13
	10 ft	10 ft	7 ft	2	W5x16
	10 ft	12 ft	7 ft	2	W5x19

2.6 Overall approach

The overall approach used to design the high-, medium-, and low-capacity breakaway connection systems combined the following processes:

- Use of applicable design aids: Standard structural design aids such as AASHTO LTS-6, AISC steel design specifications, etc. were used to size/select/design various components of candidate breakaway system designs.
- Finite element modeling and simulations: Finite element modeling and *dynamic* simulations were used to quantify impact-related occupant risk factors, such as OIV, for candidate breakaway system designs. Similarly, finite element modeling and *quasi-static* 'pushover' simulations were used to analytically quantify the ultimate flexural capacity of various steel components in the breakaway connection designs.
- Pendulum impact testing: Pendulum impact tests of single-post breakaway systems were conducted at the FDOT Structures Research Center to experimentally evaluate breakaway

connection performance and to quantify occupant risk measures for candidate designs. Separate, isolated fuse-plate and hinge-plate impact tests were also conducted using the FDOT pendulum to confirm that fuse plate behavior (including rupture) was in agreement with predictions from finite element impact simulations.

- Static flexural testing: Static flexural tests of high-capacity 'breakaway connection and sign post' assemblies were conducted at the University of Florida to experimentally confirm that the ultimate flexural capacity of the breakaway connection was adequate.

CHAPTER 3
DEVELOPMENT OF HIGH-CAPACITY SYSTEM

3.1 Design approach

Design of the high-capacity (80 kip-ft) breakaway connection involved an iterative process that included the following:

- Conceptual design of components
- Evaluation of impact performance (for occupant risk)
- Evaluation of ultimate flexural strength (for wind load)
- Code checks, constructability checks, etc.

Each performance evaluation step—i.e., impact and wind loading—was carried out by conducting nonlinear finite element (FE) simulations that used the LS-DYNA finite element analysis code (LSTC, 2016).

To evaluate the *impact* performance of each 'candidate' design, finite element models were developed to represent both the breakaway connection as well as a surrogate impacting vehicle. Simplified in form, but capable of adequately reproducing the impact behavior (e.g. force-deformation response) of a production vehicle, surrogate vehicles are permitted by AASHTO MASH for use in impact testing of breakaway hardware. In this study, a finite element model of the UF/FDOT 1100C passenger car crushable-nose surrogate vehicle was employed (Figure 3.1). This surrogate vehicle was designed and validated (Consolazio et al., 2016; Groetaers et al., 2016) to reproduce the force-deformation behavior of a 2006 Kia Rio production passenger car. Results obtained from rigid-pole impact testing (Figure 3.2) of the crushable nose impactor demonstrated good agreement (Figure 3.3) with results obtained from finite element simulations of the crushable nose impactor FE model (Figure 3.1b). Consequently, the FE surrogate vehicle model was used to evaluate the impact performance of all candidate breakaway connection designs considered in the present study. For each candidate design, vehicle-occupant risk measures—i.e., occupant impact velocity (OIV) and occupant ridedown acceleration (ORA)—were computed and compared to the threshold values specified in MASH (recall Table 2.1).

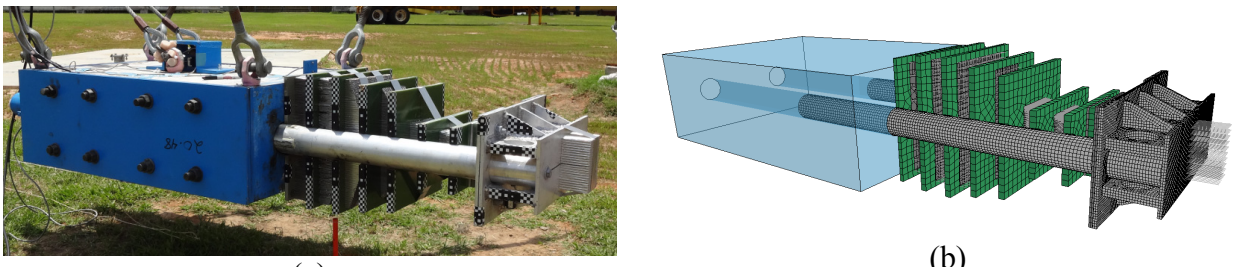

(a) (b)

Figure 3.1 UF/FDOT 1100C crushable nose surrogate vehicle impactor:
(a) Physical system; (b) Finite element model

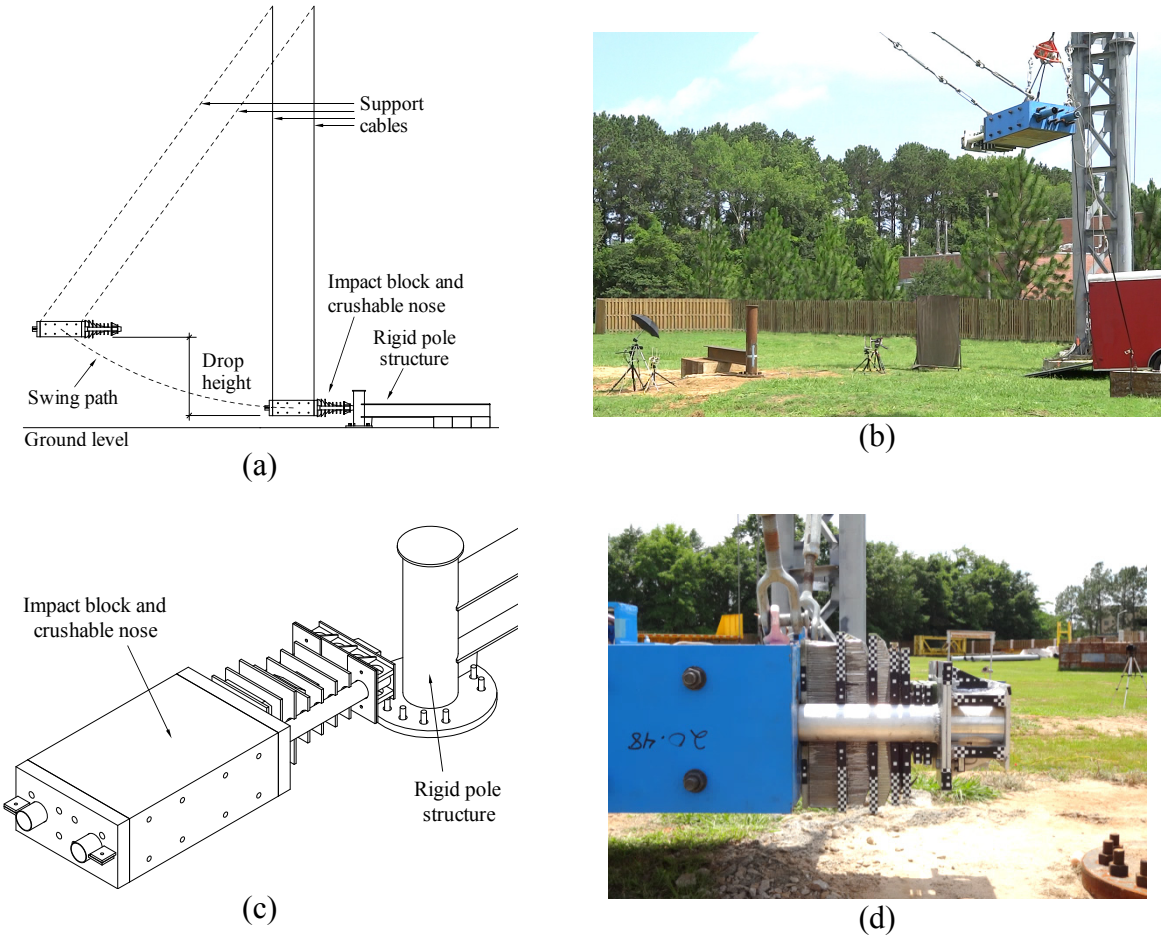

Figure 3.2 Rigid pole pendulum impact testing of surrogate vehicle:
(a) Elevation view schematic; (b) Test setup prior to release of surrogate vehicle;
(c) Isometric view schematic; (d) Crushable nose after impact test

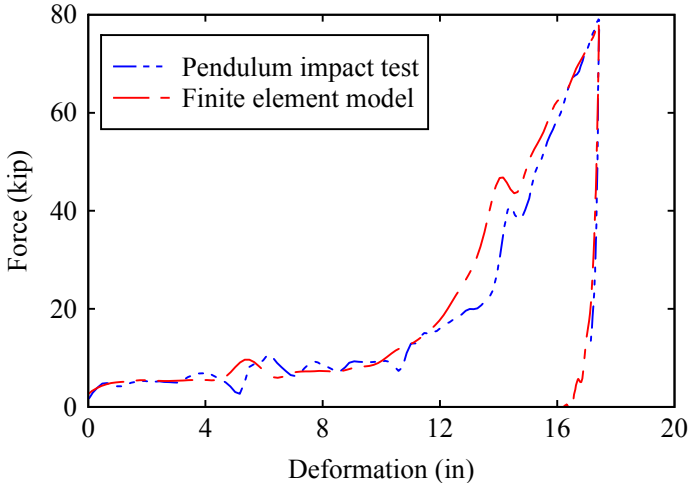

Figure 3.3 Comparison of rigid pole impact test results and FE simulation results

To evaluate ultimate *flexural capacity* under equivalent-static wind loading conditions, finite element models representing each candidate breakaway connection, and an attached segment of sign post, were subjected to quasi-static 'pushover' analyses. In each such analysis, a stiff horizontal spring was attached to the sign post (Figure 3.4a) at the elevation of the center of wind pressure. The node at end of the spring opposite the sign post was prescribed a slow (quasi-static) time-varying horizontal displacement. As the node displaced, axial force generated in the spring acted as an 'equivalent wind load' on the sign post, thus generating flexural moment in the breakaway connection at the base of the post. By using displacement control (prescribed displacement) rather than load control (prescribed load), it was possible to deform each connection-and-post model to the point of structural collapse (plastic pushover), thus permitting a clear evaluation of the ultimate flexural capacity of the base connection. Subsequent interpretation of pushover analysis results was accomplished by computing rotations that accounted for connection-component deformation and post-hinging (Figure 3.4b), and then plotting M-θ response curves for each breakaway system.

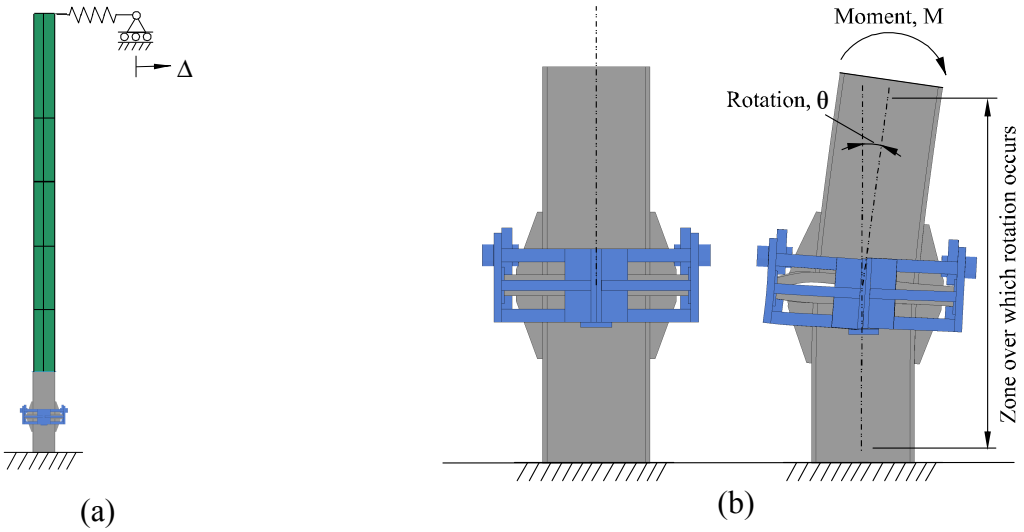

Figure 3.4 Quasi-static finite element pushover simulation used to evaluate ultimate flexural capacity of breakaway connection: (a) Overall model; (b) Relationship between moment and rotation

3.2 Intermediate design iterations

Development of an optimized and simplified high-capacity breakaway connection system was initiated by merging a finite element model of the 1100C UF/FDOT surrogate vehicle (Figure 3.1) together with a finite element model of the moment-resisting collar connection developed in BDK75-977-40 (Figure 3.5a) and a finite element model of a single, full-height sign post. Using this merged (vehicle+connection+post) model, impact simulations were conducted to establish baseline values of occupant risk (OIV, ORA) in a MASH-compliant manner (i.e., using a finite element model of a MASH compliant surrogate vehicle).

Using the BDK75-977-40 system as a starting point for design iterations, various approaches to structural optimization were explored. While a significant number of candidate designs were modeled using finite elements, and evaluated using impact simulation and quasi-static pushover analysis, only key intermediate design iterations are summarized here. In

BDK75-977-40, due to the use of a 50 year design life, relatively heavy W12x40 structural steel sign posts were needed in order to provide sufficient capacity to resist the associated wind loads. In the present study, however a 10 year design life was adopted instead. Based on the reduced design life, reduced wind load, and reduced base moment, it was possible to downsize the steel sign post size from a W12x40 to a W10x26, while still satisfying the requirements of AASHTO LTS-6 (see Appendix A).

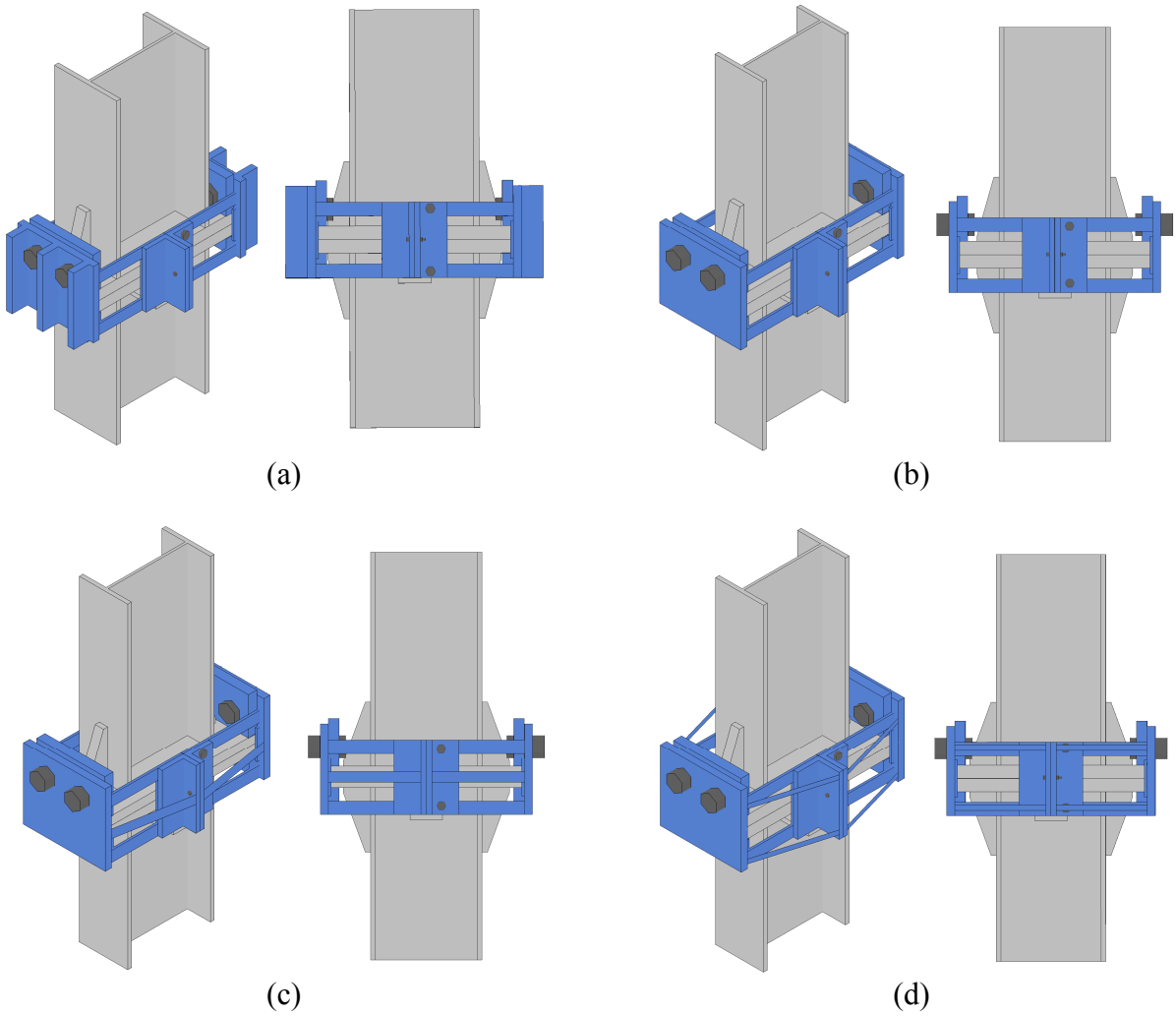

Figure 3.5 Intermediate design iterations:
(a) Original BDK75-977-40 design; (b) Collar stiffeners removed, post size optimized;
(c) Diagonal ties added; (d) Diagonal ties split for accessibility

The reduction in wind-induced base moment not only permitted optimization of the post size, but also optimization of individual breakaway connection components. One early-stage design iteration involved modifying the BDK75-977-40 connection by removing the stiffeners from the primary plates on the collar (Figure 3.5b). Removal of the stiffeners yielded multiple benefits: reduced material costs; significantly reduced fabrication costs (related to cutting and welding the stiffeners); and reduced connection weight, thereby producing reduced occupant

risks (OIV, ORA). Whereas impact simulations of the BDK75-977-40 connection (Figure 3.5a) indicated an OIV value that was close to the *maximum* limit permitted by MASH, corresponding simulations of the optimized connection (Figure 3.5b) produced an OIV value that was below even the preferable values specified by MASH. Thus, the reduction in post and connection weight yielded significant improvements in system performance.

Additional optimizations were also explored—via finite element simulation—including reducing the thickness of the flange plates (the horizontal plates at the slip plane), and reducing the thickness of the triangular stiffeners at the post-to-flange-plate interface. These thickness optimizations were found to only marginally improve the occupant risk values. Moreover, while reducing the thickness of the flange plates offered little benefit in terms of simplifying the fabrication process, this same change had the potential to adversely affect the flexural capacity of the breakaway connection. Consequently, reducing the flange plate thickness was not adopted as a design optimization. However, while reducing the thickness of the triangular stiffeners had little beneficial effect on occupant risk, the same change simplified the welding (fabrication) process. In particular, full penetration welds between the triangular stiffeners and the flange plates was simplified by reducing the triangular stiffener thickness.

A detailed examination of data obtained from quasi-static pushover simulations of the model shown in Figure 3.5b revealed the development of a mechanical advantage mechanism (i.e., prying) acting on the tension connector bolts. For a breakaway connection to function properly, the tension connector bolts must rupture under impact loading (to permit breakaway behavior), but must *not* fail under the application of wind load. Due to the flexibility of the side plates in the optimized collar (Figure 3.5b), prying action caused forces in the bolts to be significantly larger than desired, thus diminishing wind resistance capacity. To mitigate this problem, diagonal tension ties ('straps') were added to the connection, as shown in Figure 3.5c. Quasi-static pushover simulations of the Figure 3.5c connection confirmed that the presence of these ties, to be fabricated from thin steel plates, prevented significant prying on the tension bolts. As a result, the tension bolts were loaded as desired (with approximately one-half of the applied wind shear load going to each bolt), and the flexural capacity of the connection increased, exceeding that required by AASHTO LTS-6.

However, introduction of the diagonal tension ties reduced accessibility to the tension connector bolts, thereby potentially complicating field assembly of the collar connection. An alternative design was therefore explored. In the connection shown in Figure 3.5d, each diagonal tie was split into two separate ties—an upper element and a lower element—thus permitting improved access to the tension bolts, while simultaneously preventing the prying action previously identified. Based on simulation results, the designs shown in Figures 3.5c and 3.5d produced predictable tension bolt rupture and were considered to be reasonably 'optimized' in that they exhibited occupant risk values (OIV, ORA) that were much smaller than those produced by the original design (Figure 3.5a). However, given the significant number of individual structural components that would have to be cut, welded together, or bolted together, these intermediate design iterations were not deemed to be adequately 'simplified'.

3.3 Final design

In all of the designs discussed above (Figure 3.5a-d), each half of the moment collar was unique in configuration: one half was welded, while the other half was partially welded and partially bolted (the bolts allowing accommodation for fabrication tolerances). Since the two collar-halves were non-interchangeable, this would have required the fabrication of numerous unique structural components. Additionally, most of these individual components (side plates, side angles, diagonal ties, lower binding plates, guide bars) would have required welding, thus increasing fabrication costs.

To address these issues, a final high-capacity breakaway connection design was developed (Figure 3.6) that preserved the beneficial structural performance characteristics of the designs discussed above, while simultaneously making use of significantly simplified structural components. (Detailed fabrication drawings for the final high-capacity connection are included in Appendix B.) In the final design, both collar-halves were made to be identical—and therefore interchangeable—and just four (4) unique components form each collar-half:

- Primary plate
- Upper binding plate (bolted)
- Lower binding plate (welded)
- U-plates (bolted)

Fabrication costs were reduced by minimizing the number of unique components that had to be formed, and also by minimizing the use of welding. The only component that required welding was the lower binding plate on each collar half (and this weld was achieved using fillet welds rather than more complex full-penetration welds).

Each collar 'side plate' in the connection was formed by bending a *single* U-shaped plate into the desired configuration—rather than welding multiple plates and angles together as was the case in all designs shown in Figure 3.5 (including the original BDK75-977-40 connection, Figure 3.5a). Moreover, the U-plates are *bolted* to the collar primary plates, thus eliminating welds and simultaneously accommodating fabrication tolerances.

In the final design (Figure 3.6), four (4) tension connector bolts—rather than two (2), as was the case in all of the Figure 3.5 designs—were used to secure the two collar-halves together. Using four (4) connector bolts—rather than two (2)—improved the structural redundancy of the connection against wind load and incidental (non-vehicular) impact loads (e.g., from roadside maintenance operations). The *inwardly curving* geometry of the side U-plates (Figure 3.6) positions the tension connector bolts at shielded locations inside the connection assembly. Moreover, the rounded side geometry formed by joining two curved side plates together significantly reduced the potential for accidental snagging and eliminated the laterally protruding structural-angles that were present in all previously discussed designs (Figure 3.5).

As in the original BDK75-977-40 moment-collar connection, all connections developed and tested (both statically and dynamically) in the present study employed the use of 0.02-in. thick Teflon sheets between steel components that slide relative to one another during vehicle impact loading. Specifically—and as detailed in Appendices B, C, and D—Teflon sheets were used to reduce friction at the large flange-plate-to-flange-plate interface, and at all four (4) of the smaller binding-plate-to-flange-plate interfaces in each connection.

To numerically assess the impact performance of the high-capacity breakaway connection, and to analytically verify that it met the occupant risk limits set forth in MASH

(Table 2.1), a series of finite element impact simulations were performed. At a later stage of this study (described in detail in the following chapter), physical pendulum impact tests were performed to experimentally assess the performance of the high-capacity connection. Due to cable interference issues, such tests could be performed on single-post test articles, but not on multi-post sign structures. Consequently, all physical testing in this study focused on single-post test articles. To complement these tests, corresponding numerical simulations of single-post impact conditions were performed for head-on (0 deg.) and oblique (25 deg.) angles, as described below in Sections 3.3.1 and 3.3.2, respectively. Subsequently, numerical simulation of the most critical (i.e., head-on, 0 deg.) low speed impact condition for a 'full' three-post sign structure is presented in Section 3.3.3.

3.3.1 Single-post, head-on (0 deg.) impact loading performance

A finite element model of the 1100C UF/FDOT crushable nose surrogate vehicle impactor (Figure 3.1) was merged with a finite element model (Figure 3.7a-c) of a W10x26 sign post, the high-capacity breakaway connection, and a channel segment (representing the tributary mass of sign panel), and a head-on (0 deg.), 19 mph (30 kph) impact simulation was conducted. In Figure 3.7d-g, renderings of the finite element simulation results are presented at various points in time during the impact. Both tension connector bolts (top and bottom) on each side of the collar were found to rupture at approximately the same point in time, thus allowing the 'downstream' collar-half to separate cleanly and translate away from the post assembly without undergoing significant yawing (plan-view) rotation, which could lead to potential interference or snagging.

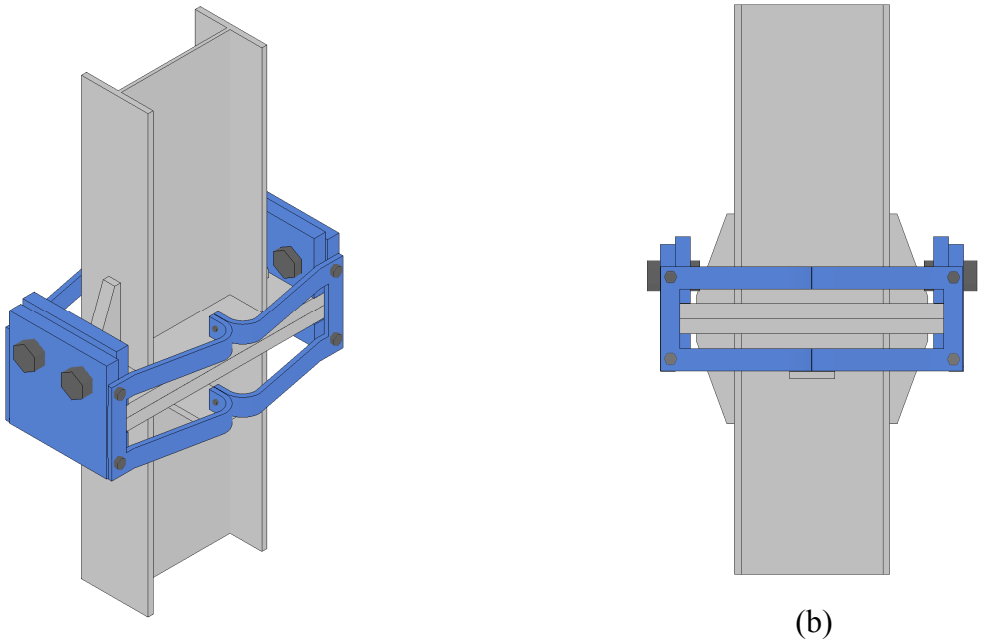

(a) (b)

Figure 3.6 Final high-capacity breakaway connection
(For detailed fabrication drawings, see Appendix B.)

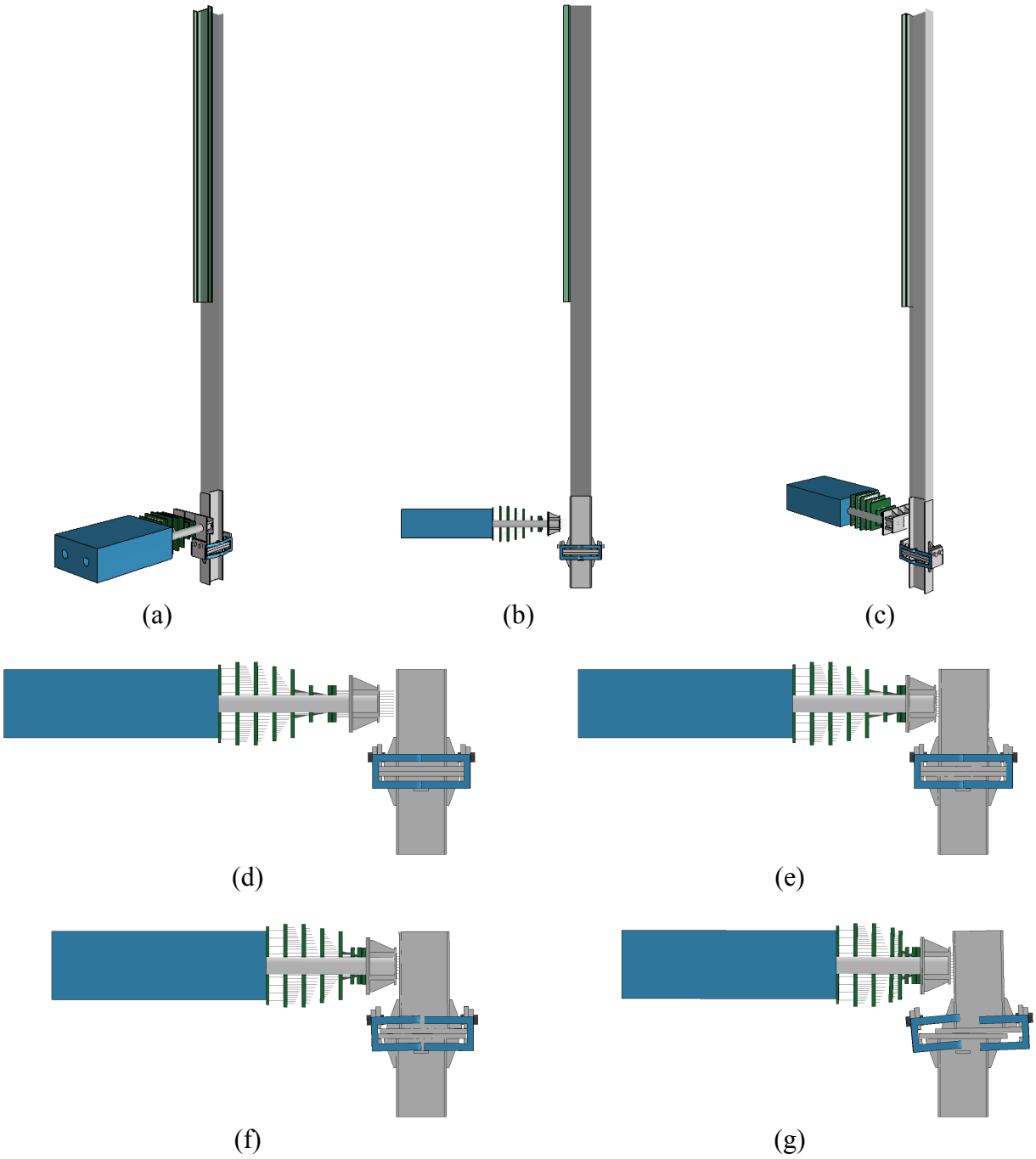

Figure 3.7 Simulation of breakaway connection response to head-on (0 deg.) 19-mph impact:
(a-c) Full-height single-post model with attached channel, as used in simulation;
(d-g) Detailed views of connection behavior during impact loading
(Note: The portion of post above the connection in (a-c) appears visually different
due to use of beam elements, rather than solid elements, in this region.)

For the tension connector bolts to rupture (break) in a predictable manner, the U-plates forming the sides of the collar must be strong enough to prevent excessive (and undesirable) deformation, as well as stiff enough to prevent significant prying on the bolts. In Figure 3.8, effective stresses (von Mises stresses) in the U-plates were found to momentarily approach the steel yield stress (50 ksi) just prior to bolt rupture (Figure 3.8c), but then return to elastic levels afterward. Such results indicate that the 3/8-in. thickness of the U-plates was reasonably optimized in regard to balancing the need for adequate strength and stiffness against the competing need for minimizing mass (thereby minimizing occupant risks).

Occupant risk measures (OIV, ORA) determined from the head-on (0 deg.) impact simulation indicated favorable values in comparison to MASH limits. In Figure 3.9, the occupant impact velocity (OIV) at 2 ft. of flail displacement (recall Table 2.1) was not only less than the maximum value permitted by MASH, it was also well below the preferable limit set by MASH. In regard to occupant ridedown acceleration, MASH defines ORA as being the maximum vehicle acceleration (or 'deceleration') that occurs *after* the occupant has impacted the vehicle compartment (i.e., has traveled 2 ft. longitudinally relative to the vehicle). Since maximum vehicle decelerations for breakaway hardware typically occur *before* the 2-ft flail displacement has been reached, ORA values (i.e., maximum decelerations *after* occupant impact) for such devices are often negligible in comparison to the AASHTO MASH limits. ORA results for the Figure 3.7 simulation were consistent with this trend and were found to be of negligible magnitude. (Note that both deceleration data and ORA values from experimental impact tests will be presented in detail later in this report, and will confirm that the ORA values were negligible in comparison to MASH limits.)

3.3.2 Single-post, oblique (25 deg.) impact loading performance

To assess the impact performance of the proposed breakaway connection under an oblique single-post impact condition, a MASH-compliant 25-deg., 19-mph (30-kph) impact simulation was conducted. In Figure 3.10, renderings of the finite element simulation results are presented at various points in time during the impact. An important consideration in conducting oblique impact simulation is assessing the potential for breakaway component snagging and abrupt vehicle deceleration. For the proposed connection design, the results in Figure 3.10 indicate that the 'downstream' collar-half cleared the stub (i.e., the portion of post below the slip plane) without snagging. In the earlier BDK75-977-40 design, ensuring this type of 'clean exit' behavior under oblique impact conditions required that ¼ in. x ¼ in. x 3-½ in. steel bars be welded to the collar primary plates at four separate locations. In the updated high-capacity connection design (Figure 3.6), the need for these bars (and the associated welding) was eliminated. Instead, by carefully choosing the widths of the vertical legs of the U-plates, the inner surfaces of these plates were able to serve as the necessary lateral-confinement mechanisms.

As was the case for the head-on (0 deg.) condition, occupant risk measures determined from the oblique (25 deg.) impact simulation were very favorable. In Figure 3.11, the occupant impact velocity (OIV) was found to be well below the corresponding MASH preferable limit.

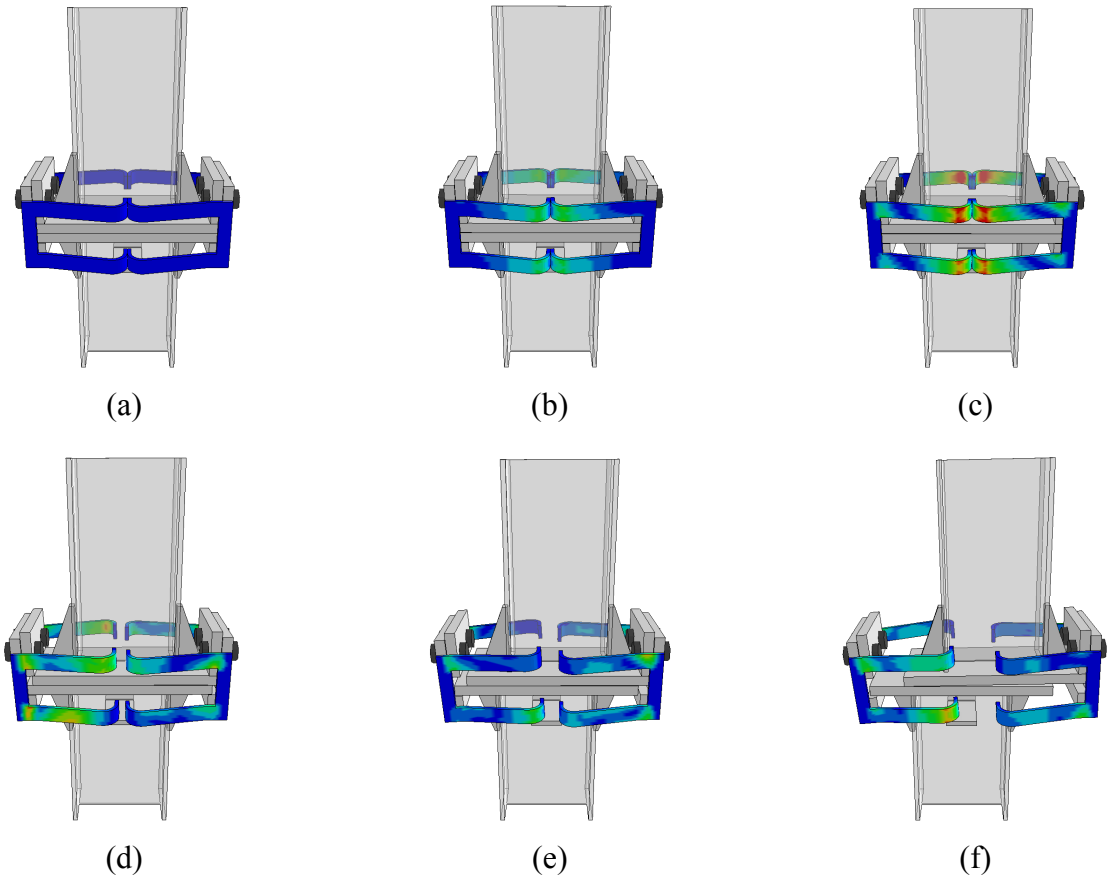

Figure 3.8 Effective stresses (von Mises stresses) in bent U-plate components of breakaway connection during head-on (0 deg.) 19-mph impact (crushable nose impactor not shown for clarity)
(Legend: blue = 0 ksi; red = 50 ksi = Fy)

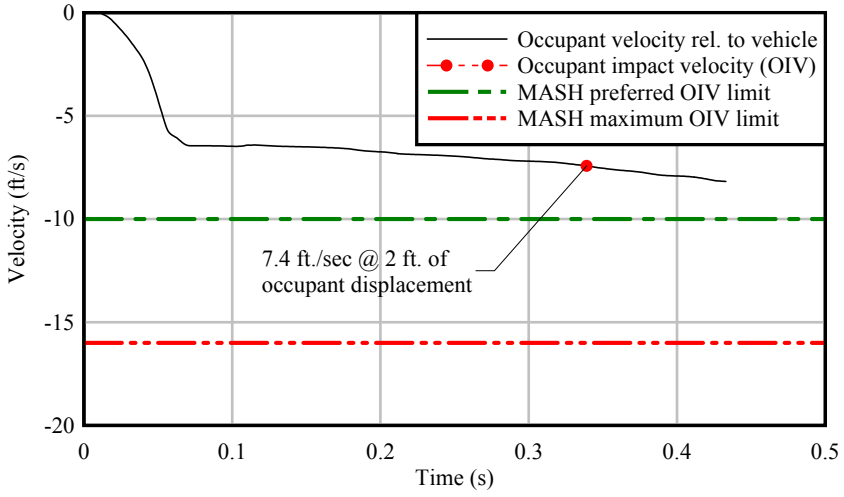

Figure 3.9 Occupant impact velocity (OIV) for head-on (0 deg.) 19-mph impact

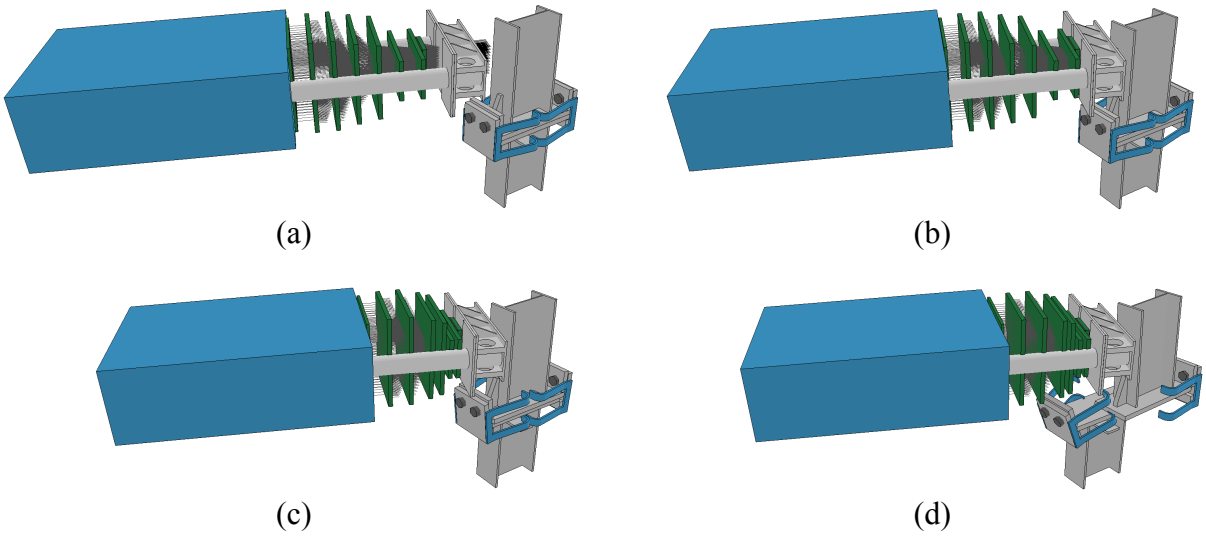

Figure 3.10 Simulation of breakaway connection response to oblique (25 deg.) 19-mph impact (upper portion of post and channel included in simulation but omitted from figure)

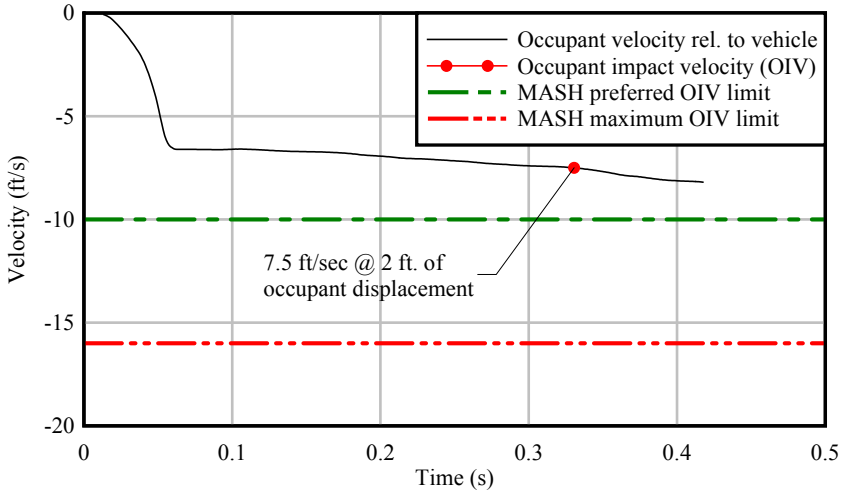

Figure 3.11 Occupant impact velocity (OIV) for oblique (25 deg.) 19-mph impact

3.3.3 Three-post sign structure, head-on (0 deg.) impact loading performance

To assess occupant risk measures (OIV, ORA, vehicle compartment intrusion) for a full sign structure consisting of multiple posts with an attached sign panel, a head-on (0 deg.) low-speed (19 mph) 1100C impact against a three-post high-capacity sign structure was modeled (Figure 3.12) and simulated (Figure 3.13). This head-on, low-speed impact condition was deemed to be among the worst-case scenarios in regard to maximizing OIV, ORA, and risk for vehicle compartment intrusion. Occupant impact velocity data from the simulation (Figure 3.14) were larger in magnitude than the velocity data obtained from the earlier single-post head-on simulation (Figure 3.9), but remained within the maximum limit permitted by MASH (16 ft/sec, recall Table 2.1).

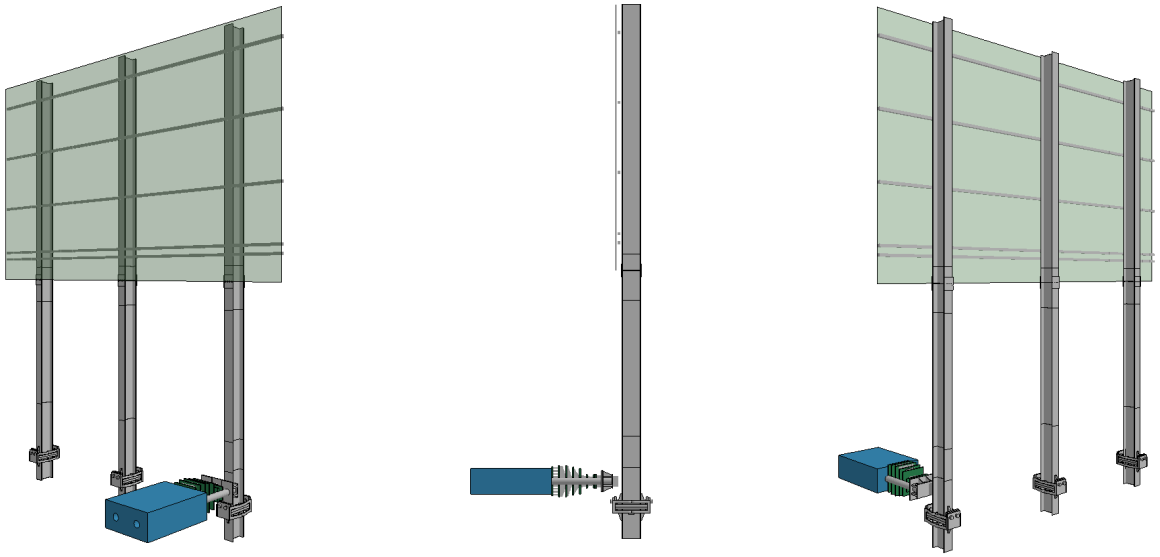

Figure 3.12 Three-post sign structure system model:
(a) Isometric upstream view; (b) Elevation view; (c) Isometric downstream view

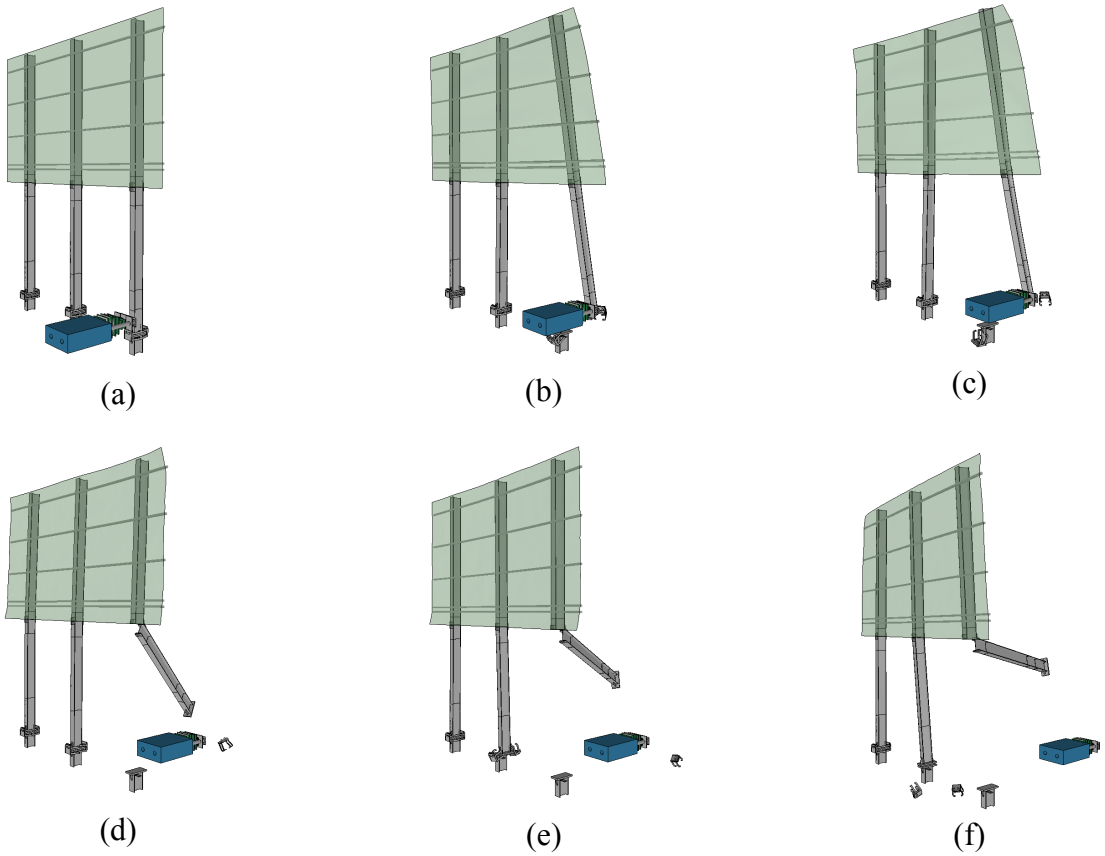

Figure 3.13 Three-post sign structure response to head-on (0 deg.) 19-mph impact

After breaking the high-capacity connection (Figure 3.13b), the 1100C vehicle continued to slow (i.e., decelerate) as it remained in contact with the lower-segment of the post, and loaded the fuse-plate in tension. Maximum OIV (15.2 ft/sec) was reached when the fuse-plate ruptured (Figure 3.13c). Following this rupture, the lower-segment of post swung out of the path of the vehicle (Figure 3.13d-f), thus eliminating the potential for vehicle compartment intrusion (recall Table 2.1). To ensure that fuse-plate rupture was not prematurely averted by potential plastic-hinging of the bottom transverse aluminum Z-beam (i.e., 'wind beam'), it was determined that the use of double Z-beams was preferable at the base of the sign panel (Figure 3.12). As noted in Section 3.3.1, occupant ridedown acceleration (ORA) was not a controlling parameter in the impact, and was in fact well below the MASH preferable limit (Figure 3.15).

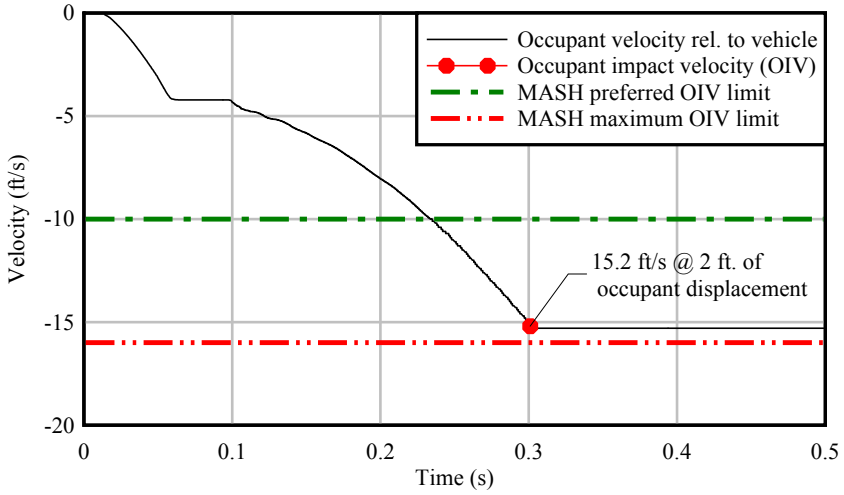

Figure 3.14 Occupant impact velocity (OIV) for head-on (0 deg.) 19-mph impact on three-post sign structure system

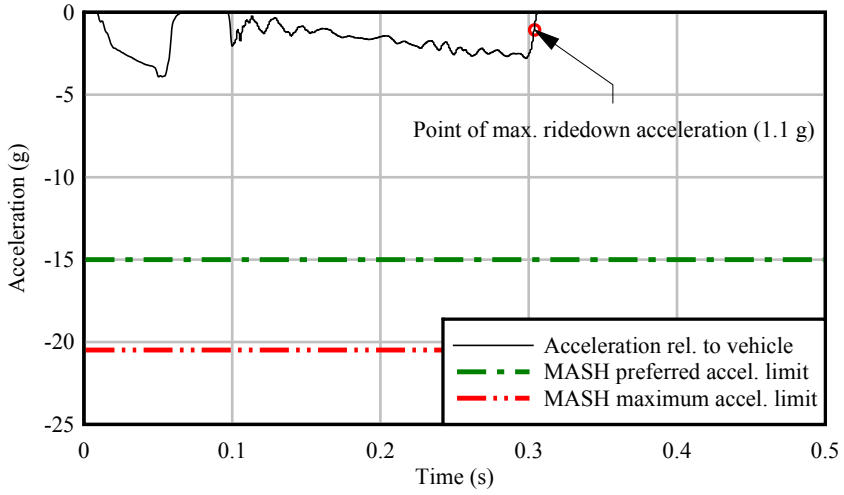

Figure 3.15 Occupant ridedown acceleration (ORA) for head-on (0 deg.) 19-mph impact on three-post sign structure system

3.3.4 Wind loading performance

As described earlier, the design flexural strength (for wind loading) of the high-capacity breakaway connection was defined as 80 kip-ft (recall Table 2.3). For breakaway supports, AASHTO LTS-6 requires that the *ultimate flexural strength* of a device exceed the *design flexural strength* by a factor of safety FS=1.5. To analytically demonstrate that the high-capacity breakaway connection possessed an ultimate flexural strength in excess of (FS=1.5)(80 kip-ft) = 120 kip-ft, a quasi-static nonlinear pushover analysis—of the type previously shown in Figure 3.4a—was performed. Results from the finite element simulation (Figure 3.16) indicated that yielding first occurred at the junction between the tension-side triangular stiffener and the upper flange plate. With additional loading, the zone of yielding spread until eventually the plastic capacity of the connection system was reached.

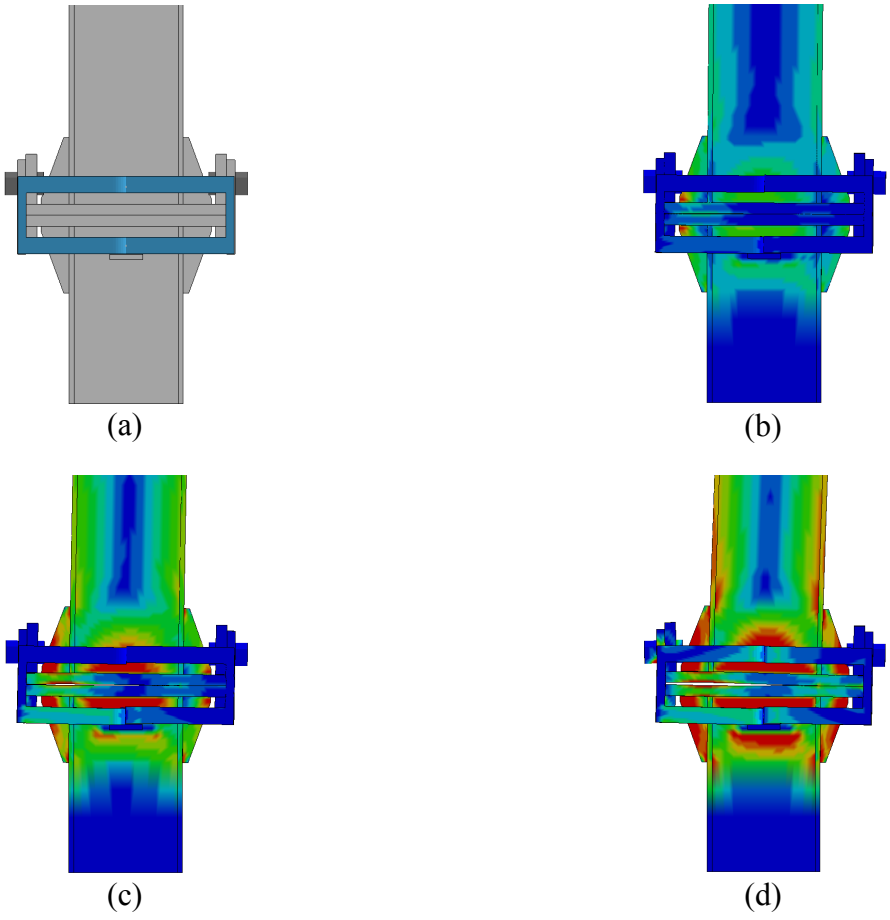

Figure 3.16 Effective stresses (von Mises stresses) in connection components during quasi-static pushover analysis:
(a) Unstressed model; (b) Initiation of yielding at tip of tension-side stiffener;
(c) Initiation of yielding in flange plates; (d) Ultimate flexural capacity condition
(Legend: blue = 0 ksi; red = 65 ksi = σ_{ULT} ; Fy = 50 ksi)

In Figure 3.17, moment-rotation data—determined as shown earlier in Figure 3.4b—from the pushover analysis are compared to the design moment (80 kip-ft) and to the ultimate moment required by AASHTO LTS-6 (120 kip-ft). Evident from the figure, the breakaway connection possessed an ultimate flexural strength (132 kip-ft) that exceeded the AASHTO required value by 10%. In regard to this 10% surplus of capacity, it is worth noting that the nonlinear constitutive relationship used in the finite element model employed a yield point of Fy=50 ksi. For A572 Gr. 50 steel, from which the connection system was later fabricated, 50 ksi is the *minimum* yield strength. As actual yield strengths for A572 Gr. 50 steel will nearly always exceed the minimum specified value of 50 ksi, the buffer between the ultimate strength of the breakaway connection and the AASHTO required strength was expected to exceed 10% in most practical cases. In fact, subsequent experimental testing of the high-capacity connection—presented in the following chapter—confirmed that the capacity surplus exceeded 10%.

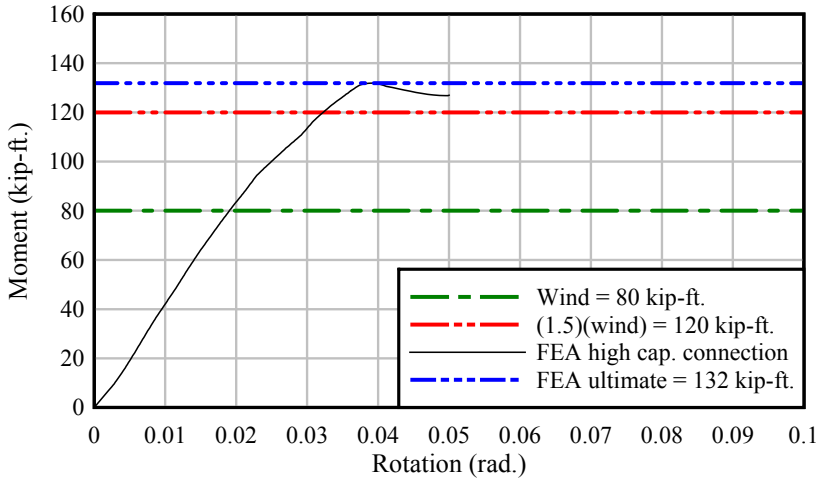

Figure 3.17 Results from quasi-static finite element pushover analysis of high-capacity connection

3.4 Summary

Results from the finite element impact simulations and quasi-static flexural capacity simulations presented in this chapter suggested that the high-capacity system detailed in Appendix B would meet the impact performance requirements of AASHTO MASH and the flexural capacity requirements of AASHTO LTS-6. Consequently, based on the analytical findings, physical validation of breakaway connection performance was undertaken in the form of experimental impact testing and flexural testing, as described in the following chapter.

CHAPTER 4
TESTING OF HIGH-CAPACITY SYSTEM

4.1 Introduction

Based on the fabrication drawings of the high-capacity breakaway connection (Appendix B), single-post test articles were fabricated for use in both dynamic impact testing and static flexural capacity testing. The test articles fabricated for use in *impact* testing (Figure 4.1a-c) were produced by Boone Welding in Gainesville, Florida, and were galvanized (Figure 4.1d) so as to be consistent with intended field-installation conditions. After galvanizing, all components were delivered to the FDOT Structures Research Center in Tallahassee, Florida, and assembled for testing. To further maintain consistency with intended field-installation conditions, 0.02-in. thick Teflon sheets (recall Section 3.3) were installed at five (5) sliding-interface locations (see Appendix B) during the assembly of each high-capacity breakaway connection test article. Such Teflon sheets were included in the assembly of systems subjected to impact testing as well as those subjected to static flexural testing.

(a)

(b)

(c)

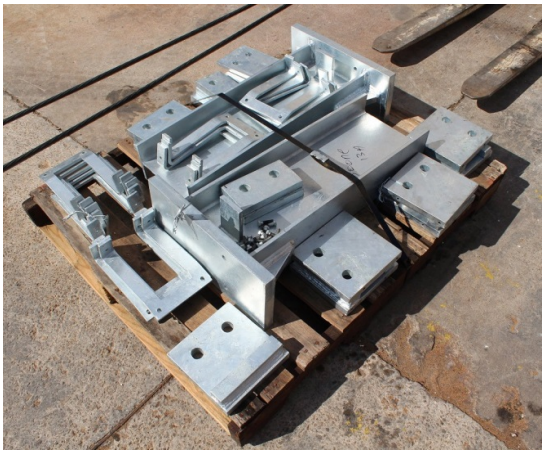

(d)

Figure 4.1 Fabrication and galvanizing of high-capacity connection components: (a) Collar components; (b) U-plates; (c) Stubs; (d) Galvanized components

4.2 Impact testing

All impact tests of the high-capacity breakaway connection system were conducted using the impact pendulum (Figure 4.2) located at the FDOT Structures Research Center in Tallahassee, Florida. Test conditions were consistent with the MASH specifications summarized in Table 2.1, and were conducted on single-post test articles at impact angles of 0 deg. (head-on) and 25 deg. (oblique). The MASH compliant UF/FDOT 1100C crushable-nose surrogate vehicle (Consolazio et al., 2016; Groetaers et al., 2016) was used in all tests, and a drop height of 12 ft (Figure 4.3) was used to produce an impact speed of 19 mph (30 kph). To approximate the influence that sign panel mass—but *not* sign panel stiffness—would have in a multi-post sign structure, a steel channel was attached to the upper segment of each single-post test article. In each case, the channel mass was calibrated to be equal to the tributary mass of sign panel that would be associated with an interior post in a 3-post sign structure.

Figure 4.2 High-capacity breakaway connection test article installed at the FDOT pendulum impact test facility (FDOT Structures Research Center, Tallahassee, Florida)

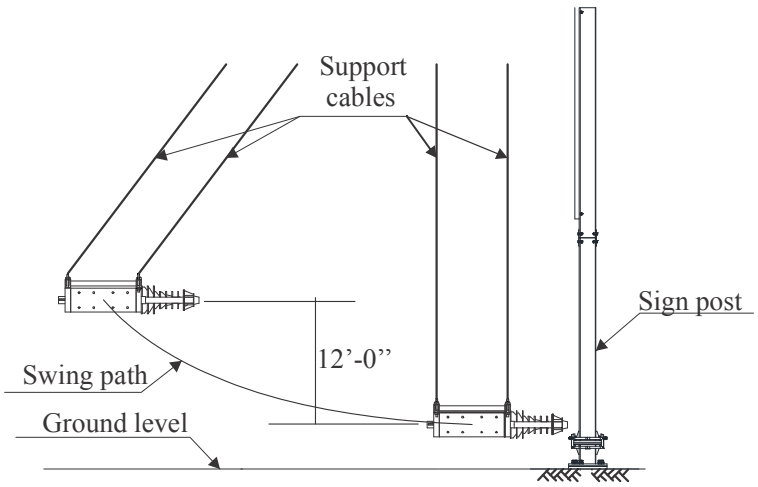

Figure 4.3 Schematic diagram of pendulum impact test setup

4.2.1 Instrumentation

High-speed data acquisition systems were used to record data from high-speed video cameras, and from a collection of sensors. Specific items of instrumentation that were employed during each test included:

- Uniaxial accelerometers (50 g, quantity =2) on the back block of the surrogate vehicle
- Uniaxial accelerometer (250 g, quantity =1) on the impact head of the surrogate vehicle
- High speed video cameras (zoomed view, and wide angle view, quantity = 2)
- Emitter/receiver pairs of infrared optical break beam sensors (quantity = 2)
- A tape switch affixed to the impact face of the test article (steel post)

Both of the high speed video cameras recorded data at a rate of 2000 frames/sec. All remaining sensors (accelerometers, etc.) were sampled and recorded at a frequency of 10 kHz.

4.2.2 Head-on (0 deg.) impact test

On February 8, 2016, an integrated test article—consisting of a stub, high-capacity breakaway collar connection, lower-segment of post, fuse/hinge plates, and upper-segment of post—was installed (Figure 4.4) and subjected to a head-on (0 deg.) 19 mph impact from the UF/FDOT 1100C surrogate vehicle (Figure 4.5). In accordance with the dimensions of the Kia Rio production vehicle from which the surrogate vehicle was developed, the impact elevation (mid-height of the impact head) on the lower-post was 18 in. above the theoretical ground plane (i.e., 14 in. above the slip plane in the breakaway connection, leaving a 4 in. permanent stub, as permitted by AASHTO MASH).

In Figure 4.6, frames from high speed video of the head-on impact test confirmed that the two halves of the moment collar broke apart cleanly—as intended—after the tension bolts holding them together reached their rupture loads. On the upstream (impact) side, one collar-half remained with the stub and dropped to the ground. On the downstream (non-impact) side, the other collar-half cleared the stub without snagging and traveled with the lower-post.

AASHTO MASH states that detached (breakaway) elements—e.g., the downstream collar half—are not permitted to penetrate the vehicle occupant compartment or present an undue hazard to other traffic, pedestrians or nearby personnel. Since the trajectory of the downstream collar half is *away* from the impacting vehicle, the risk of vehicle compartment penetration is negligible. Furthermore, the downstream collar travels in the *same direction* that the vehicle travels after passing beneath the sign structure (recall Figure 1.2). In a pendulum impact test, forward motion of the surrogate vehicle is halted by gravitational resistance (caused by the upward arc of the swing path). However, in a roadside environment, the vehicle will—by design—continue traveling past the sign structure, thus essentially following the path of downstream collar half. While a finite level of risk is acknowledged to be associated with the motions of both the vehicle and of the downstream collar half, ‘undue hazards’ are not deemed to be introduced by such motions.

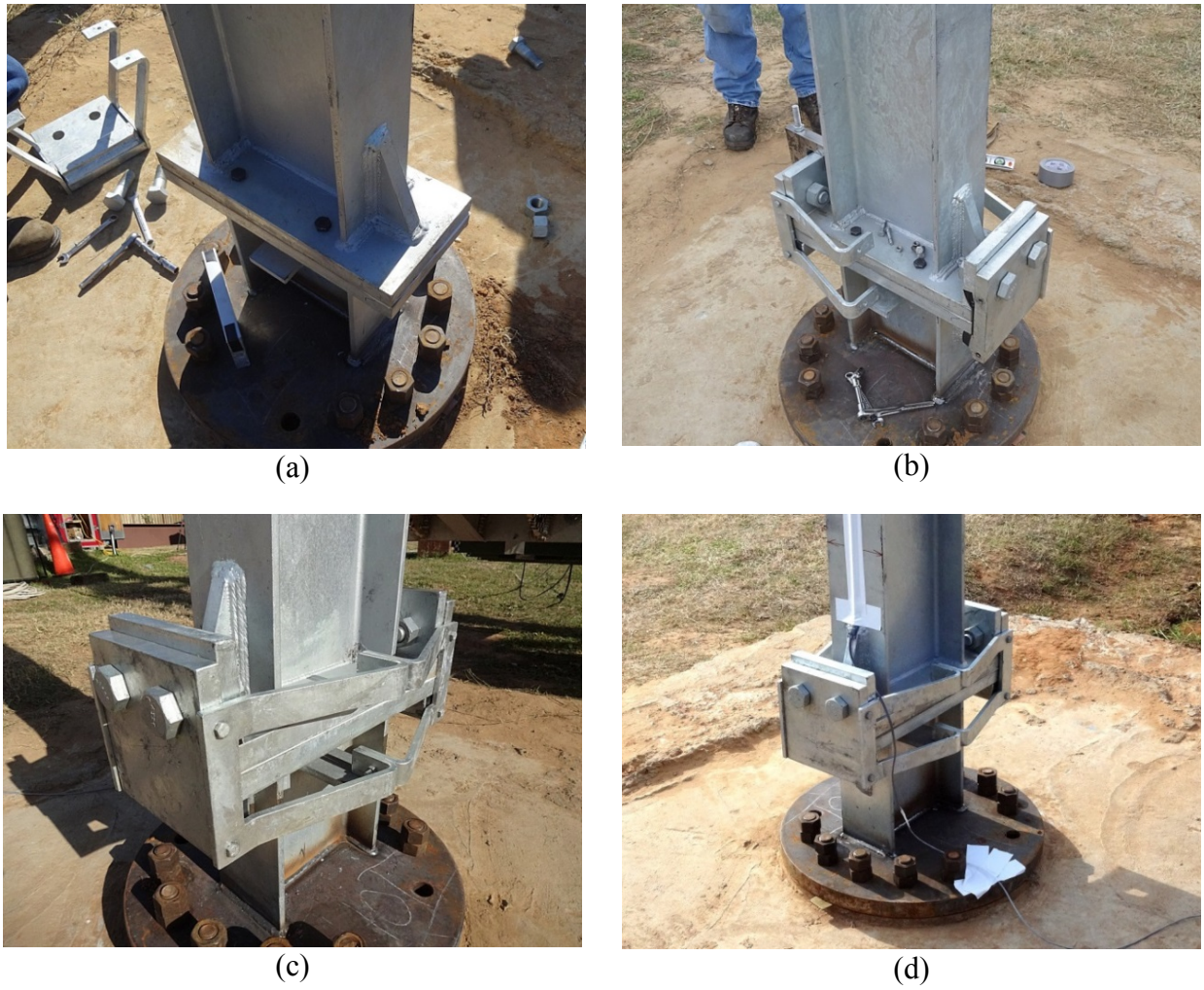

Figure 4.4 Installation of test article for head-on (0 deg.) impact test:
(a) Post mounted to stub with temporary fit-up bolts; (b) Collar installation in progress;
(c) Collar installed (non-impact face shown); (d) Collar installed (impact face shown)

In Figure 4.7, frames from the wide angle high speed video again show clean separation of the post from the stub. In contrast to a 'full' multi-post and sign panel system, where the stiffness of non-impacted posts restrains rotation of the upper-segment of the impacted post (recall Figure 1.3), no such stiffness was present in the single-post test setup. Consequently, there was insufficient resistance to break the fuse plate at mid-height, and therefore the entire post (lower and upper segments) rotated and landed (Figure 4.8) as a single entity. As shown in Figure 4.8b, the collar components underwent minimal permanent deformation; only the previously-flush legs of the U-plates were left slightly out of alignment (due to the force required to break the tension connector bolts).

(a)

(b)

(c)

Figure 4.5 Head-on (0 deg.) impact test:
(a) Fully-installed test article; (b) Elevation view; (c) Isometric view

Acceleration data from two 50g accelerometers mounted on the 1100C surrogate vehicle back block were averaged together and time-integrated (using trapezoidal integration) to compute the occupant impact velocity (OIV), which was found to be 9.27 ft/sec (Figure 4.9). For comparison, AASHTO MASH specifies a preferred OIV limit of 10 ft/sec and a maximum permissible limit of 16 ft/sec. AASHTO MASH also limits the maximum occupant ridedown acceleration (ORA) to 20.49 g, but sets the preferred limit at 15 g. Examining the acceleration data in Figure 4.10 after the time of occupant impact (i.e., $t = 0.26$ sec for this test), the maximum occupant acceleration levels are found to be negligible in comparison to the AASHTO preferred ORA limit of 15 g. Hence the experimental OIV and ORA were both well within the permissible limits established by AASHTO MASH.

To compare the experimental occupant impact velocity data to corresponding FEA results, simulation data previously reported in Figure 3.9 are repeated in Figure 4.9. In general, the time-varying trends of occupant impact velocities (experimental and FEA) were in reasonable agreement. However, peak achieved velocities differed by approximately 25%, with the experimental OIV being closer to the MASH preferred limit than the FEA OIV. It is hypothesized that this discrepancy originated from differences in assumed versus actual rupture strength of the 5/16-in. diameter tension connector bolts that hold the collar-halves together. In the FEA simulation, the minimum specified bolt rupture strength was employed, whereas the actual strengths of the bolts used during experimental testing likely exceeded this minimum permissible value.

(a) (b) (c)

(d) (e) (f)

Figure 4.6 High speed video frames from head-on (0 deg.) 19-mph impact test

(a) (b) (c)

(d) (e) (f)

Figure 4.7 Wide angle high speed video frames from head-on (0 deg.) 19-mph impact test

(a)

(b)

(c)

Figure 4.8 Components of test article after head-on (0 deg.) 19-mph impact test: (a) Lower and upper segments (still joined by fuse and hinge plates); (b) Overhead view of minimal deformations in collar U-plates; (c) Isometric view of collar with U-plates

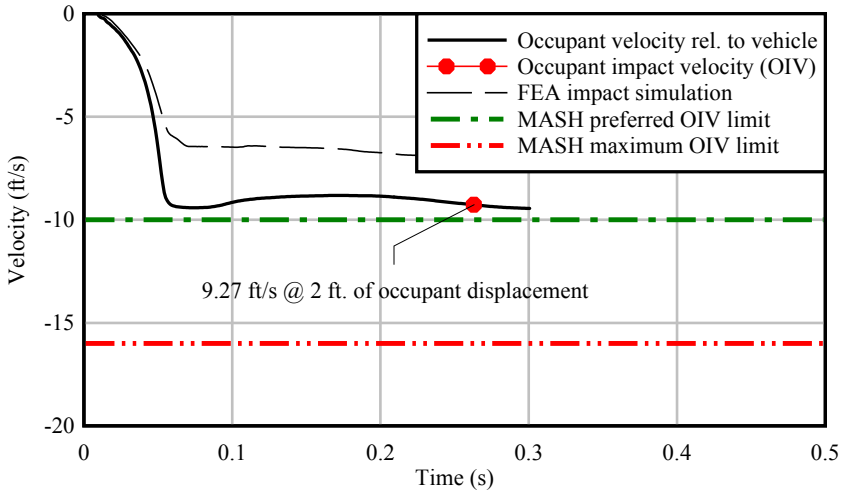

Figure 4.9 Occupant impact velocity (OIV) from head-on (0 deg.) 19-mph impact test

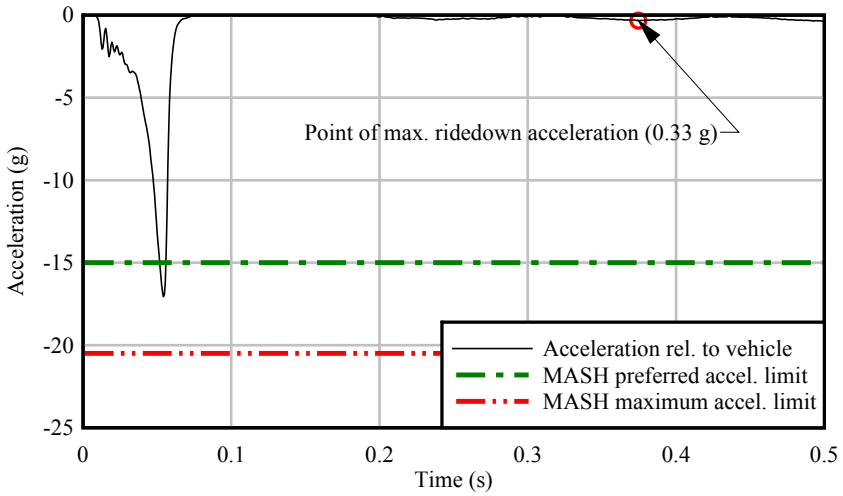

Figure 4.10 Occupant ridedown acceleration (ORA) from head-on (0 deg.) 19-mph impact test

4.2.3 Oblique (25 deg.) impact test

On February 10, 2016, an oblique angle (25 deg.) impact test (Figure 4.11) was performed to assess the potential for breakaway component snagging and abrupt vehicle deceleration. In Figure 4.12, frames from high speed video of the oblique impact test confirm that no significant snagging occurred. After the two halves of the moment collar broke apart, the downstream (non-impact) collar-half momentarily interacted with (contacted) the downstream vertical flange of the stub (Figure 4.12c). However, this contact was brief in duration, and did not prevent the collar-half from continuing to travel with the lower-post segment, eventually clearing the stub. In Figure 4.13, frames from wide angle high speed video again show clean separation of the post from the stub. Similar to the head-on (0 deg.) impact, in the oblique (25 deg.) impact test, there was insufficient inertial (mass-related) resistance in the upper segment to break the fuse plate at mid-height, thus the entire post (lower and upper segments) rotated as a single entity. In Figure 4.14, the brief contact interaction noted above resulted in non-uniform (unsymmetric) permanent deformations of the U-plate legs but no other noticeable damage.

Acceleration data from two 50-g accelerometers mounted on the 1100C surrogate vehicle back block were averaged together and time-integrated (using trapezoidal integration) to compute the occupant impact velocity (OIV), which was found to be 9.1 ft/sec (Figure 4.15). For comparison, AASHTO MASH specifies a preferred OIV limit of 10 ft/sec and a maximum permissible limit of 16 ft/sec. Maximum occupant ridedown acceleration (ORA) occurring after the time of occupant impact (i.e., $t = 0.27$ sec for this test) was found to be negligible in comparison to the AASHTO MASH preferred ORA limit of 15 g, or the maximum limit of 20.49 g. Hence the experimental OIV and ORA were both well within the permissible limits established by AASHTO MASH.

To compare the experimental occupant impact velocity data to corresponding FEA results, simulation data previously reported in Figure 3.11 are repeated in Figure 4.15. While the trends of occupant impact velocities were in reasonable agreement, peak achieved velocities differed by approximately 20%, with the experimental OIV being closer to the MASH preferred limit than the FEA OIV. As noted earlier, this discrepancy is attributed to probable differences in assumed versus actual rupture strength of the 5/16-in. diameter tension connector bolts.

(a)

(b)

(c)

Figure 4.11 Oblique (25 deg.) impact test:
(a) Fully-installed test article; (b) Isometric view; (c) Overhead view at impact point

(a)

(b)

(c)

(d)

(e)

(f)

Figure 4.12 High speed video frames from oblique (25 deg.) 19-mph impact test

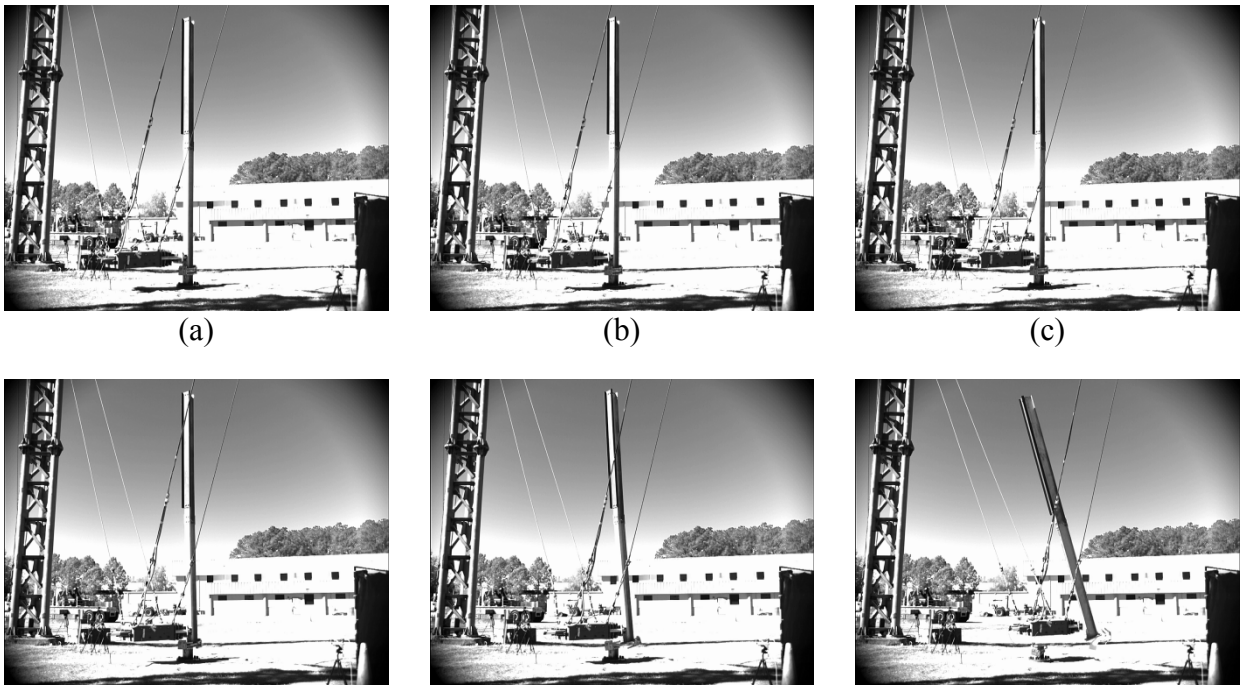

Figure 4.13 Wide angle high speed video frames from oblique (25 deg.) 19-mph impact test

Figure 4.14 Collar components of test article after oblique (25 deg.) 19-mph impact test:
(a) Isometric view collar-halves; (b) Overhead view showing U-plate deformations

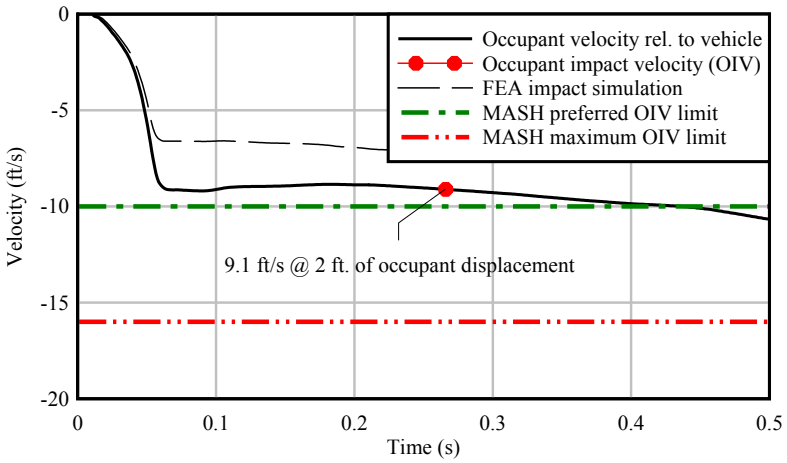

Figure 4.15 Occupant impact velocity (OIV) from oblique (25 deg.) 19 mph impact test

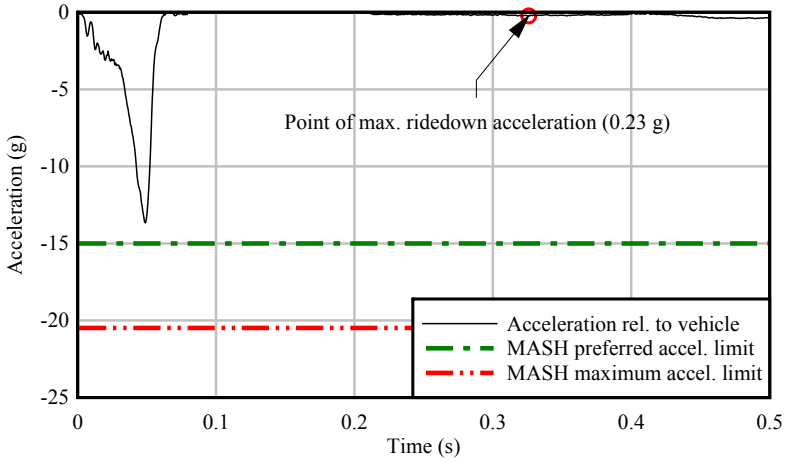

Figure 4.16 Occupant ridedown acceleration (ORA) from oblique (25 deg.) 19 mph impact test

4.3 Fuse plate testing

In the single-post pendulum impact tests described above, it was not feasible to account for structural stiffness that would be associated with either a sign panel or adjacent (non-impacted) posts in a multi-post sign structure. Consequently, the single-post pendulum impact tests did not produce the type of fuse plate rupture that occurs during vehicle collision with multi-post structures (recall Figure 1.3). Hence, to collect experimental data for use in validating finite element simulations of vehicle impacts with *multi*-post sign structures, a special-purpose test setup (Appendix E) was developed in which pendulum impact energy was used to rupture fuse plates in a controlled and predictable manner. In each such test, validation data consisting of fuse plate elongations, strains, and rupture point were determined.

Since fuse plate rupture is a dynamic (i.e., rate-dependent) phenomenon, it was important that the tensile loading rate of the fuse plate in the test setup be similar to that which would occur in a multi-post sign structure during vehicle impact. Thus, to establish a suitable 'target' tensile loading rate for the fuse plate tests, time-histories of fuse plate tensile forces were computed using a finite element simulation of an 1100C surrogate vehicle striking a three-post high-capacity sign structure (Figure 4.17). As documented in the structural drawings of the high-

capacity connection (Appendix B), each breakaway sign post incorporates a single fuse plate and a single hinge plate (Figure 4.17a), the details of which are shown in Figure 4.18. In the fuse plate (Figure 4.18a), a *net-section rupture plane* was formed by perforating the plate with four (4) 1-in. diameter holes. Additionally, in both the fuse plate and hinge plate, four (4) corner holes were also included for bolts that connect the plates to the flanges of the W10x26 sign post.

For purposes of finite element modeling, areas around the perforation holes in the fuse plate were discretized using a high resolution mesh (Figure 4.19), thus allowing accurate representation of steel necking and fracture. In contrast, the corner holes in the plate, and corresponding bolts, were modeled in a simplified manner using individual 'nodal rigid bodies' (LSTC, 2016) of appropriate size.

In the fuse plate test setup, impact energy from a 2420-lbf (1100-kg) impact block was used to rupture each fuse plate in a predictable time-varying manner. The back block of the impactor (Figure 4.20) was identical to the back block of the 1100C MASH compliant surrogate vehicle described earlier, however the crushable nose differed significantly. To generate an incrementally increasing tensile force on the fuse plate, over a targeted time duration of 0.1 sec., a series of rectangular crushable aluminum honeycomb cartridges (Figure 4.21) were sized using an energy-based design procedure. Force-deformation characteristics for each cartridge were incorporated into a finite element model of the test setup, and impact simulations were conducted (Figure 4.22).

The simulations analytically confirmed that the target tensile loading rate of the fuse plate would be achieved with the proposed test setup. Additionally, the results revealed a potential safety issue with respect to the planned experimental testing. It was found that after fuse plate rupture, and post rotation, the final position of the top of the post would be undesirably close to the return swing path of the impact block. To increase the clearance distance between these two objects (post and block), and thus avoid a potential secondary collision, the hinge plate was weakened by introducing a 2 in. diameter hole (Figure 4.23). With this modification, rotation of the post increased and the potential for a return-swing collision was eliminated.

On March 30, 2016, two repetitions of fuse plate testing were conducted (Figure 4.24). In each test (Test 1 and Test 2), tracking points were imprinted on the fuse plate being tested (Figure 4.24b) so that the recorded high speed video could later be processed into fuse plate elongation and strain data. Photos of the test article condition and fuse plate condition after impact Test 1 are shown in Figure 4.25 (results from Test 2 were similar). Steel yielding, necking, and plate fracture (Figure 4.25b) clearly occurred through the perforated net section of the fuse plate, as intended. In Figure 4.26 high speed video frames from both Test 1 and Test 2 are compared to results from a finite element impact simulation of the test conditions. Qualitatively, good agreement is observed between the experimental and analytical patterns of deformation and fracture.

To quantitatively compare the results, the motion tracking (digital image correlation) software Xcitex ProAnalyst was used to compute time-varying plate elongations along the measurement lines indicated in Figure 4.27. Plate strains were then computed from the elongation data, averaged together (across all three measurement lines), and correlated to time. In Figure 4.27, good agreement is observed in the experimental and analytical time histories of fuse plate strain, and in the times at which plate rupture occurred. Based on these results, the finite element simulation techniques used to analyze 'full' multi-post sign structure impacts (e.g., Figure 4.17)—wherein fuse plate rupture occurs—were deemed to be reasonably validated.

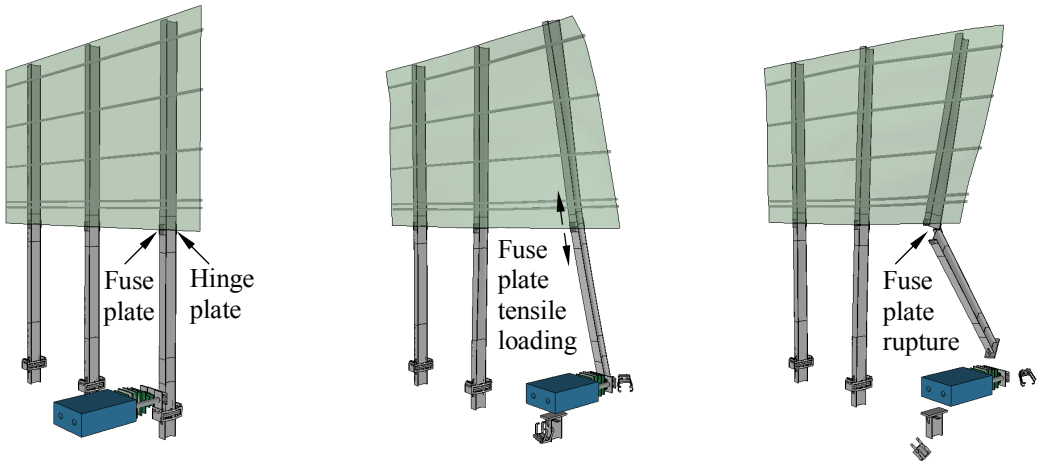

(a) (b) (c)

Figure 4.17 Simulation of head-on (0 deg.) 19-mph impact on 3-post sign structure: (a) Initial contact; (b) Fuse plate at rupture load; (c) Rotation of leg about hinge plate

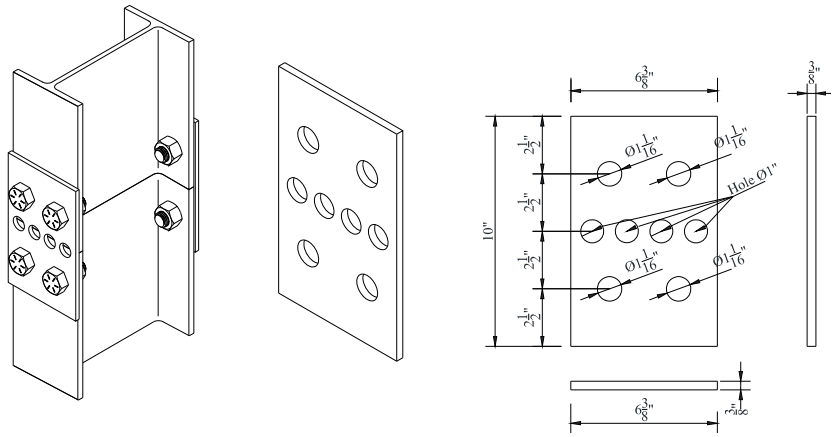

(a)

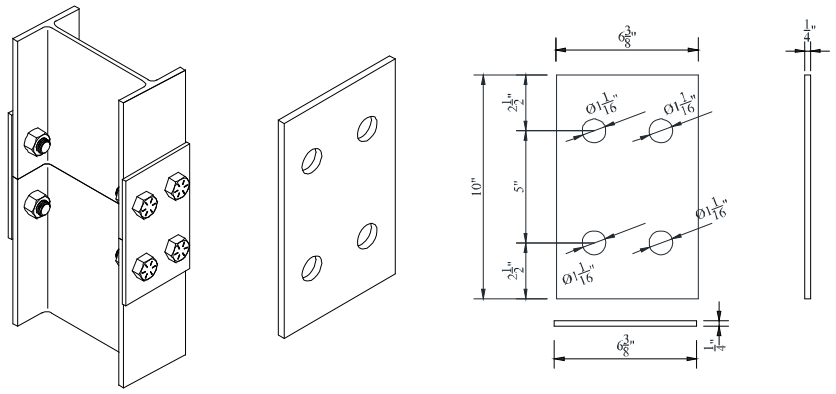

(b)

Figure 4.18 Fuse and hinge plate details: (a) Fuse plate; (b) Hinge plate

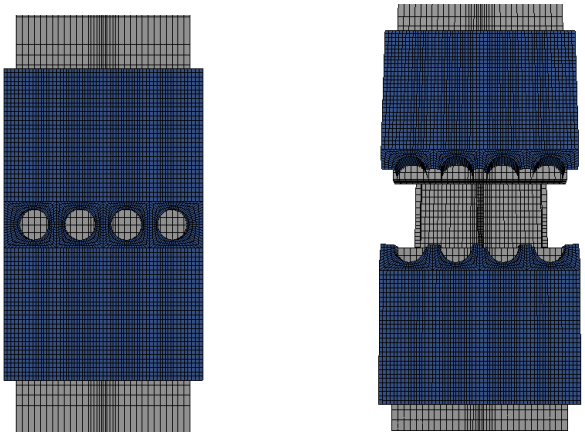

(a) (b)

Figure 4.19 Finite element model of fuse plate: (a) Before impact; (b) After rupture

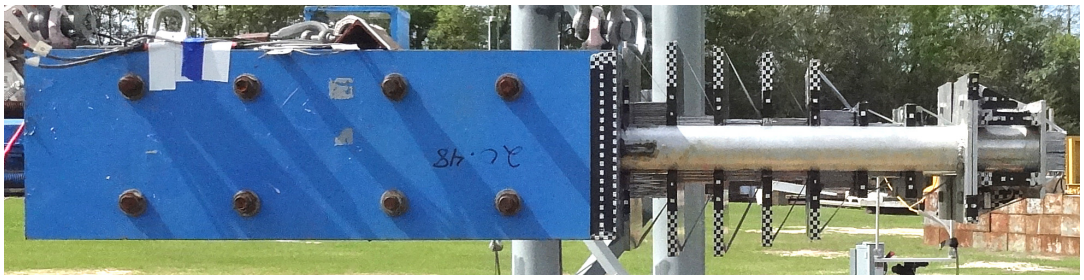

Figure 4.20 Elevation view of fuse plate impactor

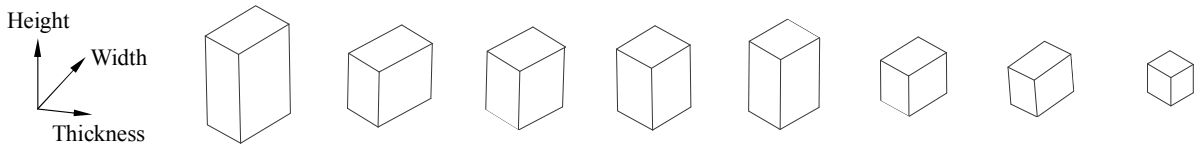

Cartridge #	8	7	6	5	4	3	2	1
Shape	Rect.	Rect.	Rect.	Rect.	Rect.	Rect.	Rect.	Rect.
<u>Compressive strength:</u>								
Specified	550 psi	550 psi	550 psi	550 psi	272 psi	272 psi	272 psi	272 psi
Actual	504 psi	504 psi	504 psi	504 psi	278 psi	278 psi	278 psi	278 psi
<u>Dimensions:</u>								
Height†	7.625 in.	5.50 in.	5.00 in.	5.00 in	6.25 in.	4.375 in.	4.00 in.	3.125 in.
Width†	5.00 in	5.00 in.	4.50 in.	3.625 in.	4.00 in.	4.00 in.	2.625 in.	3.00 in.
Thickness ‡	3.00 in.	3.00 in.	3.00 in.	3.00 in.	3.00 in.	3.00 in.	3.00 in.	3.00 in.

†Based on actual compressive strength, not specified strength.

‡Maximum thickness after cartridge pre-crushing. Material thickness prior to pre-crushing was 3.25 in.

Figure 4.21 Aluminum honeycomb cartridge dimensions
used in crushable nose of fuse plate impactor

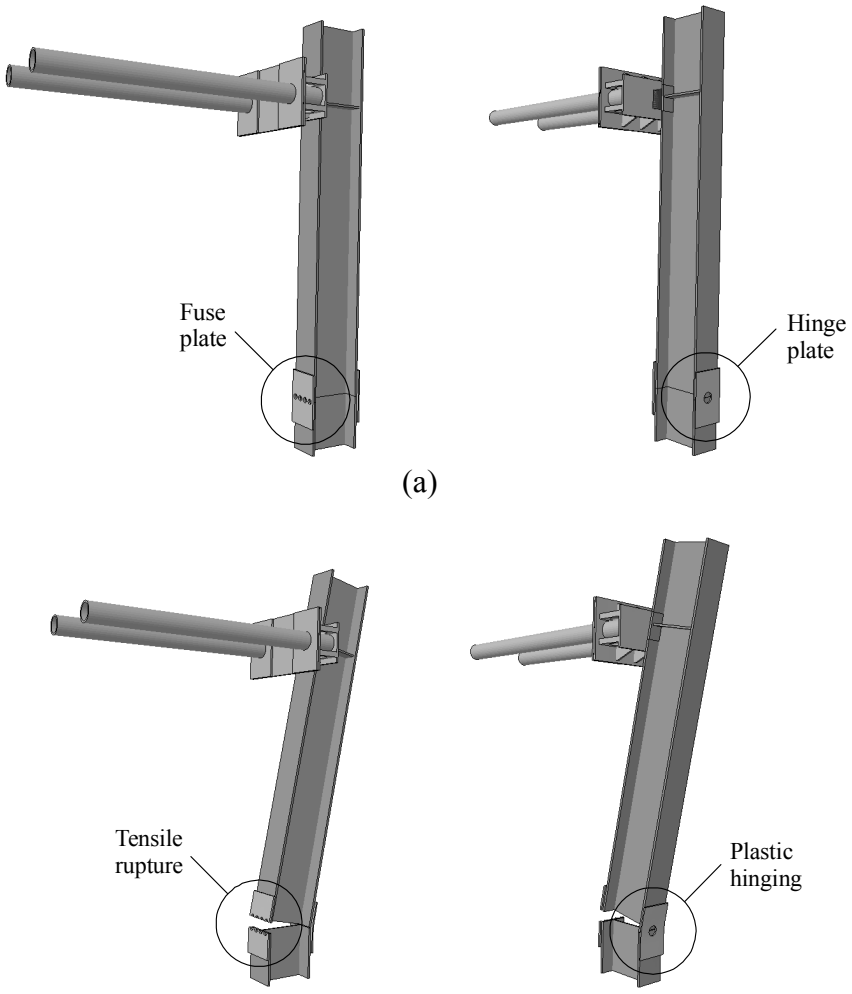

Figure 4.22 Finite element simulation of fuse plate test
(Head of impactor shown; back block of impactor omitted):
(a) Point of initial impact; (b) Tensile rupture of fuse plate

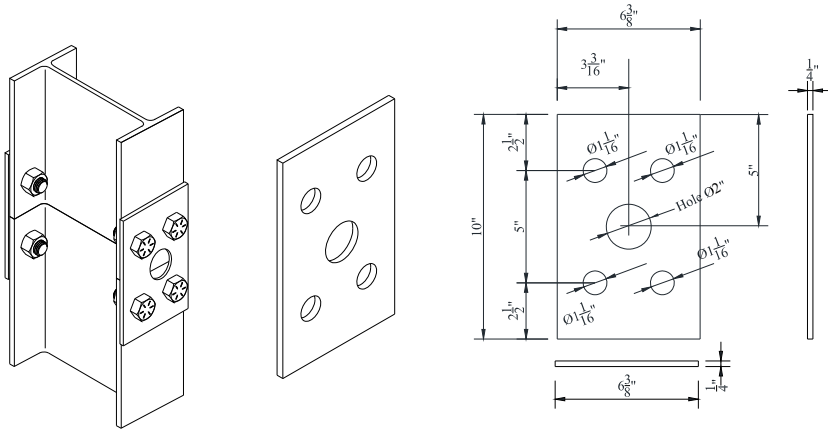

Figure 4.23 Modified hinge plate used in fuse plate test setup

(a)

(b)

(c)

(d)

Figure 4.24 Special-purpose fuse plate test setup:
(a) Overview of impactor, high-speed camera, and test article (fuse plate at bottom of post);
(b) Tracking points imprinted on fuse plate; (c) Fuse plate; (d) Modified hinge plate

(a) (b)

Figure 4.25 Final condition after impact Test 1: (a) Overall test article; (b) Fuse plate

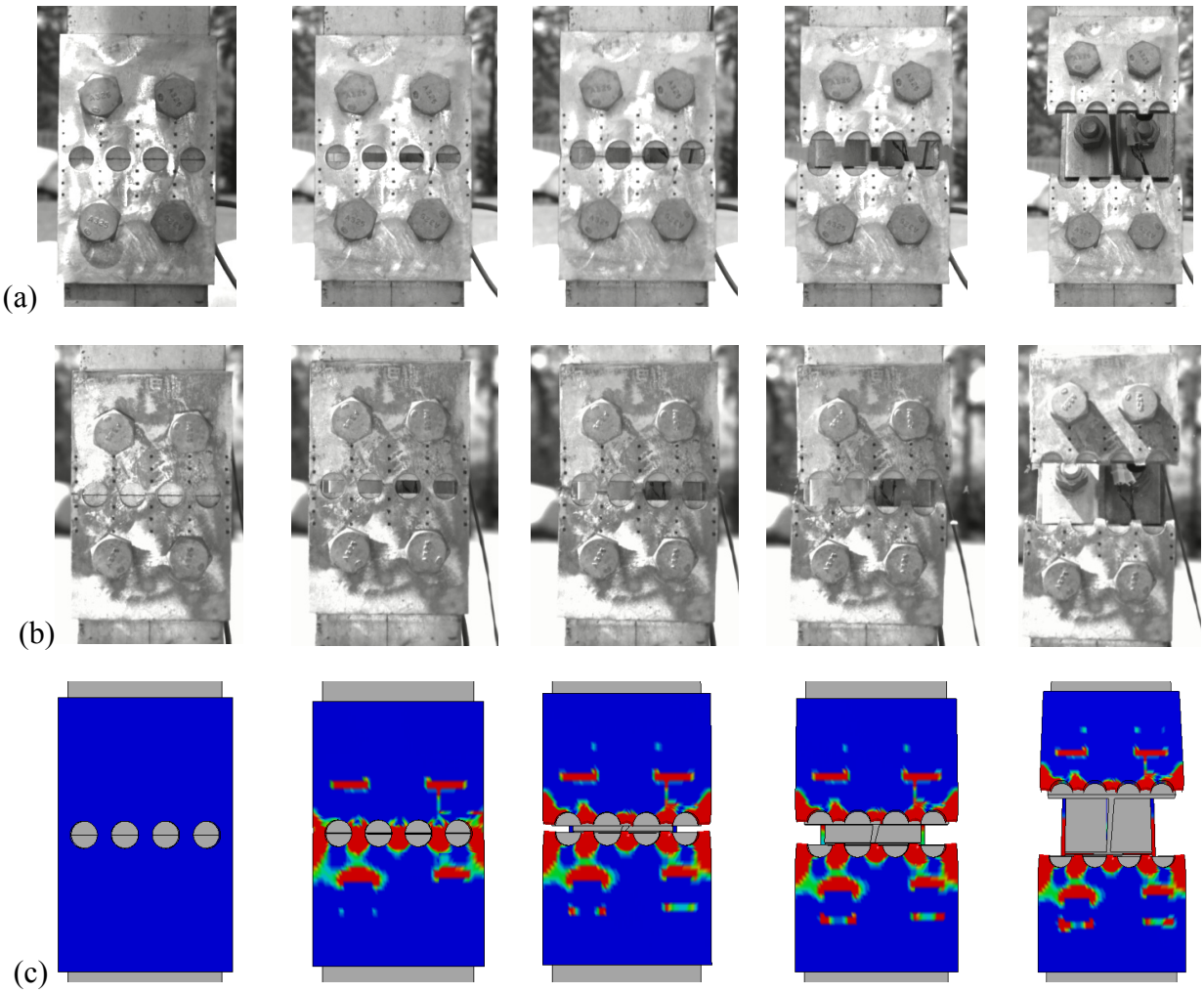

(a)

(b)

(c)

Figure 4.26 Fuse plate rupture: (a) Test 1 (speed = 17 mph); (b) Test 2 (speed = 16.6 mph); (c) Plastic strains from finite element simulation (speed = 17 mph; blue: $\varepsilon_P = 0$; red: $\varepsilon_P = \left(F_y/E\right) \cdot 10$)

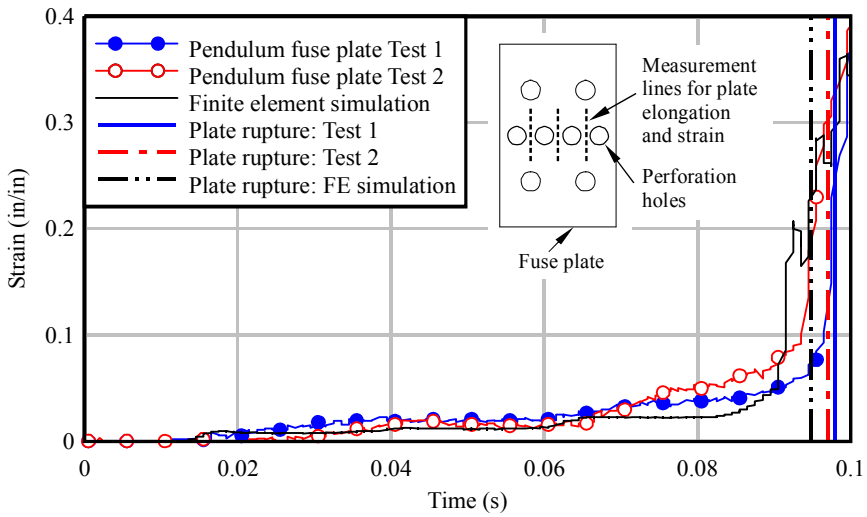

Figure 4.27 Comparison from fuse plate data from impact testing and corresponding finite element simulation

4.4 Static flexural testing

Static flexural testing of the high-capacity breakaway connection was conducted at the Structures Research Lab of the University of Florida. Per AASHTO LTS-6, laboratory testing was conducted to demonstrate that the breakaway system possessed an ultimate flexural strength factor of safety of at least FS=1.5, relative to the design wind capacity. Since the high-capacity system was designed to possess 80 kip-ft of design moment capacity (recall Table 2.3), static flexural testing was undertaken to demonstrate that the ultimate strength of the high-capacity breakaway connection was (FS=1.5)(80 kip-ft)=120 kip-ft or greater.

Two repetitions of static flexural testing (configured as shown in Figure 4.28) were conducted. Flexural test items consisted of four main components: a reaction frame, a W10x26 stub, the high-capacity moment collar, and a W10x26 post. Two ungalvanized test articles with 'mill scale' surface conditions were fabricated by Boone Welding (of Gainesville, Florida), delivered to the University of Florida, and assembled for testing. To maintain consistency with the intended field-installation conditions (see Appendix B), 0.02-in thick Teflon sheets were inserted at the flange-plate-to-flange-plate interface, and at all four (4) binding-plate-to-flange-plate interfaces. Importantly, the coefficient of friction for sliding of steel against Teflon is controlled *not* by the surface condition of the steel (ungalvanized or galvanized) but instead by the Teflon. Thus, inclusion of the Teflon sheets ensured that results obtained from flexural testing were not influenced by direct steel-to-steel sliding.

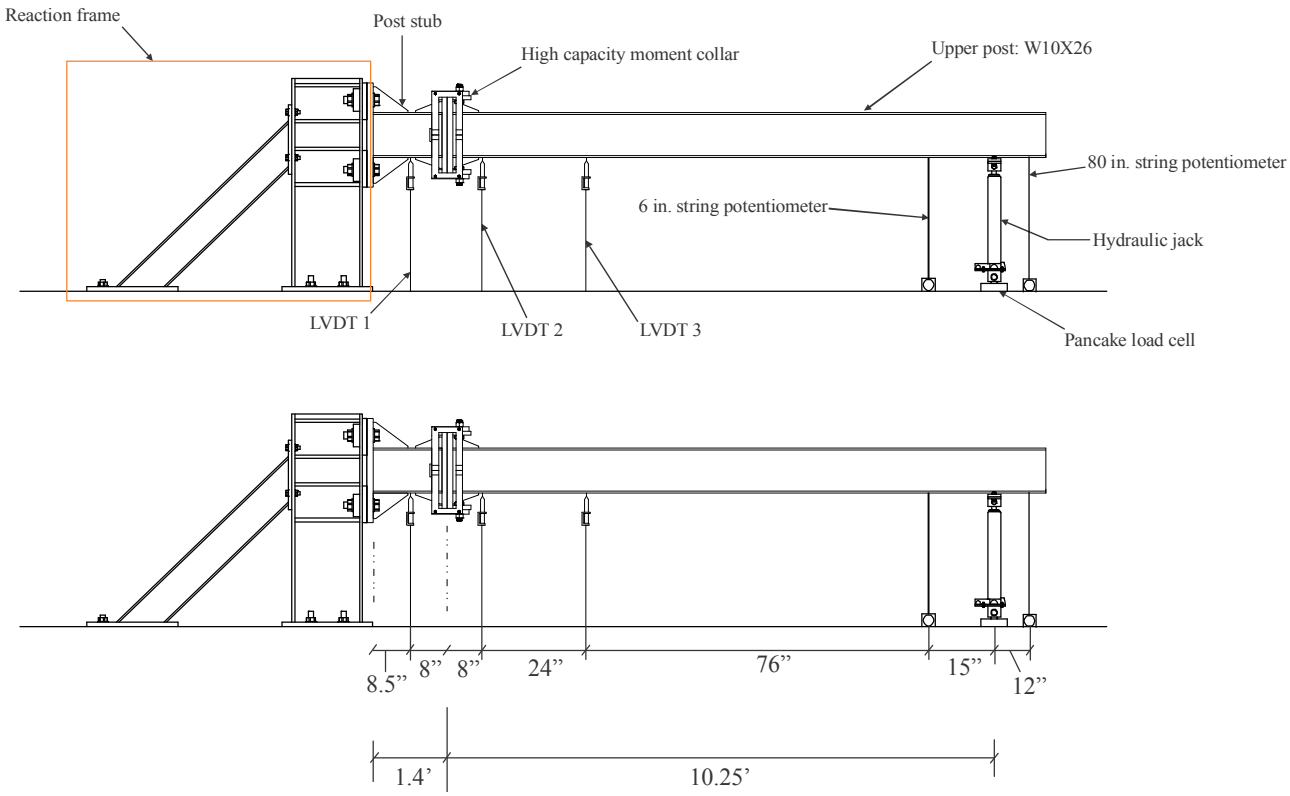

Figure 4.28 Schematic diagram of static test setup used to determine ultimate flexural capacity

To assemble the test articles, the stub and post were aligned and secured together with two halves of the high-capacity moment collar. An approximately-fixed support condition was created by horizontally attaching the stub to the reaction frame with four 1-1/2 in. diameter bolts. Moment collar components—specifically primary plates and binding plates—were positioned and installed flush to the flange plates. Securing bolts that connected the binding plates to the primary plates were installed using compression tools that applied a force of approximately 300 lbf to each upper binding plate, thus ensuring full contact of the flange plates. (Note that the compression tools used in this study [shown later in Figure 6.7c] were essentially custom-fabricated C-clamps constructed from steel plates and threaded bars. Any tool that produces an equivalent application of force to the upper binding plates would be deemed acceptable for moment collar installation.) Once full contact was achieved, the securing bolts were torqued to 250 lbf-ft.

A hydraulic jack (16 kip capacity), was used to apply load near the end of the test article, approximately 10 ft from the slipping plane (between the flange plates) of the breakaway connection. At this loading position, the load location was in agreement with specifications provided in AASHTO LTS-6, which state that load must be applied at a distance of at least five times the maximum major bending dimension of the post tested. Load applied by the hydraulic jack to the post was measured using a pancake load cell (50 kip capacity, manufactured by National Scale Technology), positioned under the jack with a pin joint and spherical washer-set (Figure 4.29). A 1-in. thick steel support plate, anchored to the lab floor, was used as the base for the load cell.

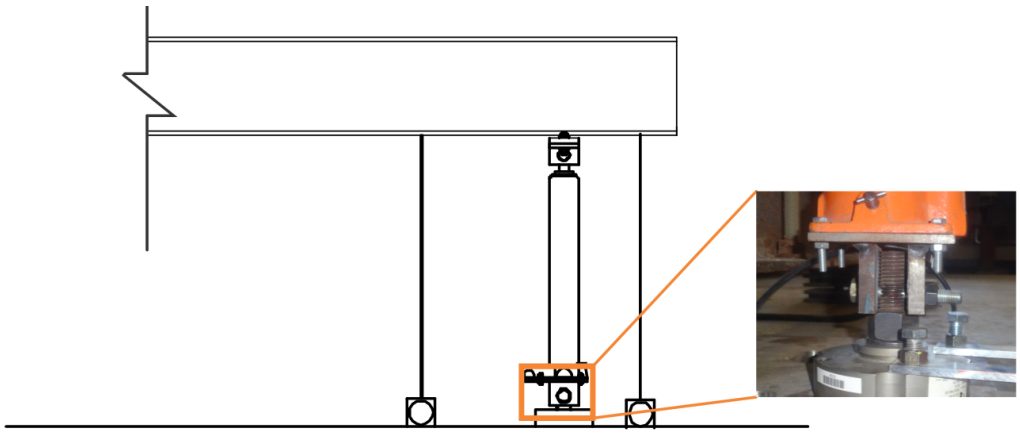

Figure 4.29 Hydraulic jack connected to load cell using a pin joint and spherical washers

Vertical steel guides were placed on both sides of the steel post, at the jack loading location, to keep the W10x26 post from deflecting laterally during testing. Use of the steel guides restrained the post from laterally-torsionally buckling, and ensured that loading was about the strong axis of the post. Vertical displacements were measured at several locations along the post using DCTH Series LVDTs (manufactured by RDP Electrosense). Load was applied through the jack such that a displacement rate (at the jack location) of approximately 1.5 in./min was produced. System response during testing was monitored by way of a load vs. tip-deflection plot. Loading was continued until the ultimate flexural capacity was reached.

4.4.1 Static flexural capacity, Test 1

On March 1, 2016, static flexural capacity Test 1 was conducted (Figure 4.30) on the first of two test articles. In Figure 4.31, photographs of deformation of the post, breakaway connection components, and the stub are shown at various stages during testing. Due to the shear load applied by the hydraulic jack, the flange plates in the connection—which were separated by a sheet of low-friction Teflon—slipped relative to one-another (Figure 4.31c). This relative motion, in turn, caused tension loading of the four (4) connector bolts, however, not to a force level sufficient to cause bolt rupture. As the jack force was increased further, the collar remained intact, and eventually a plastic hinge formed in the steel stub (Figure 4.31d) just above one of the LVDTs that were used to measure vertical displacement. Results from Test 1 are shown in Figure 4.32 in the form of a moment-rotation plot. System response was nearly linear up to the required flexural capacity of (FS=1.5)(80 kip-ft)=120 kip-ft, ultimately reaching 151 kip-ft (26% larger than required), and producing a FS=(151 kip-ft/80 kip-ft)=1.89>1.5. The experimental rotation data shown in Figure 4.32 account for contributions from (1) deformation of the breakaway connection components, (2) plastic hinge rotation in the stub, and, (3) slip at all Teflon-steel interfaces. As such, these data are comparable to corresponding rotations computed using finite element analysis (recall Figure 3.4b). In Figure 4.32, FEA moment-rotation data (reproduced from Figure 3.17) are shown to be in generally good agreement with the experimental results. Considering that the FEA simulation employed a material model with a yield point of exactly 50 ksi, whereas the yield point of the steel used in test article fabrication almost certainly exceeded this value, the observed differences in peak moment are reasonable.

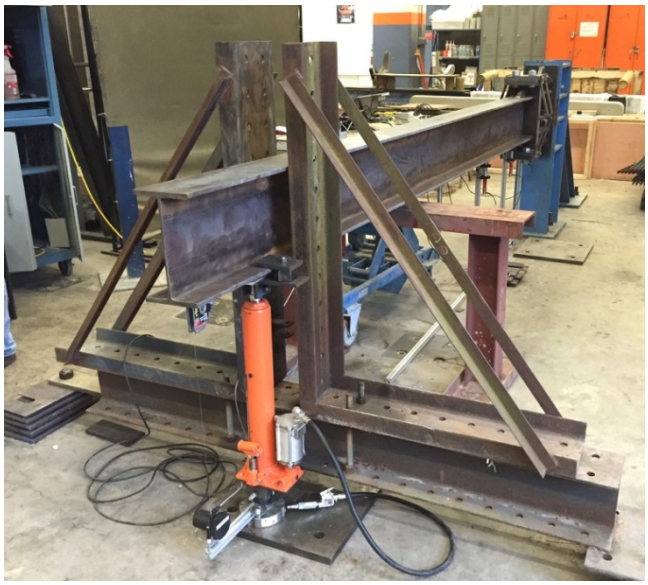

Figure 4.30 Overview of static flexural capacity Test 1

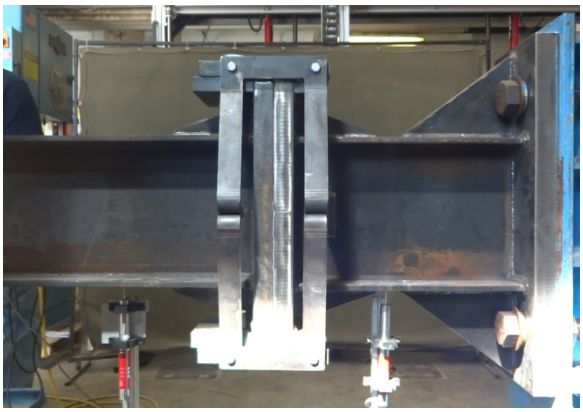

(a)

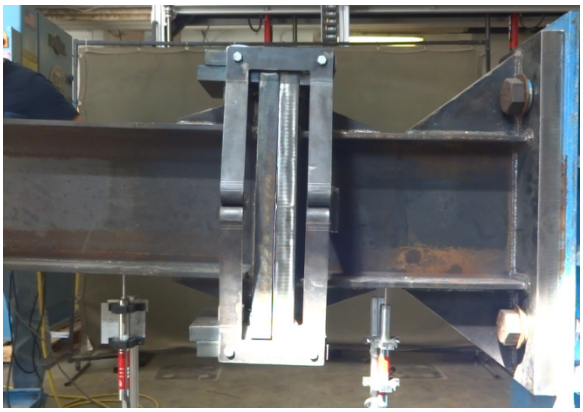

(b)

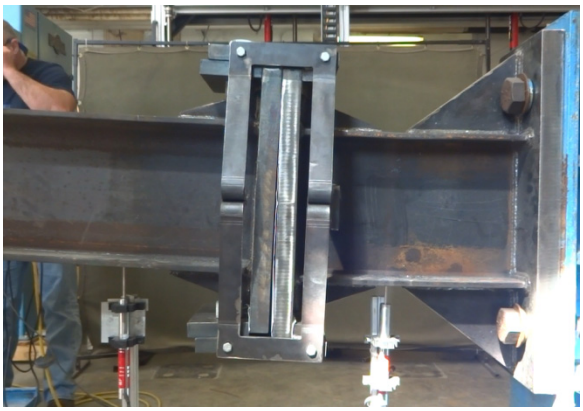

(c)

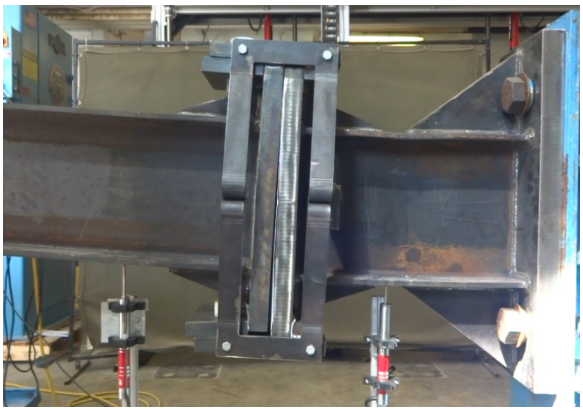

(d)

Figure 4.31 Deformations of post, breakaway connection, and stub during flexural Test 1

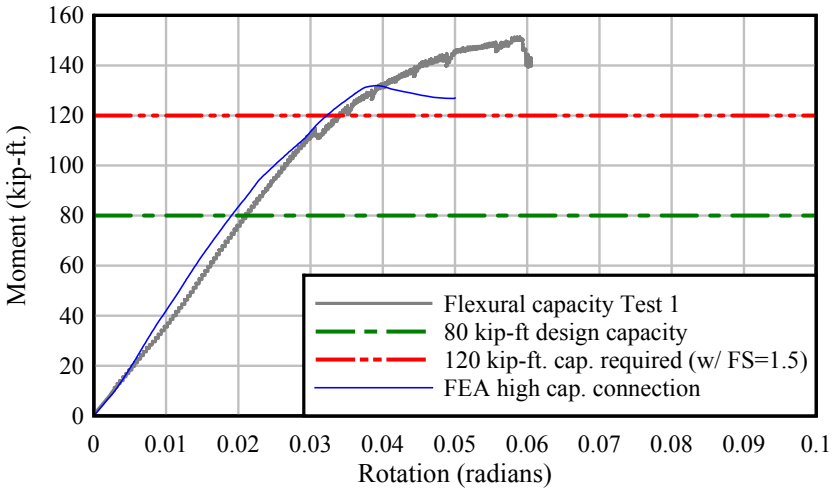

Figure 4.32 Results from flexural capacity Test 1

4.4.2 Static flexural capacity, Test 2

On March 17, 2016, static flexural capacity Test 2 was conducted (Figure 4.33 and Figure 4.34) on the second test article. In Figure 4.35, photographs of deformation of the post, breakaway connection components, and stub are shown at various stages during testing. During Test 2, as in Test 1, the flange plates in the connection slipped relative to one-another (Figure 4.35c). However, unlike Test 1, the degree of relative slip continued to increase during Test 2 (Figure 4.35d). The continued increase in slip was possibly due to fabrication differences, or due to insufficient tightening of the side bolts (Grade 8 cap screws) that connected the U-plates to the primary plates. Regardless, due to the magnitude of the slip displacement, significant eccentric loading of the lower primary plate occurred, causing visually evident bending of the bottom primary plate (Figure 4.35d). As the jack force was further increased, bending of the lower primary plate increased accordingly, as did tension forces in the four (4) connector bolts. Eventually all four (4) connector bolts failed, releasing the collar-halves (Figure 4.35e) and—due to the horizontal orientation of the test setup—allowing the post and stub to separate (Figure 4.35f).

At the ultimate strength condition, permanent bending deformation (plastic hinging) occurred in both the stub (Figure 4.36a) and the lower primary plate (Figure 4.36b). Results from Test 2 are presented in Figure 4.37, and compared to the corresponding results from Test 1. System response in Test 2 was again nearly linear up to the required flexural capacity of (FS=1.5)(80 kip-ft)=120 kip-ft, ultimately reaching 138 kip-ft (15% larger than required) and producing a FS=(138 kip-ft/80 ftip-ft)=1.72>1.5). The momentary drop in moment during Test 2 at approximately 130 kip-ft corresponded to the flange plates slipping as described above.

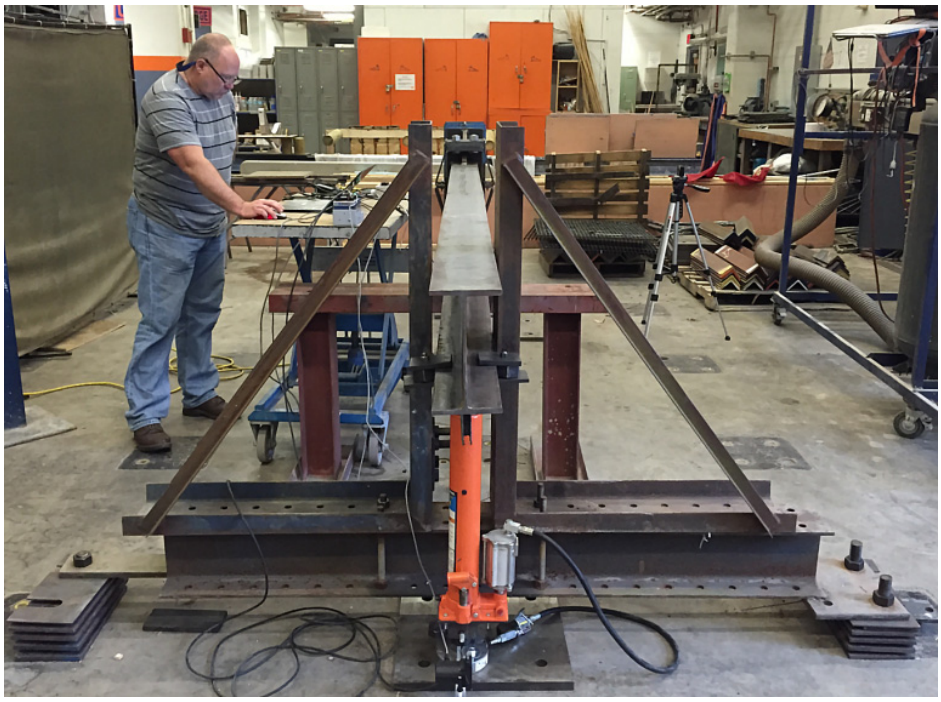

Figure 4.33 End view of static flexural capacity Test 2

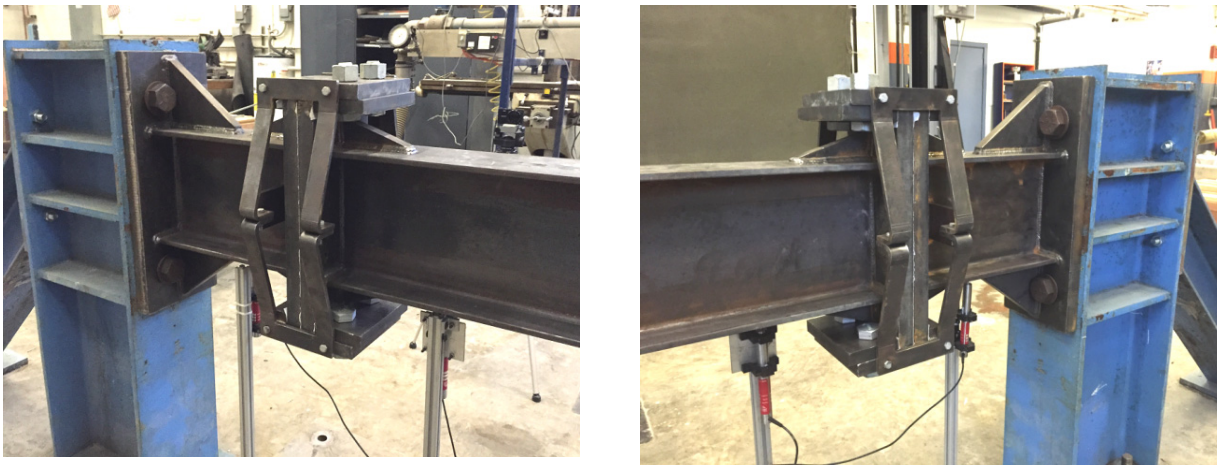

(a) (b)

Figure 4.34 Side views of breakaway connection in static flexural capacity Test 2:
(a) North side; (b) South side

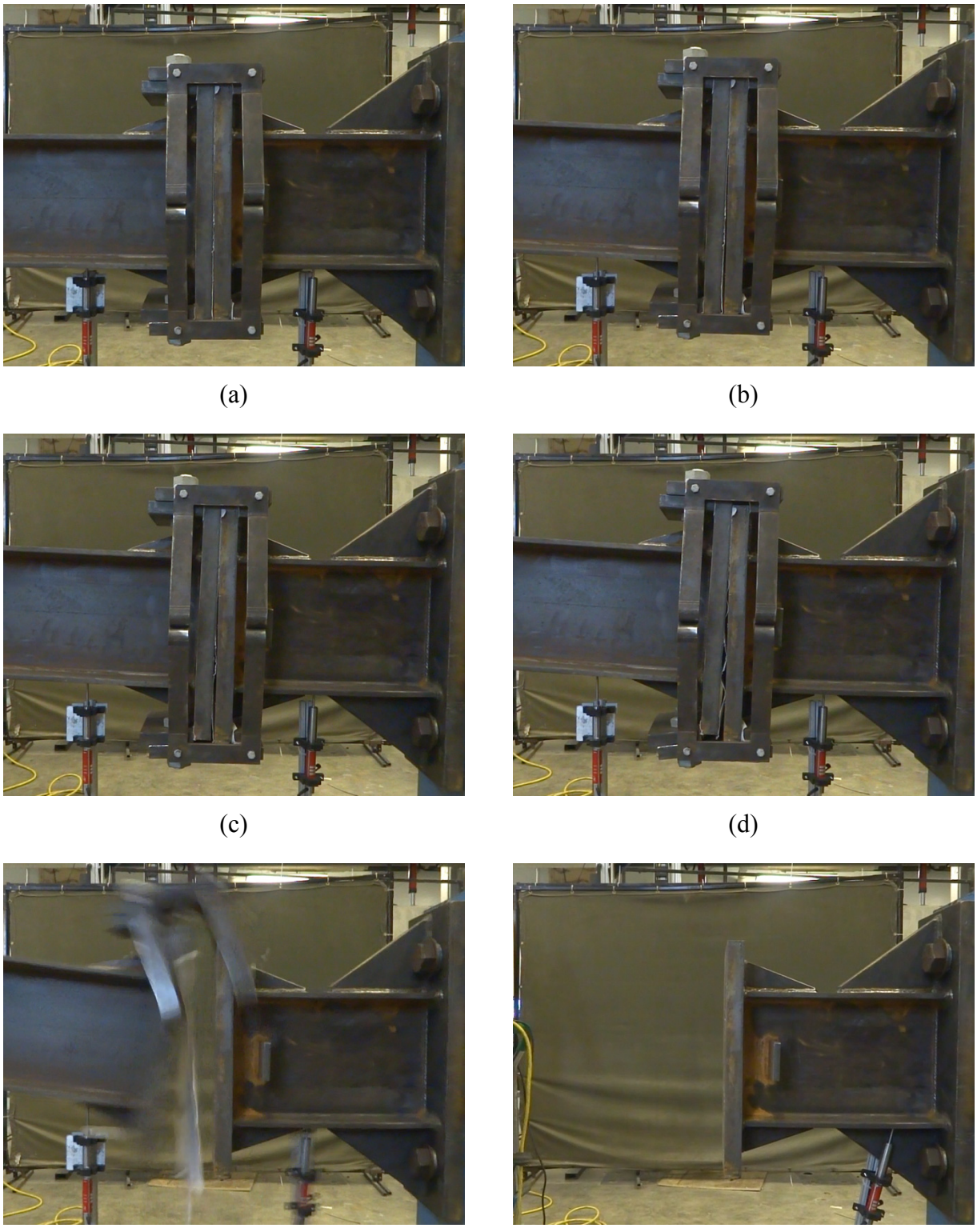

(a) (b) (c) (d) (e) (f)

Figure 4.35 Deformations of post, breakaway connection, and stub during flexural Test 2

(a) (b)

Figure 4.36 Final deformed state after Test 2:
(a) Stub; (b) Bottom primary plate (with top U-plate unbolted and removed for clarity)

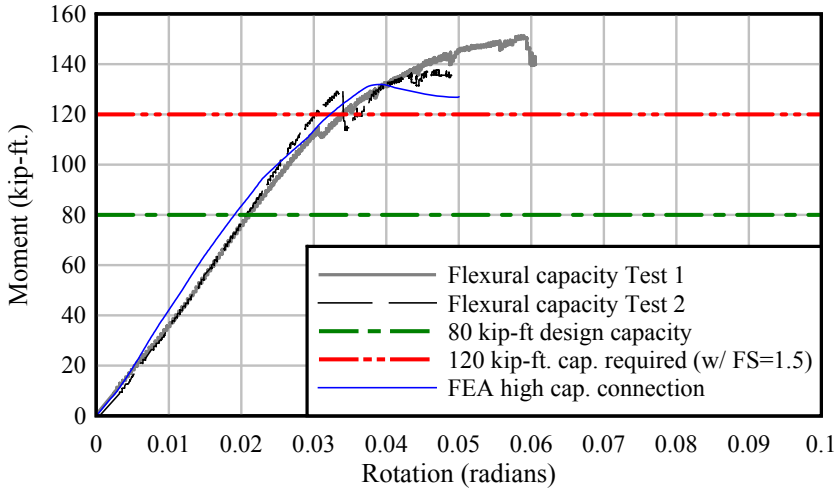

Figure 4.37 Results from flexural capacity Test 2 and Test 1 (for comparison)

CHAPTER 5
DEVELOPMENT OF MEDIUM-CAPACITY AND LOW-CAPACITY SYSTEMS

5.1 Introduction

For combinations of sign structure size and wind loading that require less flexural capacity than the high-capacity system defined in Table 2.3 (and described in previous chapters), 'scaled-down' medium- and low-capacity versions of the moment-resisting collar connection were developed. In the present chapter, the development of these systems, using dynamic and static finite element simulations, is described. Physical impact testing of the same systems is described in the following chapter.

5.2 Design approach

As described in earlier chapters, for the high-capacity system developed in this study, a representative post size of W10x26 was employed. Based on the flexural capacities and post-depth ranges stipulated in Table 2.3, post sizes selected for use in designing the medium-capacity and low-capacity connections were W8x24 (an 8-in.-deep post) and W5x19 (a 5-in.-deep post), respectively. Since these post sizes were lighter (i.e., less mass per unit length) than the W10x26 post used in the high-capacity system, the inertial resistances (during vehicle impact) of the medium- and low-capacity posts were known in advance to be less than that of the high-capacity post. Furthermore, all components (flange plates, primary plates, binding plates, U-plates, etc.) in the medium- and low-capacity connections were designed to be of equal or smaller size than the corresponding components in the high-capacity connection. Thus, the medium- and low-capacity breakaway connection assemblies were lighter (less massive) than the high-capacity breakaway connection assembly.

Given that both the post and breakaway connection assemblies were lighter in the medium- and low-capacity systems, occupant risk (OIV) values for these systems were expected to be lower than the OIV for the more massive, high-capacity system. Furthermore, since the OIV value for the high-capacity system was confirmed to be within the limits permitted by AASHTO MASH, the OIV values for the medium- and low-capacity connections were similarly expected to be within the allowable MASH limits.

Consequently, for purposes of designing the medium- and low-capacity connections, it was not deemed necessary to conduct finite element impact simulations from which OIV values would be quantified[†]. Instead, focus was given to conducting quasi-static pushover analyses of candidate medium- and low-capacity connection designs so that individual component thicknesses could be optimized while still satisfying the ultimate wind resistance (flexural strength) requirements of AASHTO LTS-6.

Design of the medium- and low-capacity breakaway connections was based primarily on the following principles:

- *Commonality of design concepts*: The basic function of each component in the high-capacity system was preserved but scaled-down to produce the medium- and low-capacity systems. Structural components were neither added, nor removed, during the scaling process.

[†] Note, however, that OIV values were later computed for the medium-capacity and low-capacity systems from physical impact test data, as documented in the next chapter.

- *Commonality of system components*: Wherever feasible and efficient (from a structural perspective), the same components, or component dimensions were used in the high-, medium-, and low-capacity systems. For example, the sizes of the tension connector bolts (used to join the collar halves) and the cap screws (used to secure the U-plates to the primary plates) were the same in the high-, medium-, and low-capacity systems, so that all such bolts are interchangeable (and thus cannot be accidentally confused in the field). Similarly, the thickness of the U-plates was maintained at a constant value (3/8 in. thickness) across all three system sizes (high, medium, low) for uniformity in fabrication processes.
- *Uniformity of flange widths*: All three system sizes (high, medium, low) utilize flange plates that are 8 in. in width.
- *Structural optimizations*: Key component dimensions (primary- and binding-plate thicknesses, securing-bolt diameters, etc.) were reduced in the medium- and low-capacity systems to a reasonable extent, i.e., to a level that did not require the use of hard-to-acquire materials (plate thicknesses, bolt types). Because A490 securing-bolts are not widely available in galvanized form, lower strength, galvanized A325 securing-bolts were used instead (in all systems: high, medium, low). The use of lower strength A325 bolts, however, necessitated primary- and binding-plates that were moderately thicker than would have been required with A490 bolts. In summary, reasonable structural optimization within the constraints of material availability was sought in designing the medium- and low-capacity systems.

Overview drawings of the finalized medium- and low-capacity systems are shown, in comparison to the high-capacity system, in Figure 5.1. Detailed fabrication drawings for the medium- and low-capacity systems are included in Appendix C and Appendix D of this report, respectively.

5.3 Confirmation of flexural capacity using quasi-static pushover analysis

To quantify ultimate flexural capacity under equivalent-static wind loading conditions, finite element models representing each 'candidate' (i.e., trial) design of the medium- and low-capacity connections, and attached segments of sign post, were subjected to quasi-static pushover analyses, using the procedures previously described in Chapter 3 and illustrated in Figure 3.4.

5.3.1 Medium-capacity connection

As indicated in Table 2.3, the design flexural strength (for wind loading) of the medium-capacity breakaway connection was defined as 55 kip-ft. For breakaway supports, AASHTO LTS-6 requires that the ultimate flexural strength of the device exceed the design strength multiplied by a factor of safety FS=1.5. Thus, the minimum required ultimate capacity of the medium-capacity connection was (FS=1.5)(55 kip-ft) = 82.5 kip-ft. Results from a quasi-static pushover analysis of this system (Figure 5.2) indicated that yielding first occurred at the junction between the tension-side triangular stiffener and the upper flange plate. With continued loading, the zone of yielding started to spread. However, ultimate capacity was eventually controlled by formation of a plastic hinge in the post, not by complete yielding of the triangular stiffener.

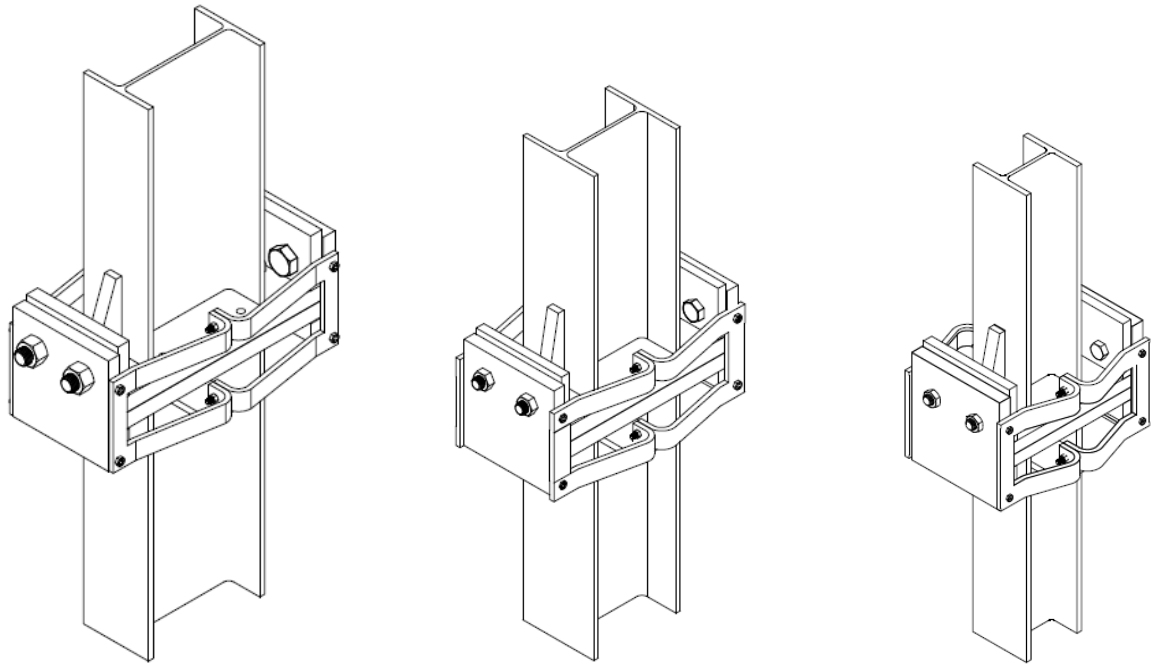

(a) (b) (c)

Figure 5.1 Breakaway connection systems:
(a) High-capacity connection with W10x26 post; (b) Medium-capacity connection with W8x24 post; (c) Low-capacity connection with W5x19 post

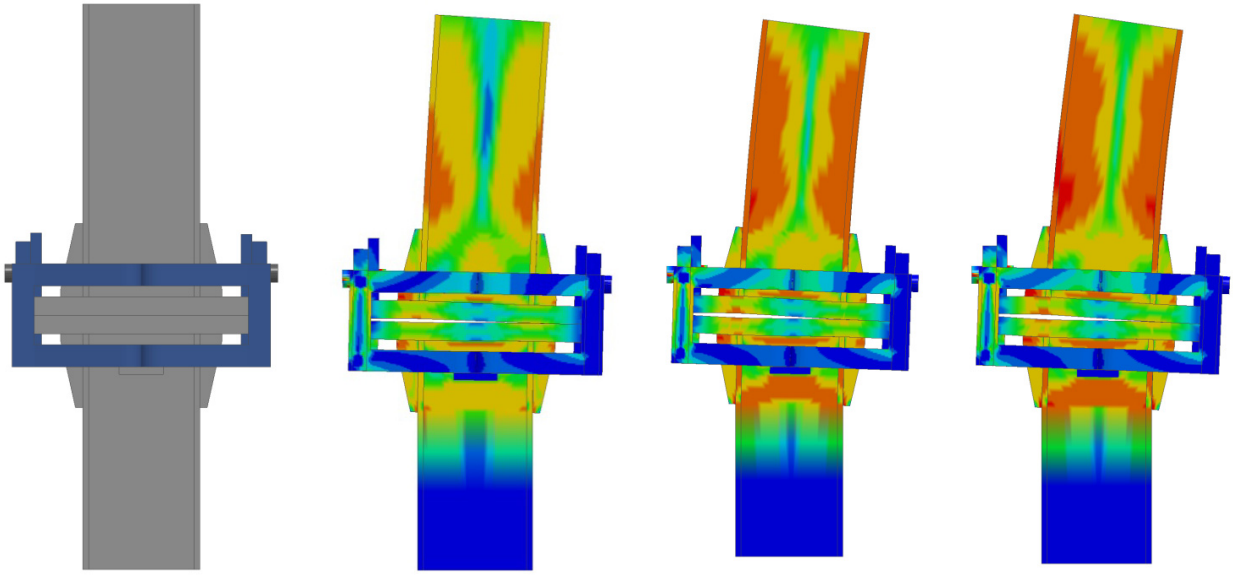

(a) (b) (c) (d)

Figure 5.2 Effective stresses from pushover analysis of medium-capacity connection with W8x24 post: (a) Unstressed model; (b) Initial yielding of stiffener tip; (c) Initial yielding of W8x24 post; (d) Maximum flexural capacity (Legend: blue = 0 ksi; red = 65 ksi = σ_{ULT})

In Figure 5.3, moment-rotation data—determined per Figure 3.4b—from the medium-capacity pushover analysis are compared to the design moment (55 kip-ft) and to the ultimate moment required by AASHTO LTS-6 (82.5 kip-ft). Per finite element pushover simulation, the medium-capacity connection possessed an ultimate flexural strength that exceeded the AASHTO required value by approximately 30%. Furthermore, as discussed in Section 3.3.4, the nonlinear constitutive relationship used in the finite element model employed a yield point of Fy=50 ksi. For A572 Gr. 50 steel, 50 ksi is the *minimum* yield strength. As actual yield strengths for A572 Gr. 50 steel will typically exceed the minimum specified value of 50 ksi, the buffer between the ultimate strength of the connection and the AASHTO required strength would likely exceed 30% in most practical cases.

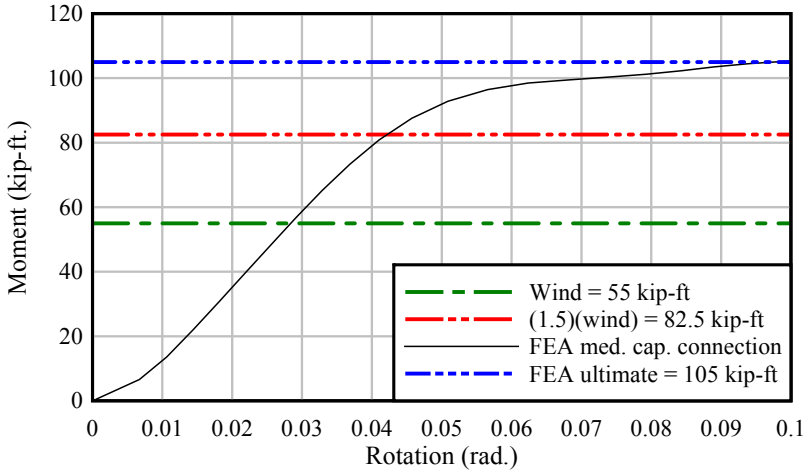

Figure 5.3 Results from quasi-static finite element pushover analysis of medium-capacity connection with W8x24 post

5.3.2 Low-capacity connection

For the low-capacity design moment of 30 kip-ft indicated in Table 2.3, AASHTO LTS-6 requires that the ultimate flexural capacity of the connection exceed (FS=1.5)(30 kip-ft)= 45 kip-ft. Results from a quasi-static pushover analysis of the low-capacity section (Figure 5.4) indicated that yielding first occurred in the post. With continued loading, yielding also initiated at the junction between the tension-side triangular stiffener and the upper flange plate. Ultimate capacity, however, was eventually controlled by formation of a plastic hinge in the post. In Figure 5.5, moment-rotation data from the pushover analysis are compared to the design moment (30 kip-ft) and to the ultimate moment required by AASHTO LTS-6 (45 kip-ft). Per finite element pushover simulation, the low-capacity connection possessed an ultimate flexural strength that exceeded the AASHTO required value by at least 20%.

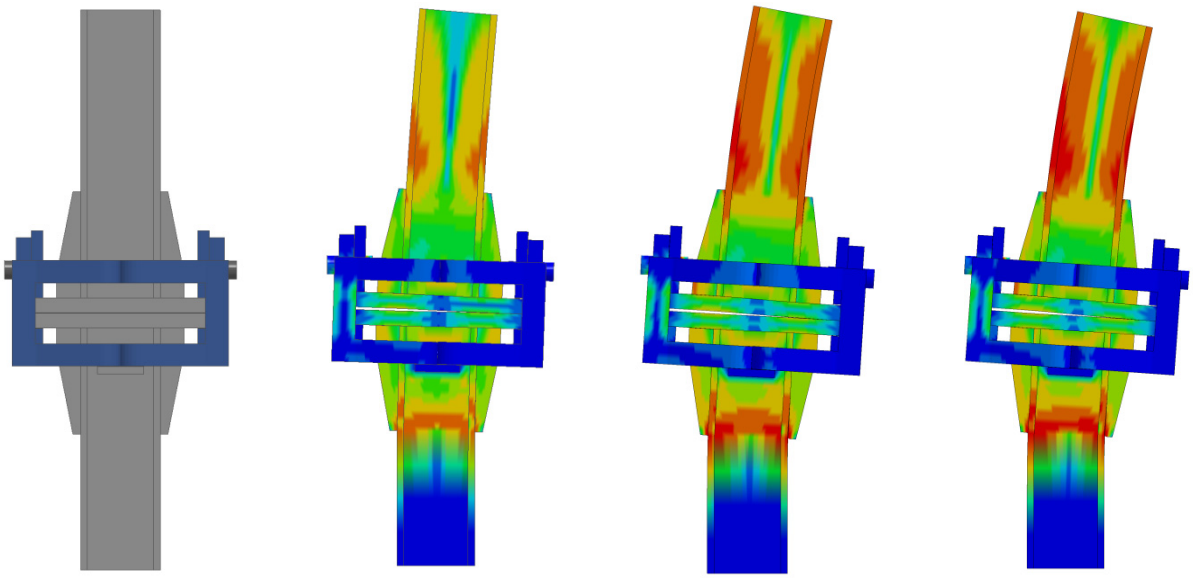

Figure 5.4 Effective stresses from pushover analysis of low-capacity connection with W5x19 post: (a) Unstressed model; (b) Initial yielding of W5x19 post; (c) Initial yielding of stiffener tip; (d) Maximum flexural capacity (Legend: blue = 0 ksi; red = 65 ksi = σ_{ULT})

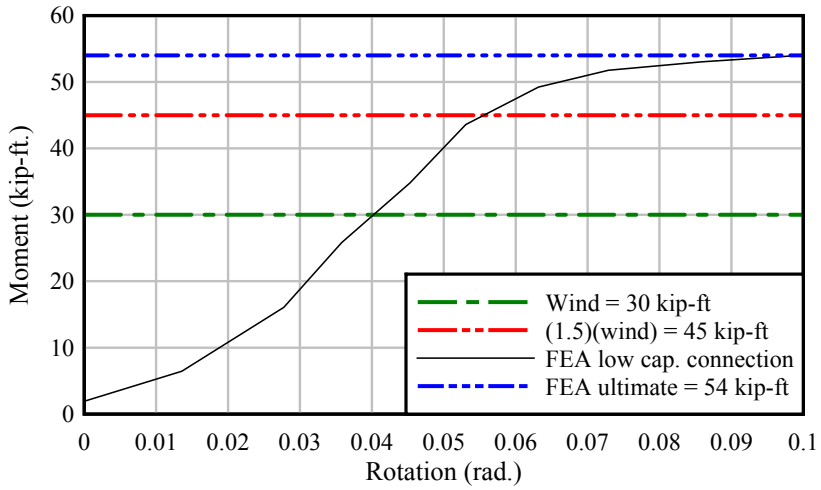

Figure 5.5 Results from quasi-static finite element pushover analysis of low-capacity connection with W5x19 post

CHAPTER 6
TESTING OF MEDIUM-CAPACITY AND LOW-CAPACITY SYSTEMS

6.1 Introduction

To experimentally evaluate the breakaway performance of the medium-capacity and low-capacity systems, experimental impact tests were conducted at the FDOT Structures Research Center using the gravity pendulum facility and the UF/FDOT 1100C crushable nose surrogate vehicle. Each impact test was conducted on a single-post breakaway system that consisted of either a W8x24 post (for the medium-capacity system, see Appendix C) or a W5x19 post (for the low-capacity system, see Appendix D). Each post was of the same height as that which would be installed in a full (i.e., multi-post) medium- or low-capacity sign system. To approximate the influence that sign panel mass—but *not* sign panel stiffness—would have in a multi-post sign structure, a steel channel was attached to the upper segment of each single-post test article. In each case, the channel mass was calibrated to be equal to the tributary mass of sign panel that would be associated with an interior post in a 3-post sign structure. All medium- and low-capacity test articles were fabricated by Precision Tool and Engineering in Gainesville, Florida.

As noted earlier, and as documented in Appendices C and D, 0.02-in. thick Teflon sheets were installed at five (5) locations within each medium-capacity and low-capacity breakaway connection system that was tested during this study.

6.2 Instrumentation

High-speed data acquisition systems were used to record data from high-speed video cameras, and from a collection of sensors. Specific items of instrumentation that were employed during each test included:

- Uniaxial accelerometers (50 g, quantity =2) on the back block of the surrogate vehicle
- Uniaxial accelerometer (250 g, quantity =1) on the impact head of the surrogate vehicle
- High speed video cameras (zoomed view, and wide angle view, quantity = 2)
- Emitter/receiver pairs of infrared optical break beam sensors (quantity = 2)
- A tape switch affixed to the impact face of the test article (steel post)

Both of the high speed video cameras recorded data at a rate of 2000 frames/sec. All remaining sensors (accelerometers, etc.) were sampled and recorded at a frequency of 10 kHz.

6.3 Impact testing

To be consistent with the requirements of AASHTO MASH, impact tests were conducted using the UF/FDOT 1100C crushable nose surrogate vehicle (Consolazio et al., 2016; Groetaers et al., 2016), an impact speed of 19 mph (produced by using a drop height of 12 ft), and impact angles of 0 deg. and 25 deg.

6.3.1 Medium-capacity connection: head-on (0 deg.) impact test

On June 17, 2016, an integrated test article—consisting of a stub, medium-capacity breakaway collar connection, post, and channel—was installed (Figure 6.1) and subjected to a head-on 19 mph impact from the UF/FDOT 1100C surrogate vehicle (Figure 6.2). As described

earlier (in Sections 4.2.2 and 4.2.3), both head-on (0 deg.) and oblique (25 deg.) impact testing of *high-capacity* single-post test articles demonstrated that insufficient upper-post resistance was available to break the fuse plates that were located at post mid-height. Accordingly, in each test, the entire post (lower and upper segments) rotated as a single entity (recall, for example, Figure 4.7). Results of this type arose due to the necessary omission of sign panel stiffness and adjacent-post stiffness from the pendulum test setup. Given that similar behavior was expected to occur during the medium-capacity (and also low-capacity) pendulum impact tests, full-height continuous sign posts—without fuse plates or hinge plates—were instead employed in these tests. (Note that steel channels representing the tributary mass of sign panel were still attached to each full-height continuous sign post, even though fuse/hinge plates were omitted.)

Due to fabrication errors, holes drilled in the U-plates that formed the sides of the moment collar connection were larger in diameter than specified (Figure 6.1a). Consequently, 3/8-in. thick, 5/8-in. O.D. (outer diameter) unthreaded steel spacers (McMaster-Carr part #93320A210) were inserted into the oversized holes in the U-plates, and oversized flat washers (as well as lock washers) were installed between the Grade 8 cap screws and the U-plates (Figure 6.1b).

In accordance with the dimensions of the Kia Rio production vehicle from which the UF/FDOT surrogate vehicle was developed, the impact elevation (mid-height of the impact head) on the lower-post was 18 in. above the theoretical ground plane (i.e., 14 in. above the slip plane in the breakaway connection, leaving a 4-in. permanent stub, as permitted by AASHTO MASH).

In Figure 6.3, frames from high speed video of the head-on impact test confirm that the two halves of the moment collar broke apart cleanly—as intended—after the tension bolts holding them together reached their rupture loads. On the upstream (impact) side, one collar-half remained with the stub and dropped to the ground. On the downstream (non-impact) side, the other collar-half cleared the stub without snagging and traveled with the lower-post. In Figure 6.4, frames from wide angle high speed video again show clean separation of the post from the stub.

(a)

(b)

(c)

Figure 6.1 Medium-capacity test article installed for head-on (0 deg.) impact test: (a) Elevation view of stub base, moment collar connection, and lower-segment post; (b) Isometric view of breakaway connection; (c) Integrated test article

(a)

(b)

(c)

Figure 6.2 Head-on (0 deg.) impact test of medium-capacity connection:
(a) 1100C surrogate vehicle and test article; (b) Elevation view; (c) Overview

Acceleration data from two 50g accelerometers mounted on the 1100C surrogate vehicle back block were averaged together and time-integrated (using trapezoidal integration) to compute the occupant impact velocity (OIV), which was found to be 7.9 ft/sec (Figure 6.5). For comparison, AASHTO MASH specifies a preferred OIV limit of 10 ft/sec and a maximum permissible limit of 16 ft/sec. AASHTO MASH also limits the maximum occupant ridedown acceleration (ORA) to 20.49 g, but sets the preferred limit at 15 g. Examining the acceleration data in Figure 6.6 after the time of occupant impact, the maximum occupant acceleration levels are found to be negligible in comparison to the AASHTO preferred ORA limit of 15 g. Hence the experimental OIV and ORA were both well within the permissible limits established by AASHTO MASH.

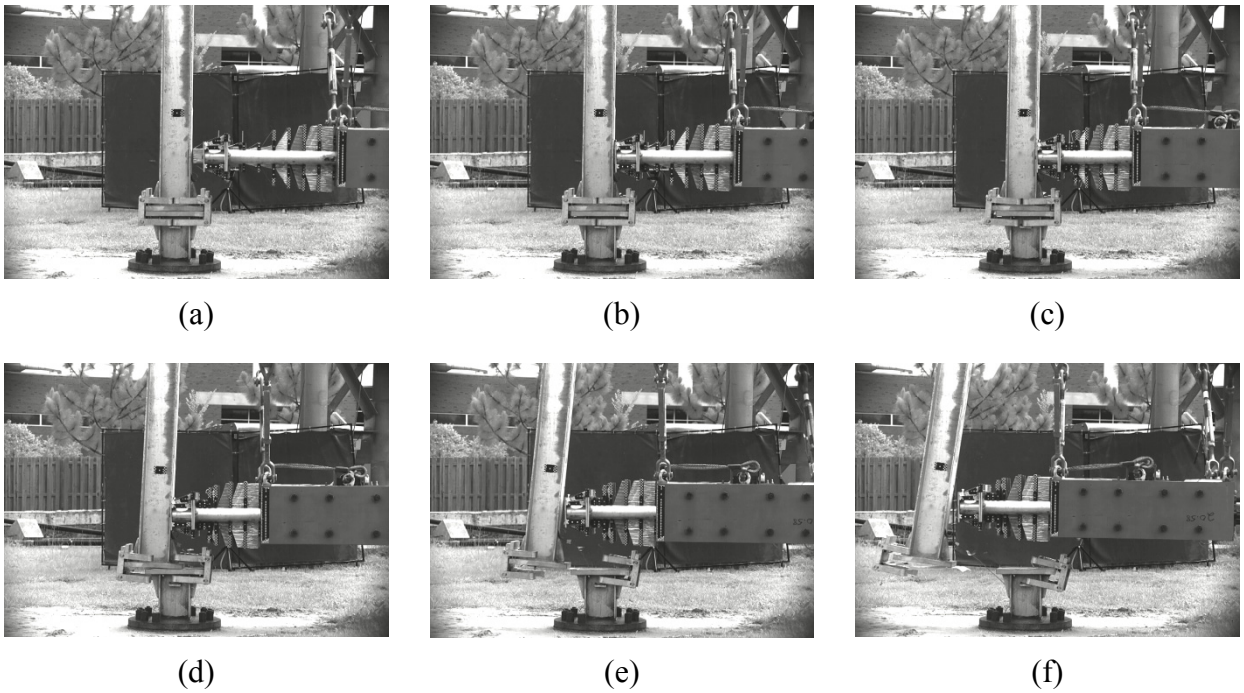

(a) (b) (c)

(d) (e) (f)

Figure 6.3 High speed video frames from head-on (0 deg.)
19-mph impact test of medium-capacity system

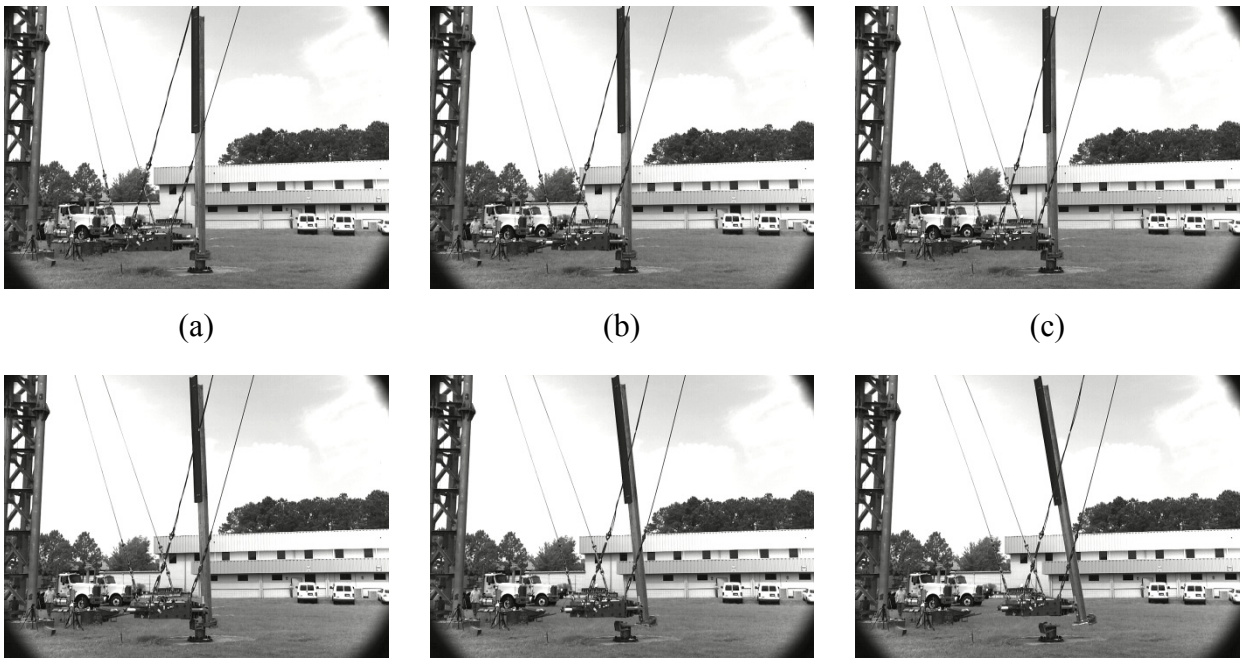

(a) (b) (c)

(d) (e) (f)

Figure 6.4 Wide angle high speed video frames from head-on (0 deg.)
19-mph impact test of medium-capacity system

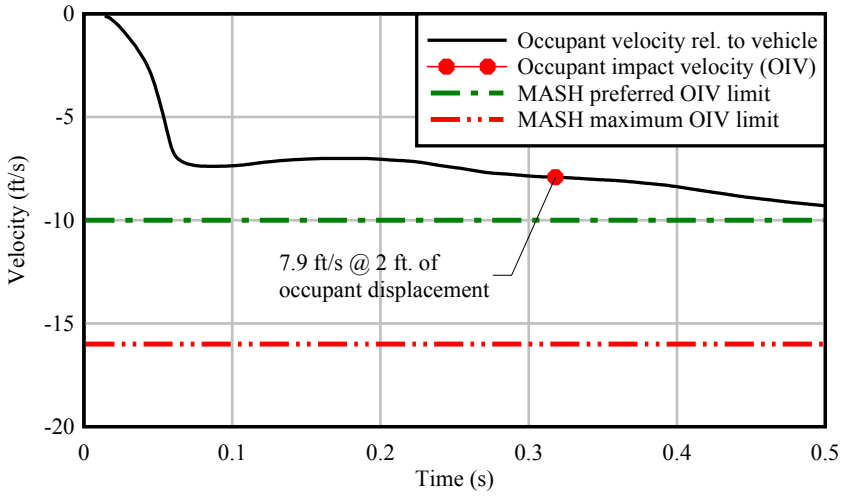

Figure 6.5 Occupant impact velocity (OIV) from head-on (0 deg.) 19-mph impact test of medium-capacity system

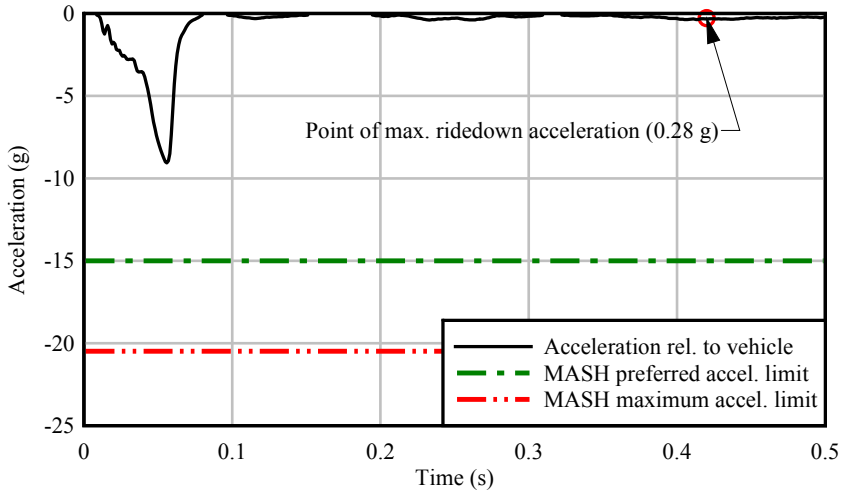

Figure 6.6 Occupant ridedown acceleration (ORA) from head-on (0 deg.) 19-mph impact test of medium-capacity system

6.3.2 Medium-capacity connection: oblique (25 deg.) impact test

On June 22, 2016, an oblique angle (25 deg.) impact test was performed on a medium-capacity connection test article to assess the potential for breakaway component snagging and abrupt vehicle deceleration. Due to the fabrication errors noted earlier, holes drilled in the U-plates that formed the sides of the moment collar connection were larger in diameter than specified in the fabrication drawings. Thus, as in the head-on (0 deg.) test, 3/8-in. thick, 5/8-in. O.D. (outer diameter) unthreaded steel spacers were inserted into the oversized holes in the U-plates, and oversized flat washers (and lock washers) were installed between the Grade 8 cap screws and the U-plates. However, for the oblique (25 deg.) impact test, extension plates (Figure 6.7a) also had to be welded into the U-plates to re-introduce *confinement* of the flange plates that was lost as a result of the fabrication errors. Had the U-plates been fabricated correctly, they would have confined the flange plates as intended, thereby preventing transverse

sliding of the flange plates relative to one another during oblique impact. The addition of the extension plates only reintroduced the intended extent (i.e., dimension) of confinement; their addition did not, however, add more confinement than was originally intended.

Remaining steps in the collar installation process are illustrated in Figure 6.7b-d. Once fully installed, the integrated test article—consisting of a stub, medium-capacity breakaway collar connection, full-height continuous post (without fuse/hinge plates), and channel—was subjected to an oblique (25 deg.) 19-mph impact from the UF/FDOT 1100C surrogate vehicle (Figure 6.8).

(a)

(b)

(c)

(d)

Figure 6.7 Installation of medium-capacity connection for oblique (25 deg.) impact test: (a) U-plates with added extensions due to fabrication errors; (b) Parts ready for assembly; (c) Compression tools applied to upper binding plates; (d) Fully assembled system

(a)

(b)

(c)

Figure 6.8 Oblique (25 deg.) impact test of medium-capacity connection:
(a) Fully-installed test article; (b) Side view of oblique impact angle;
(c) Overhead view of oblique impact angle

In Figure 6.9, frames from high speed video of the oblique impact test confirm that no significant snagging occurred. After the two halves of the moment collar broke apart, the downstream (non-impact) collar-half momentarily interacted with (i.e., contacted) the downstream vertical flange of the stub. However, this contact was brief in duration, and did not prevent the collar-half from continuing to travel with the lower-post segment, eventually clearing the stub. In Figure 6.10, frames from wide angle high speed video again show clean separation of the post from the stub. The brief contact interaction between the downstream collar-half and the stub flange resulted in slightly non-uniform (unsymmetric) permanent deformations of the U-plate legs (Figure 6.11), but no further damage was observed.

Acceleration data from two 50 g accelerometers mounted on the 1100C surrogate vehicle back block were averaged together and time-integrated (using trapezoidal integration) to compute the occupant impact velocity (OIV), which was found to be 7.3 ft/sec (Figure 6.12). For comparison, AASHTO MASH specifies a preferred OIV limit of 10 ft/sec and a maximum permissible limit of 16 ft/sec. AASHTO MASH also limits the maximum occupant ridedown acceleration (ORA) to 20.49 g, but sets the preferred limit at 15 g. Examining the acceleration data in Figure 6.13 after the time of occupant impact, the maximum occupant acceleration levels are found to be negligible in comparison to the AASHTO preferred ORA limit of 15 g.

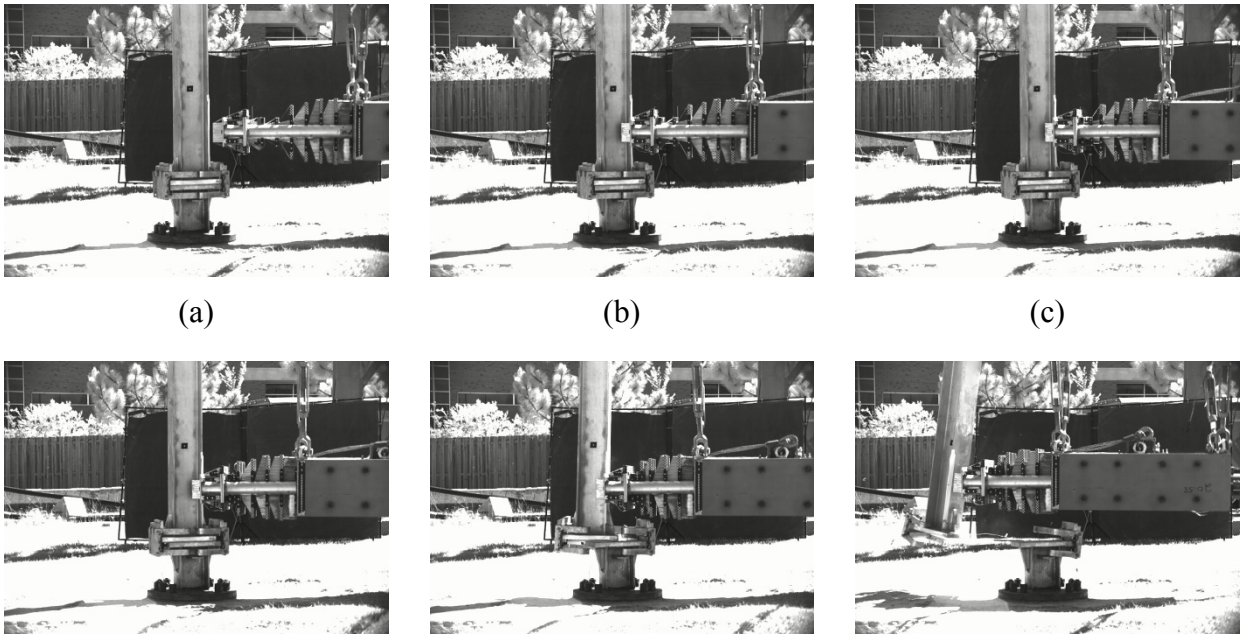

(a) (b) (c)

(d) (e) (f)

Figure 6.9 High speed video frames from oblique (25 deg.)
19-mph impact test of medium-capacity system

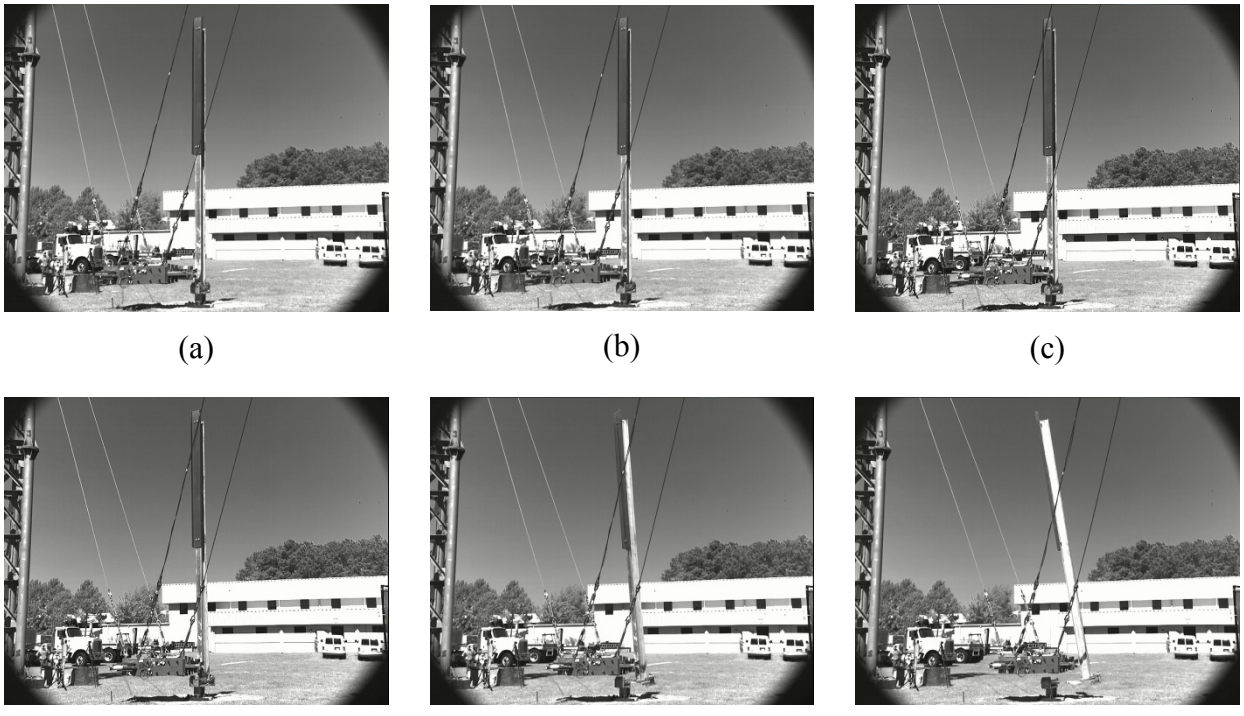

(a) (b) (c)

(d) (e) (f)

Figure 6.10 Wide angle high speed video frames from oblique (25 deg.)
19-mph impact test of medium-capacity system

Figure 6.11 Medium-capacity collar components after oblique (25 deg.) 19-mph impact test

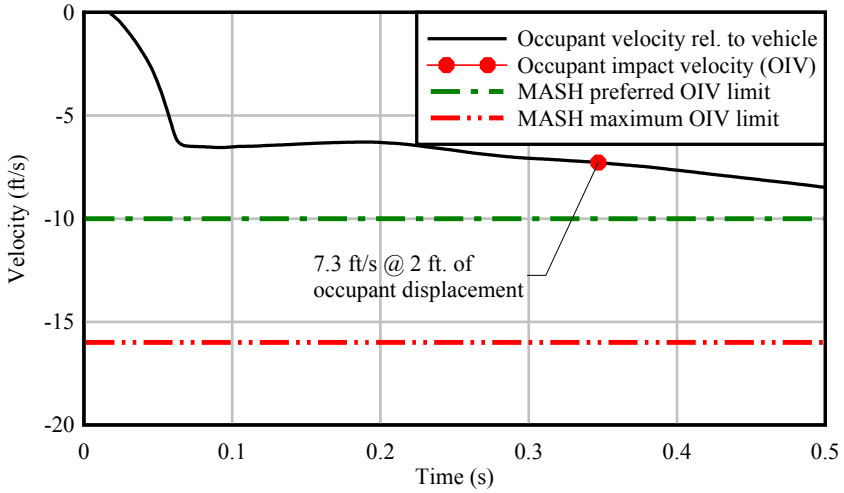

Figure 6.12 Occupant impact velocity (OIV) from oblique (25 deg.) 19-mph impact test of medium-capacity system

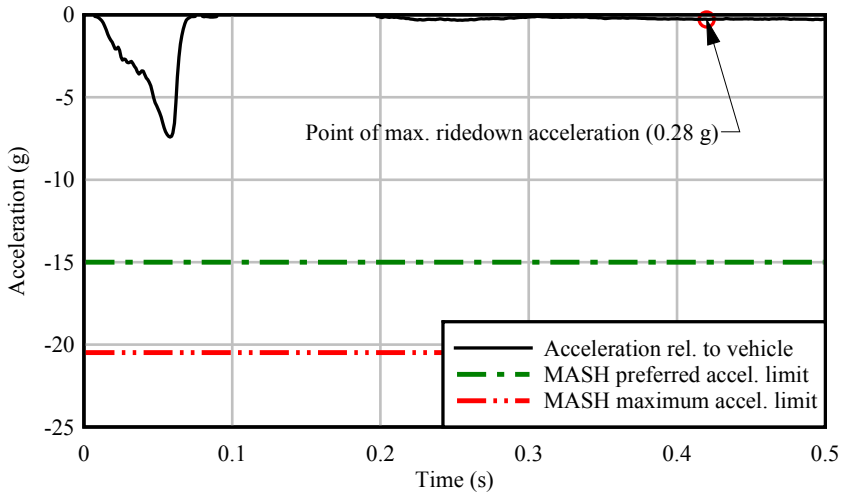

Figure 6.13 Occupant ridedown acceleration (ORA) from oblique (25 deg.) 19-mph impact test of medium-capacity system

6.3.3 Low-capacity connection: head-on (0 deg.) impact test

On June 22, 2016, an integrated test article—consisting of a stub, low-capacity breakaway collar connection, full-height continuous post (without fuse/hinge plates), and channel—was installed (Figure 6.14) and subjected to a head-on 19 mph impact from the UF/FDOT 1100C surrogate vehicle (Figure 6.15). Due to the same type of fabrication errors noted earlier, holes drilled in the U-plates that formed the sides of the moment collar connection were larger in diameter than specified. Consequently, 3/8-in. thick, 5/8-in. O.D. (outer diameter) unthreaded steel spacers were inserted into the oversized holes in the U-plates, and oversized flat washers (as well as lock washers) were installed between the Grade 8 cap screws and the U-plates.

In Figure 6.16, frames from high speed video of the head-on impact test confirm that the two halves of the moment collar broke apart cleanly—as intended—after the tension bolts holding them together reached their failure loads. On the upstream (impact) side, one collar-half remained with the stub and dropped to the ground. On the downstream (non-impact) side, the other collar-half cleared the stub without snagging and traveled with the lower-post. In Figure 6.17, frames from wide angle high speed video again show clean separation of the post from the stub.

Acceleration data from two 50 g accelerometers mounted on the 1100C surrogate vehicle back block were averaged together and time-integrated (using trapezoidal integration) to compute the occupant impact velocity (OIV), which was found to be 8.4 ft/sec (Figure 6.18). For comparison, AASHTO MASH specifies a preferred OIV limit of 10 ft/sec and a maximum permissible limit of 16 ft/sec. Although the low-capacity system was lighter than the medium-capacity system, the OIV for the low-capacity system (8.4 ft/sec, Figure 6.18) was 6% larger than the OIV for the medium-capacity system (7.9 ft/sec, Figure 6.5). During impact tests conducted on both systems (low- and medium-capacity), the vertical elevation-offset between the slip plane and the impact point was 14 in. In the low-capacity system, the connection flange plates were only 11.5 in. in length (see Appendix D), whereas in the medium-capacity system, the flange plates were 15 in. in length (see Appendix C). Given the smaller flange plate length of the low-capacity system, connection moment generated by the vehicle impact force—which acted at a fixed vertical eccentricity of 14 in.—caused larger flange-plate compressive contact forces to occur in the low-capacity system than occurred in the medium-capacity system. Accordingly, larger frictional forces were developed at the slip plane thus yielding a moderately larger OIV in the low-capacity system test. High speed video from the tests visually corroborated this explanation in that greater rotation of the sign-post base (indicating greater contact pressure) was observed in the low-capacity system test than in the medium-capacity system test.

AASHTO MASH also limits the maximum occupant ridedown acceleration (ORA) to 20.49 g, but sets the preferred limit at 15 g. Examining the acceleration data in Figure 6.19 after the time of occupant impact, the maximum occupant acceleration levels are found to be negligible in comparison to the AASHTO preferred ORA limit of 15 g.

(a)

(b)

(c)

(d)

Figure 6.14 Low-capacity test article installed for head-on (0 deg.) impact test:
(a) Assembly in progress with fit-up bolts in place; (b) Fully-installed connection (south side);
(c) Fully-installed connection (north side); (d) Fully-installed connection (elevation view)

(a)

(b)

(c)

Figure 6.15 Head-on (0 deg.) impact test of low-capacity connection:
(a) 1100C surrogate vehicle and test article; (b) Elevation view; (c) Overview

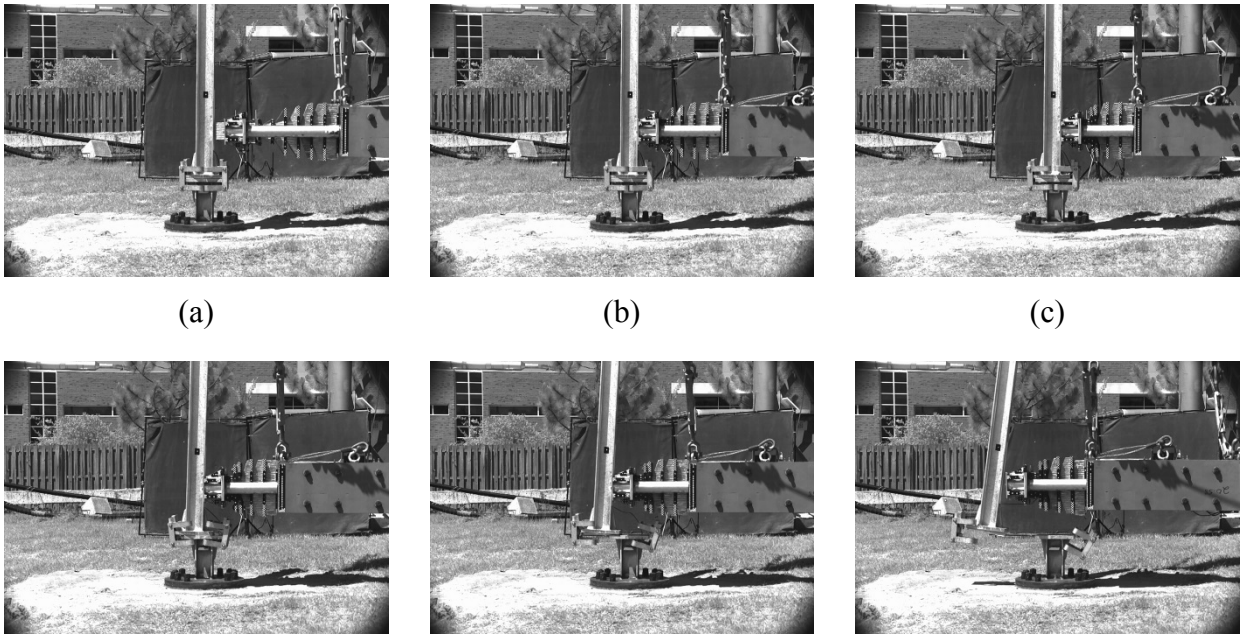

(a) (b) (c)

(d) (e) (f)

Figure 6.16 High speed video frames from head-on (0 deg.)
19-mph impact test of low-capacity system

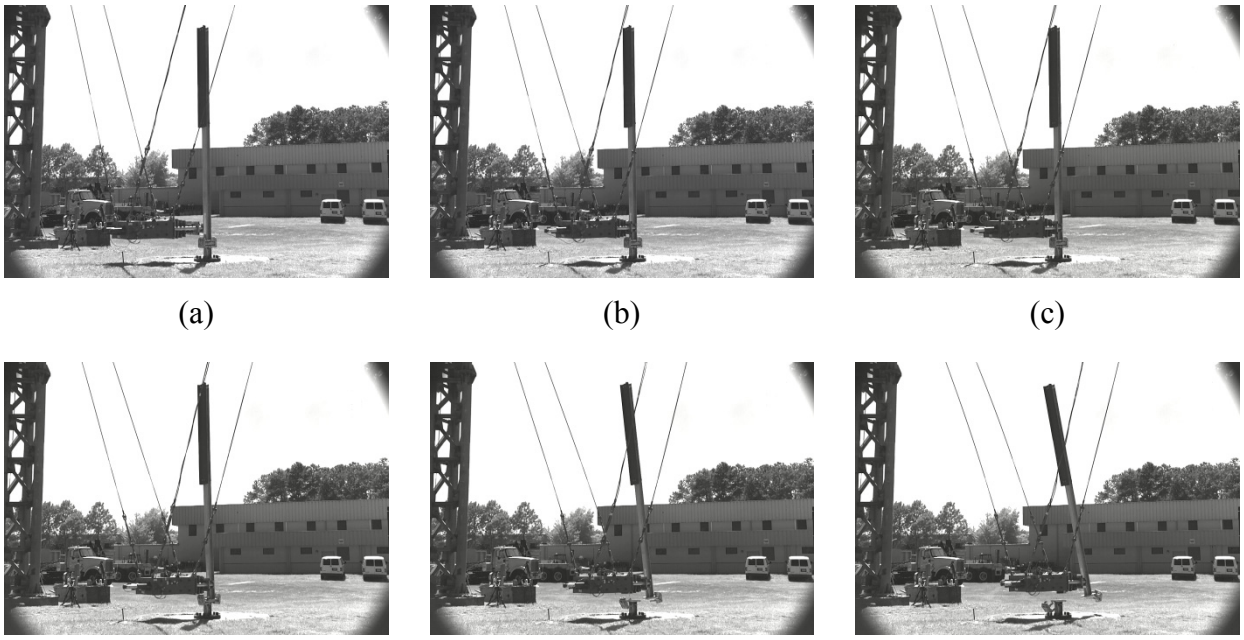

(a) (b) (c)

(d) (e) (f)

Figure 6.17 Wide angle high speed video frames from head-on (0 deg.)
19-mph impact test of low-capacity system

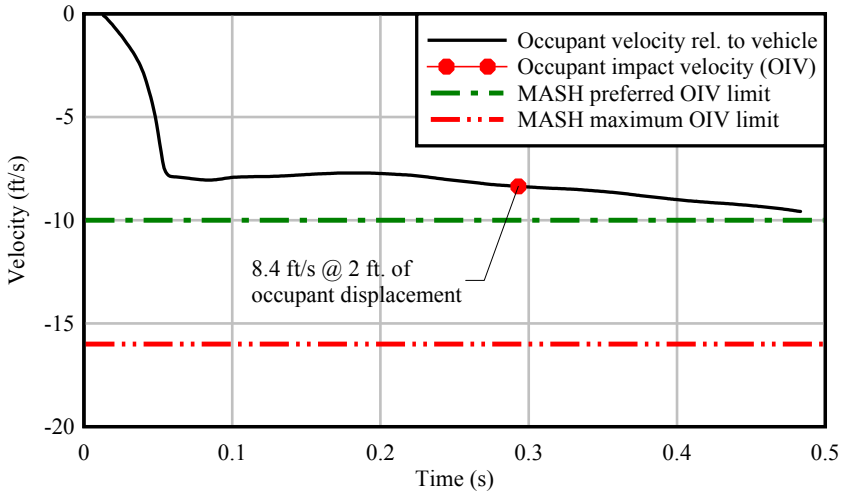

Figure 6.18 Occupant impact velocity (OIV) from head-on (0 deg.) 19-mph impact test of low-capacity system

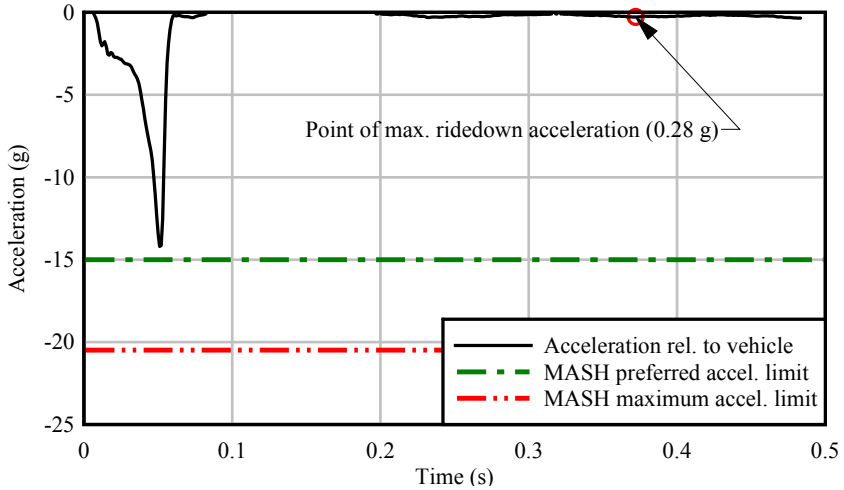

Figure 6.19 Occupant ridedown acceleration (ORA) from head-on (0 deg.) 19-mph impact test of low-capacity system

6.3.4 Low-capacity connection: oblique (25 deg.) impact test

On June 23, 2016, an oblique angle (25 deg.) impact test was performed on a low-capacity connection test article to assess the potential for breakaway component snagging and abrupt vehicle deceleration. Due to the fabrication errors noted earlier, holes drilled in the U-plates that formed the sides of the moment collar connection were larger in diameter than specified on the fabrication drawings. Thus, as in the head-on (0 deg.) test, 3/8-in. thick, 5/8-in. O.D. (outer diameter) unthreaded steel spacers were inserted into the oversized holes in the U-plates, and oversized flat washers (and lock washers) were installed between the Grade 8 cap screws and the U-plates. Once fully installed, the integrated test article—consisting of a stub, low-capacity breakaway collar connection, full-height continuous post (without fuse/hinge plates), and channel—was subjected to an oblique (25 deg.) 19-mph impact from the UF/FDOT 1100C surrogate vehicle (Figure 6.20).

(a)

(b)

(c)

Figure 6.20 Oblique (25 deg.) impact test of low-capacity connection:
(a) 1100C surrogate vehicle and test article; (b) Oblique alignment between impact head of surrogate vehicle and test article; (c) Overview of test setup

In Figure 6.21, frames from high speed video of the oblique impact test confirm that no significant snagging occurred. After the two halves of the moment collar broke apart, the downstream (non-impact) collar-half momentarily interacted with (contacted) the downstream vertical flange of the stub. However, this contact was brief in duration, and did not prevent the collar-half from continuing to travel with the lower-post segment, eventually clearing the stub. In Figure 6.22, frames from wide angle high speed video again show clean separation of the post from the stub.

Acceleration data from two 50g accelerometers mounted on the 1100C surrogate vehicle back block were averaged together and time-integrated (using trapezoidal integration) to compute the occupant impact velocity (OIV), which was found to be 8.2 ft/sec (Figure 6.23). For comparison, AASHTO MASH specifies a preferred OIV limit of 10 ft/sec and a maximum permissible limit of 16 ft/sec. Although the low-capacity system was lighter than the medium-capacity system, the OIV from the low-capacity oblique test (8.2 ft/sec, Figure 6.23) was 12% larger than the OIV from the medium-capacity oblique test (7.3 ft/sec, Figure 6.12). As described above, the smaller flange length used in the low-capacity system resulted in somewhat larger frictional forces during impact, thus moderately increasing the OIV.

AASHTO MASH also limits the maximum occupant ridedown acceleration (ORA) to 20.49 g, but sets the preferred limit at 15 g. Examining the acceleration data in Figure 6.24 after the time of occupant impact, the maximum occupant acceleration levels are found to be negligible in comparison to the AASHTO preferred ORA limit of 15 g. Hence the experimental OIV and ORA were both well within the permissible limits established by AASHTO MASH.

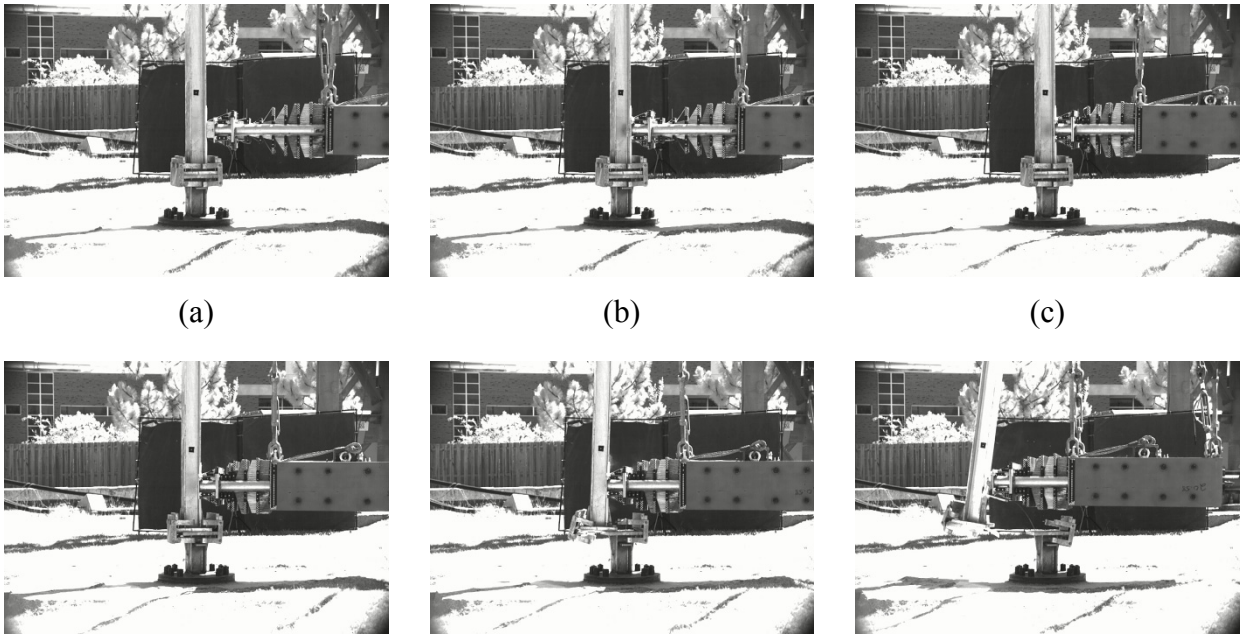

(a) (b) (c)

(d) (e) (f)

Figure 6.21 High speed video frames from oblique (25 deg.)
19-mph impact test of low-capacity system

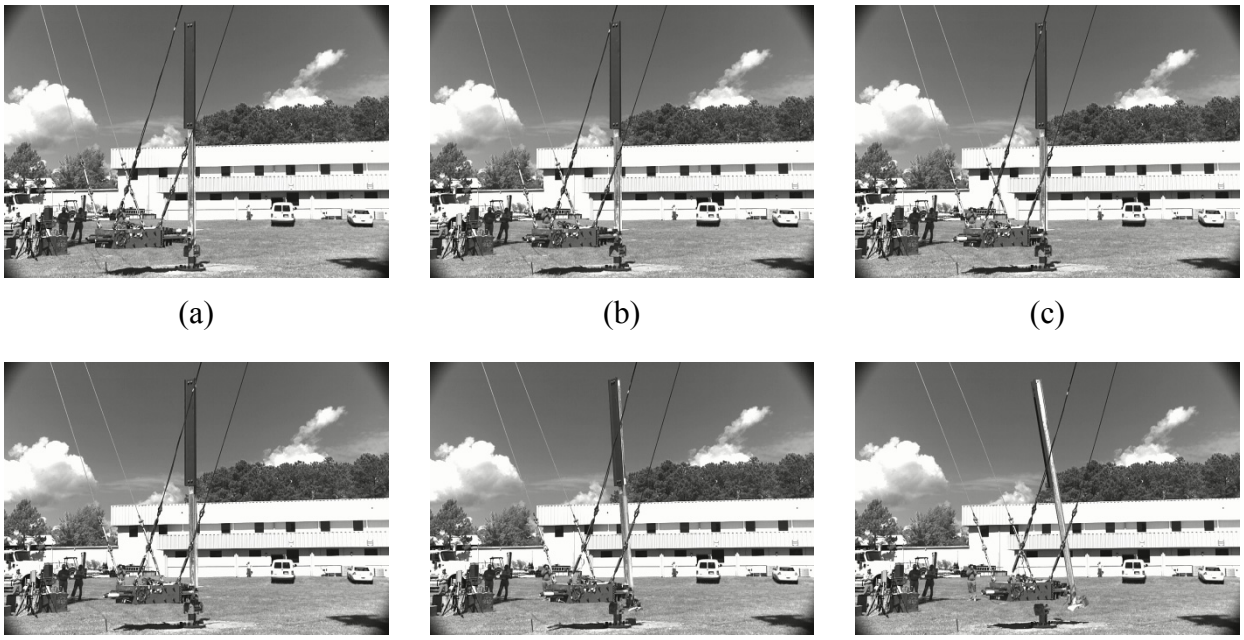

(a) (b) (c)

(d) (e) (f)

Figure 6.22 Wide angle high speed video frames from oblique (25 deg.)
19-mph impact test of low-capacity system

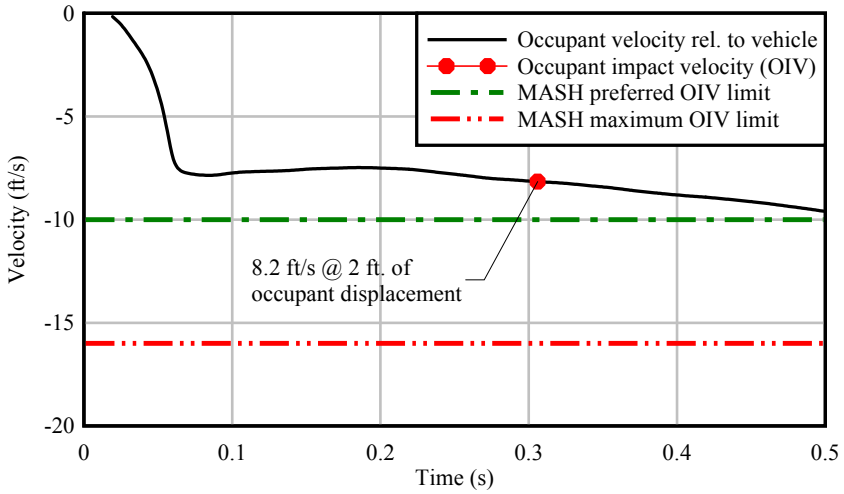

Figure 6.23 Occupant impact velocity (OIV) from oblique (25 deg.)
19-mph impact test of low-capacity system

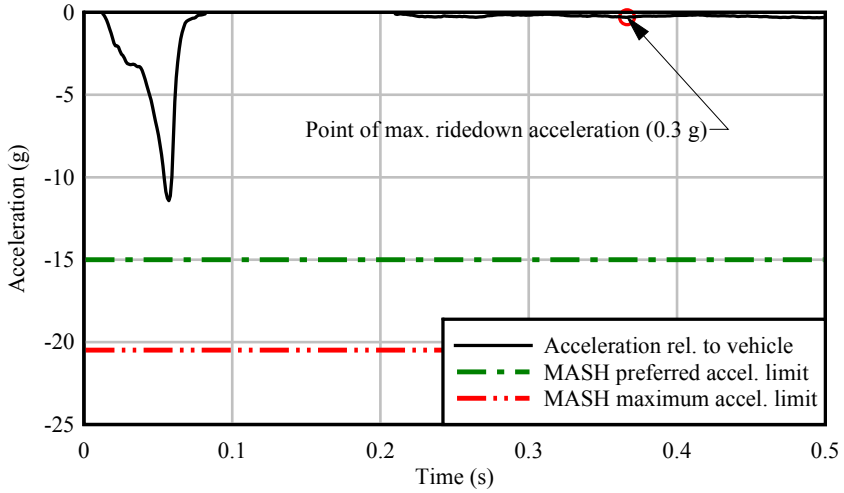

Figure 6.24 Occupant ridedown acceleration (ORA) from oblique (25 deg.)
19-mph impact test of low-capacity system

CHAPTER 7
CONCLUSIONS AND RECOMMENDATIONS

7.1 Conclusions

In the present study, the 'moment-resisting collar connection', originally developed in FDOT study BDK75-977-40, was redesigned based—in part—on reducing the design life from 50 years to 10 years. Using the revised 10-year design life, and computing correspondingly revised design wind loads, an updated (optimized and simplified) high-capacity moment collar breakaway connection was developed. Optimization of the system was achieved by reducing the weight (and mass) of key structural components, while simplification was achieved by minimizing the number of unique components fabricated, and also minimizing the use of welding. Scaled-down medium-capacity and low-capacity moment-collar connections were also developed. Collectively, the high-, medium-, and low-capacity connections developed in this study span the full range of sign post section depths currently employed in the FDOT Design Standards.

All three systems (high-, medium-, and low-capacity) were designed to meet the applicable AASHTO standards for flexural strength under wind loading (AASHTO LTS-6) and impact performance during vehicle collisions (AASHTO MASH). For vehicle impact loading, worst case conditions for assessing occupant risks—i.e., occupant impact velocity (OIV) and potential for vehicle compartment intrusion—were deemed to be associated with low-speed (19 mph) impacts from a MASH compliant 1100C surrogate passenger car. As such, all numerical simulations and physical tests were conducted under corresponding impact conditions. Collisions involving higher impact speeds and/or larger (more massive) vehicles (e.g., a pickup) would involve higher levels of kinetic energy, and should therefore result in lower occupant risks for the systems developed.

Demonstration of adequate structural performance was achieved using a combination of finite element simulation techniques (quasi-static pushover analyses and surrogate vehicle impact analyses) as well as physical validation testing (static flexural capacity testing and AASHTO MASH-compliant 1100C surrogate vehicle pendulum impact testing). Comparisons of finite element simulation results and physical test data indicated good agreement for system response to static flexural loading, and reasonable agreement for response to dynamic impact loading. Employing the use of galvanized articles during impact testing revealed the importance of accounting for galvanizing thickness when designing component clearances, and led to minor—but important—design changes.

7.2 Recommendations

This study focused on the development of breakaway connections for use in multi-post roadside sign structures. Based on the results of the numerical simulations and physical tests that were conducted, the following recommendations are made:

- Teflon sheets: To promote connection breakage under impact loading, Teflon sheets were used to reduce frictional forces between steel components that slide relative to one another. Making use of Teflon in this way, occupant impact velocities (OIVs) for *single-post* high-, medium-, and low-capacity breakaway test articles were found to be significantly less than the maximum permissible limit set forth in AASHTO MASH (2009). However, the

maximum (and controlling) OIV for a *three-post* sign structure was found—through numerical simulation—to be associated not with connection breakage but with subsequent rupture of the fuse-plate at the post mid-height. It may therefore be possible to eliminate the need for Teflon sheets, which were first introduced in FDOT study BDK75-977-40, from the breakaway connections developed in the present study. It is recommended that the feasibility of this change be explored initially using finite element simulation.

- AASHTO LRFD LTS-1: The roadside sign design specifications applicable during this study was AASHTO LTS-6 (2013, 2015). However, use of these specifications may be replaced in the future by the use of AASHTO LRFD LTS-1 (i.e., *The AASHTO LRFD Specifications for Structural Supports for Highway Signs, Luminaires, and Traffic Signals, 1st Edition*, 2015). If it is the intent of FDOT to implement AASHTO LRFD LTS-1 for roadside sign structures, then it is recommended that the structural adequacy of the connections developed in this study be verified using AASHTO LRFD LTS-1.

- Bottom transverse wind beams: Results from impact simulations of fully-detailed three-post sign structures—representing breakaway connections, segmented sign posts, fuse/hinge-plates, a sign panel, and transverse wind beams—revealed the importance of providing adequate strength and stiffness at the location of the bottommost wind beam (nearest the fuse plate). For fuse plates to survive under hurricane wind load, yet rupture under vehicle impact load, sufficient structural resistance must be provided by the bottom wind beam. It is recommended that either double aluminum Z-beams be provided at this bottom position, or that suitable alternative sections—with increased stiffness and strength—be provided.

- Assessment of potential for vehicle compartment intrusion: In this study, the risk for potential vehicle compartment intrusion (e.g., by a sign post) was assessed—using finite element impact simulation—for a large sign structure consisting of a near-maximum size sign panel supported on three posts, each utilizing the newly developed high-capacity breakaway connection system. This large-sign, three-post impact scenario was considered to be among the most critical cases for assessing vehicle compartment intrusion risk. However, if quantifying compartment intrusion risks for alternative impacts scenarios—e.g., those involving other vehicle types, or sign structures employing two (2) posts or a single (1) post—is deemed necessary, then such risks should be assessed using either numerical simulation techniques or physical tests.

REFERENCES

AASHTO (American Association of State Highway and Transportation Officials) (2009), *Manual for Assessing Safety Hardware (MASH) 2009,* American Association of State Highway and Transportation Officials, Washington, D.C.

AASHTO (2013), *Standard Specification for Structural Supports for Highway Signs, Luminaires and Traffic Signals, 6th Edition (LTS-6)*, American Association of State Highway and Transportation Officials, Washington, D.C.

AASHTO (2015), *Interim Revisions to Standard Specification for Structural Supports for Highway Signs, Luminaires and Traffic Signals, 6th Edition (LTS-6)*, Washington, D.C.

Consolazio, G., Bui, L., and Walters, R. (2012). *Pendulum impact testing of an impact-breakaway, wind resistant base connection for multi-post ground signs* (FDOT Research Project BDK-75-977-40), Structures Research Report No. 2012/92174, University of Florida, Gainesville, FL.

Consolazio, G., Hamilton, H., Groetaers, M., and Innocent, D. (2016). *Pendulum Impact Testing of Metallic, Non-metallic, and Hybrid Sign Posts* (FDOT Research Projects BDV31-977-16 and BDK75-977-42), Structures Research Report No. 2016/113605-113606, University of Florida, Gainesville, FL.

FDOT LTS-6 (2015), *FDOT Modifications to Standard Specification for Structural Supports for Highway Signs, Luminaires and Traffic Signals (LTS-6)*, FDOT Structures Manual, Vol. 3, Florida Department of Transportation, Jan. 2015.

FDOT SDG (2015), *FDOT Structures Design Guidelines*, FDOT Structures Manual, Vol. 1, Florida Department of Transportation, Jan. 2015.

Groetaers, M., Consolazio, G.R., Wagner, D.J., (2016), "Development of an 1100C Crushable Nose Surrogate Vehicle for Low Speed Impact Testing of Breakaway Hardware", *Transportation Research* Record*: Journal of the Transportation Research Board*, Number 2588, 2016, pp. 126-136.

LSTC (Livermore Software Technology Corporation) (2016). *LS-DYNA Keyword User's Manual*. LSTC, Livermore, CA.

Pinelli, J.P. and Subramanian (1999), *Study of Break-away Sign Base Connections, II* (FDOT Research Project BB-511), Report WPI No. 0510837, Aug. 1999.

Ross H.E., Jr., D.L. Sicking, R.A. Zimmer, and J.D. Michie (1993). *NCHRP Report 350: Recommended Procedures for the Safety Performance Evaluation of Highway Features*. TRB, National Research Council, Washington, D.C.

APPENDIX A:
CALCULATION OF WIND LOAD AND STEEL POST CAPACITY

Presented in this appendix is a calculation worksheet that was prepared to automate the processes of calculating wind loads on sign structures and checking structural adequacy for steel wide-flange sign posts. The worksheet was developed based on AASHTO LTS-6 (2013, 2015), FDOT LTS-6 (2015), and FDOT SDG (2015) and was used to establish discrete sizes of moment-resisting collar connections (high-capacity, medium-capacity, and low-capacity) that would be suitable for use with typical FDOT signage. An example application of the worksheet is presented.

Wind load calculations and steel post strength calculations: Basis for breakaway connection design

FDOT Project BDV31-977-24, UF Project 00114986 / 00114987
"Scaling and Validation of Breakaway Connection for Multi-post Ground Signs"
University of Florida, Department of Civil and Coastal Engineering

Reference documents:

(FDOT SDG 2015) *FDOT Structures Design Guidelines, FDOT Structures Manual, Volume 1, January 2015*

(FDOT LTS-6 2015) *FDOT Modifications to Standard Specifications for Structural Supports for Highway Signs, Luminaires, and Traffic Signals (LTS-6), FDOT Structures Manual, Volume 3, January 2015.*

(AASHTO LTS-6 2013) *AASHTO Standard Specifications for Structural Supports for Highway Signs, Luminaires, and Traffic Signals Sixth edition (LTS-6).*

$ORIGIN \equiv 1$

Design wind speed ...

FDOT LTS-6 2015, Section 3.8.2 indicates that "basic wind speed" should be determined from FDOT SDG (2015) Table 2.4.1-2.

FDOT SDG 2015, Section 2.4.1, Table 2.4.1-2 provides basic wind speeds for each Florida county ...

Table 2.4.1-2 Basic Wind Speed, V

County (Dist)	Basic Wind Speed (mph)	County (Dist)	Basic Wind Speed (mph)	County (Dist)	Basic Wind Speed (mph)
Alachua (2)	110	Hardee (1)	110	Okeechobee (1)	130
Baker (2)	110	Hendry (1)	130	Orange (5)	130
Bay (3)	130	Hernando (7)	130	Osceola (5)	130
Bradford (2)	110	Highlands (1)	130	Palm Beach (4)	150
Brevard (5)	130	Hillsborough (7)	130	Pasco (7)	130
Broward (4)	150	Holmes (3)	130	Pinellas (7)	130
Calhoun (3)	130	Indian River (4)	150	Polk (1)	110
Charlotte (1)	130	Jackson (3)	110	Putnam (2)	110
Citrus (7)	130	Jefferson (3)	110	St. Johns (2)	130
Clay (2)	110	Lafayette (2)	110	St. Lucie (4)	150
Collier (1)	150	Lake (5)	110	Santa Rosa (3)	150
Columbia (2)	110	Lee (1)	130	Sarasota (1)	130
DeSoto (1)	130	Leon (3)	110	Seminole (5)	130
Dixie (2)	130	Levy (2)	130	Sumter (5)	110
Duval (2)	130	Liberty (3)	130	Suwannee (2)	110
Escambia (3)	150	Madison (2)	110	Taylor (2)	130
Flagler (5)	130	Manatee (1)	130	Union (2)	110
Franklin (3)	130	Marion (5)	110	Volusia (5)	130
Gadsden (3)	110	Martin (4)	150	Wakulla (3)	130
Gilchrist (2)	110	Miami-Dade (6)	150	Walton (3)	130
Glades (1)	130	Monroe (6)	150	Washington (3)	130
Gulf (3)	130	Nassau (2)	130		
Hamilton (2)	110	Okaloosa (3)	130		

Conservatively choose V=150 mph as design basis for sign structure (based on worst-case Florida counties)

Conservatively select basic wind speed based on maximum values listed in table above.

$vWind := 150 \cdot mph$ ... FDOT SDG (2015); FDOT LTS-6 (2015)

For *comparison only*, based on AASHTO LTS-6, Figure 3.8.3-4 (below), maximum wind speed for coastal areas in Florida is the same as selected above.

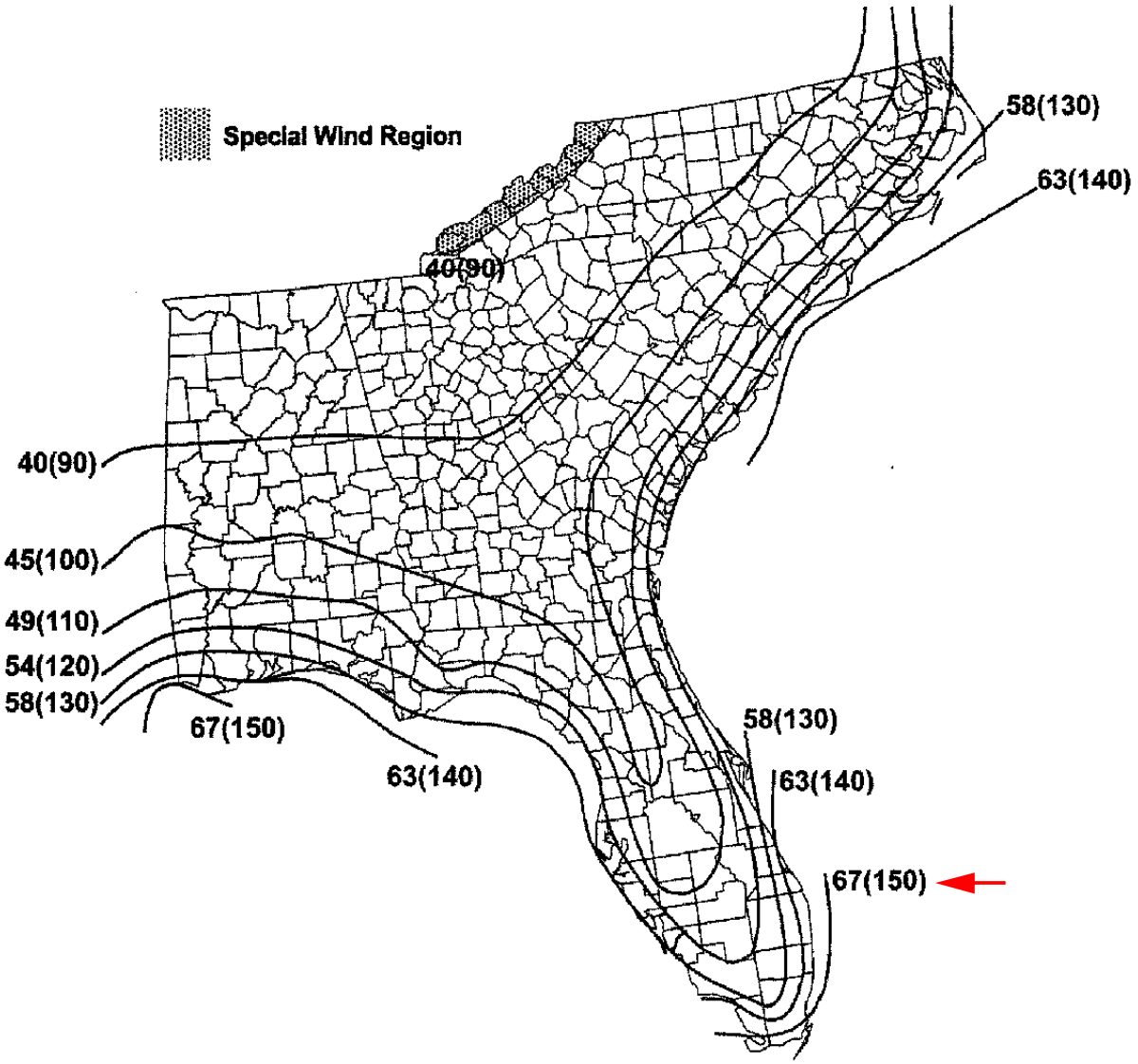

Notes:

1. Values are nominal design 3-s gust wind speeds in m/s (mph) at 10 m (33 ft) above ground for Exposure C category.
2. Linear interpolation between wind contours is permitted.
3. Islands and coastal areas outside the last contour shall use the last wind speed contour of the coastal area.
4. Mountainous terrain, gorges, ocean promontories, and special wind regions shall be examined for unusual wind conditions.

Figure 3.8.3-4—Basic Wind Speed, m/s (mph)—Eastern Gulf of Mexico and Southeastern U.S. Hurricane Coastline (ASCE 7-05)

Sign structure dimensions and post cross-sectional size...

hPanel := 12·ft ... vertical height of sign panel

wPanel := 20·ft ... horizontal width of sign panel

hClear := 11·ft ... clear height from ground surface to bottom edge of sign panel

section := "W10x26" ... steel post section designation

numPost := 3 ... number of support posts

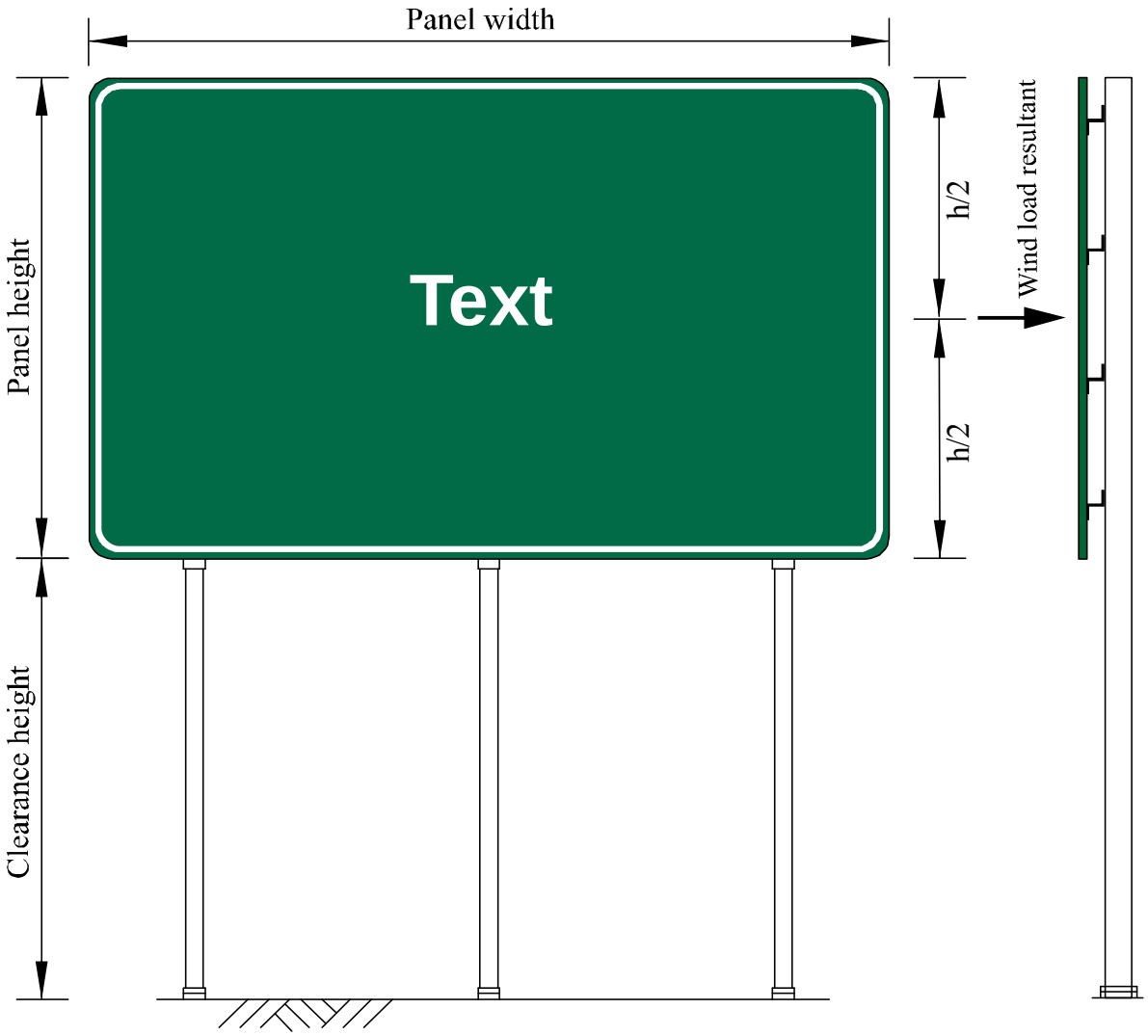

Design wind pressure per AASHTO LTS-6 ...

$Pz = 0.00256 \cdot Kz \cdot G \cdot V^2 \cdot Ir \cdot Cd$ (psf) ... (AASHTO LTS-6 Eqn. 3.8.3-1)

where ...

Pz = pressure (psf)
Kz = height and exposure factor
G = gust factor
V = basic wind speed (3-sec gust, 10 m above ground, open terrain, 50-yr mean recurrence)
Ir = importance factor
Cd = drag coefficient

Elevation (height) at which to compute wind load on sign panel ...

$hPanelWindLoad := hClear + \frac{1}{2} \cdot hPanel$ $hPanelWindLoad = 17.0 \cdot ft$ $hPanelWindLoad = 204.0 \cdot in$

Height and exposure factor Kz ...

$Kz = 2.01 \cdot \left(\frac{z}{z_g} \right)^{\frac{2}{\alpha}}$ ... AASHTO LTS-6 Eqn. C3.8.4-1 (as presented in ASCE 7)

where z is the greater of 1) the height above ground at which the pressure is calculated, or 2) 16ft. (AASHTO LTS-6, section C3.8.4)

$z(h) := \max(h, 16 \cdot ft)$

$z(hPanelWindLoad) = 17.0 \cdot ft$

Values of z_g and α are constants that vary with the exposure condition. Based on information presented in ASCE 7, and assuming exposure C, the values are : (AASHTO LTS-6, Section 3.8.4)

$exposure := "C"$

$\alpha := 9.5$

$z_g := 900 \cdot ft$

AASHTO LTS-6, Section C3.8.4:
"Exposure C has been adopted for use in these Specifications as it should provide an accurate or conservative approach for the design of structural supports. It represents open terrain with scattered obstructions."

Then ...

$Kz(z, z_g, \alpha) := 2.01 \cdot \left(\frac{z}{z_g} \right)^{\frac{2}{\alpha}}$

$KzPanel := Kz(z(hPanelWindLoad), z_g, \alpha)$

$KzPanel = 0.87$

Note: AASHTO LTS-6, Section C3.8.4:
"Kz is a height and exposure factor that varies with height above the ground depending on the local exposure conditions and may be conservatively set to 1.0 for heights less than 10 m (33 ft)."

Gust effect factor (G)

"The gust effect factor, G, shall be taken as a minimum of 1.14" (AASHTO LTS-6, section 3.8.5)

$G := 1.14$

AASHTO LTS-6, Commentary Section C3.8.5:

G is the gust effect factor and it adjusts the effective velocity pressure for the dynamic interaction of the structure with the gustiness of the wind.
...
Information presented in ASCE 7 states that if the fundamental frequency of a structure is less than 1 Hz or if the ratio of the height to least horizontal dimension is greater than 4, the structure should be designed as a wind-sensitive structure. Thus, virtually all structures addressed by these Specifications should be classified as wind-sensitive structures based on the height to least horizontal dimension ratio. It is not appropriate to use a nonwind-sensitive gust effect factor, G, for the design of sign, luminaire, and traffic signal structures.
...
Therefore, even though sign, luminaire, and traffic signal support structures are wind sensitive, the benefits of using the ASCE 7 gust effect factor calculation procedure do not outweigh the complexities introduced by its use.
...
Therefore, a gust effect factor, G, of 1.14 is recommended for the design of structural supports for signs, signals, and luminaires. Supports that have been designed with this past philosophy have performed well. Therefore, use of this philosophy is continued.

Recommended design life

For "roadside sign structures", FDOT LTS-6, Table 3-3 and AASHTO LTS-6, Table 3.8.3-2 both indicate a 10 year design life ...

$designLife := 10 \cdot yr$

FDOT LTS-6 Table 3-3

FDOT Table 3-3 Minimum Design Life

Design Life	Structure Type
50-year	Overhead sign structures
	Luminaire support structures >50' in height.
	Mast Arms
	Monotubes
	Steel Strain Poles
	ITS Camera Poles >50' in height
25-year	Luminaire supports and other structures ≤ 50' in height.
	Concrete Strain Poles
10-year	Roadside sign structures
1.5-year	Temporary construction signs

AASHTO LTS-6 Table 3.8.3-2

Table 3.8.3-2—Recommended Minimum Design Life

Design Life	Structure Type
50 yr	Overhead sign structures Luminaire support structures[a] Traffic signal structures[a]
10 yr	Roadside sign structures

[a] Luminaire support structures less than 15 m (50 ft) in height and traffic signal structures may be designed for a 25-yr design life, where locations and safety considerations permit and when approved by the Owner.

Importance factor (Ir)

For the chosen design life of ...

designLife = 10·yr

the importance factors are obtained from AASHTO LTS-6, Table 3.8.3-1 ...

IrNonHurricane := 0.71

IrHurricane := 0.54

AASHTO LTS-6, Table 3.8.3-1 ...

Table 3.8.3-1—Wind Importance Factors, I_r

Recurrence Interval Years	Basic Wind Speed in Non-hurricane Regions	Basic Wind Speed in Hurricane Regions with $V > 45$ m/s (100 mph)	Alaska
100	1.15	1.15	1.13
50	1.00	1.00	1.00
25	0.87	0.77[a]	0.89
10	0.71	0.54[a]	0.76

[a] The design wind pressure for hurricane wind velocities greater than 45 m/s (100 mph) should not be less than the design wind pressure using $V = 45$ m/s (100 mph) with the corresponding non-hurricane I_r value.

Drag coefficient (Cd)

For sign panels, Cd is based on the panel aspect ratio, AASHTO LTS-6, Table 3.8.6-1 ...

Table 3.8.6-1—Wind Drag Coefficients, C_d [a]

Sign Panel	
L_{sign}/W_{sign} = 1.0	1.12
2.0	1.19
5.0	1.20
10.0	1.23
15.0	1.30

Where L = max. sign panel dimension, and W = min. sign panel dimension. By definition, L/W cannot be less than 1.0. For intermediate values of aspect ratio not listed in table, use linear interpolation.

$$\begin{aligned}
&Cd(dim1, dim2) := \\
&\quad L \leftarrow \max(dim1, dim2) \\
&\quad W \leftarrow \min(dim1, dim2) \\
&\quad aspectRatio \leftarrow \frac{L}{W} \\
&\quad Cd \leftarrow 1.30 \quad \text{if } (aspectRatio > 15) \\
&\quad Cd \leftarrow \text{linterp}\left[\begin{pmatrix}1\\2\\5\\10\\15\end{pmatrix}, \begin{pmatrix}1.12\\1.19\\1.20\\1.23\\1.3\end{pmatrix}, aspectRatio\right] \quad \text{otherwise} \\
&\quad \text{return } (aspectRatio \quad Cd)
\end{aligned}$$

$(aspectRatio \quad CdPanel) := Cd(wPanel, hPanel)$

aspectRatio = 1.67

CdPanel = 1.17

Design wind pressure per AASHTO LTS-6 ...

$$PzAASHTO(Kz, G, V, Ir, Cd) := 0.00256 \cdot Kz \cdot G \cdot V^2 \cdot Ir \cdot Cd \cdot (psf)$$ ... (AASHTO LTS-6 Eqn. 3.8.3-1) where V=mph

AASHTO LTS-6, Section C3.8.1:

"For recurrence intervals of 10 or 25 years, the design wind pressure for hurricane wind velocities greater than ... (100 mph) should not be less than the design wind pressure calculated for V equal to ... (100 mph) and the corresponding non-hurricane Ir, value (Table 3.8.3-1)."

Hurricane wind condition

$KzPanel = 0.87$

$G = 1.14$

$vWind = 150 \cdot mph$

$IrHurricane = 0.54$

$CdPanel = 1.17$

$$PzPanel := PzAASHTO\left(KzPanel, G, \frac{vWind}{mph}, IrHurricane, CdPanel\right)$$

$PzPanel = 36.1 \cdot psf$

Check against lower limit pressure corresponding to V=100 mph and non-hurricane Ir

$KzPanel = 0.87$

$G = 1.14$

$vCheck := 100 \cdot mph$

$IrNonHurricane = 0.71$

$CdPanel = 1.17$

$$PzPanelLowerLimit := PzAASHTO\left(KzPanel, G, \frac{vCheck}{mph}, IrNonHurricane, CdPanel\right)$$

$PzPanelLowerLimit = 21.1 \cdot psf$

Wind pressure acting on the sign panel is the maximum of two pressures computed above ...

$$PzPanel := \max(PzPanel, PzPanelLowerLimit)$$

$PzPanel = 36.1 \cdot psf$

Wind pressure acting directly on each support post

Elevation (height) at which to compute wind load on sign post: choose middle of clear height ...

hPostWindLoad := hClear ÷ 2 hPostWindLoad = 5.50·ft hPostWindLoad = 66.00·in

Kz = height and exposure factor ...

KzPost := Kz(z(hPostWindLoad), z_g, α)

KzPost = 0.86

Drag coefficient (Cd) for steel post ...

For flat single members, Cd is given by AASHTO LTS-6, Table 3.8.6-1 ...

Table 3.8.6-1—Wind Drag Coefficients, C_d [a]—*Continued*

Single Member or Truss Member	$C_vVd \le 5.33$ m²/s (39 mph-ft)	5.33 m²/s (39 mph-ft) < C_vVd < 10.66 m²/s (78 mph-ft)	$C_vVd \ge 10.66$ m²/s (78 mph-ft)
Flat[d]	1.70	1.70	1.70

CdPost := 1.70 ... for "flat faced" members

Design wind pressure per AASHTO LTS-6 Eqn. 3.8.3-1 ...

designLife = 10·yr

G = 1.14

KzPost = 0.86

CdPost = 1.70

Hurricane wind condition

vWind = 150·mph IrHurricane = 0.54

PzPost := PzAASHTO(KzPost, G, vWind/mph, IrHurricane, CdPost)

PzPost = 51.9·psf

Check against lower limit pressure corresponding to V=100 mph and non-hurricane Ir

vCheck = 100·mph IrNonHurricane = 0.71

PzPostLowerLimit := PzAASHTO(KzPost, G, vCheck/mph, IrNonHurricane, CdPost)

PzPostLowerLimit = 30.3·psf

Wind pressure acting directly on support post ...

PzPost := max(PzPost, PzPostLowerLimit)

PzPost = 51.9·psf

Material properties of support post

$Fy := 50 \cdot ksi$ ... yield stress

$E := 29000 \cdot ksi$ ... elastic modulus of steel

Cross-sectional properties of support post

Steel section properties

section = "W10x26" ... steel post section designation

$(wt \quad bf \quad tf \quad d \quad tw \quad A \quad Ix \quad Iy) := getSectionProps(section)$ ... get cross-sectional properties from database

$wt := wt \cdot (plf)$ $wt = 26 \cdot plf$ ... weight per foot of length (lbf/ft = plf)

$bf := bf \cdot (in)$ $bf = 5.770 \cdot in$ ... flange width

$tf := tf \cdot (in)$ $tf = 0.440 \cdot in$ ... flange thickness

$d := d \cdot (in)$ $d = 10.330 \cdot in$ ... depth of section

$tw := tw \cdot (in)$ $tw = 0.260 \cdot in$ ... web thickness

$A := A \cdot \left(in^2\right)$ $A = 7.61 \cdot in^2$ ... cross-sectional area

$Ix := Ix \cdot \left(in^4\right)$ $Ix = 144.0 \cdot in^4$ ... strong axis moment of inertia

$Iy := Iy \cdot \left(in^4\right)$ $Iy = 14.1 \cdot in^4$ ... weak axis moment of inertia

Section moduli ...

$Sx := Ix \div \left(\frac{d}{2}\right)$ $Sx = 27.9 \cdot in^3$ ... section modulus, strong axis

$Sy := Iy \div \left(\frac{bf}{2}\right)$ $Sy = 4.9 \cdot in^3$ ... section modulus, weak axis

Radii of gyration of entire cross-section ...

$rx := \sqrt{\frac{Ix}{A}}$ $rx = 4.35 \cdot in$ ... about x-axis (strong axis)

$ry := \sqrt{\frac{Iy}{A}}$ $ry = 1.36 \cdot in$ ... about y-axis (weak axis)

Radius of gyration of T-shaped compression flange and 1/3 of compression web, about weak axis ...

$$rt := \sqrt{\frac{\left(\frac{1}{12} \cdot tf \cdot bf^3\right) + \left[\frac{1}{12} \cdot \left[\frac{1}{3} \cdot \frac{1}{2} \cdot (d - 2 \cdot tf)\right] \cdot tw^3\right]}{(tf \cdot bf) + \left[\frac{1}{3} \cdot \frac{1}{2} \cdot (d - 2 \cdot tf) \cdot tw\right]}} \qquad rt = 1.546 \cdot in$$

Web height (clear distance between flanges of beam) ...

$h := d - 2 \cdot tf$

$h = 9.45 \cdot in$

Calculation of loads acting on sign panel and post

Wind load on sign panel ...

areaPanel := wPanel·hPanel areaPanel = 240.0·ft^2

loadWindOnPanel := PzPanel·areaPanel

loadWindOnPanel = 8.65·kip

Wind load on a single sign post ...

areaPost := hClear·bf areaPost = 5.29·ft^2

loadWindOnSinglePost := PzPost·areaPost

loadWindOnSinglePost = 0.27·kip

Dead load (weight, gravity load) of panel ...

Estimated weight of sign panel, wind beams, and connection hardware ...

pPanelSelfWt := 4·psf ... per FDOT Multi-Post 2001 Sign v1.21 MathCad program

loadWeightOfPanel := pPanelSelfWt·areaPanel

loadWeightOfPanel = 0.96·kip

Dead load (weight, gravity load) of a single post ...

hPost := hClear + hPanel hPost = 23.0·ft ... conservatively estimate total post height as clear height plus panel height (see FDOT index drawing 11200)

loadWeightOfSinglefPost := hPost·wt

loadWeightOfSinglefPost = 0.60·kip

Compute *total* forces at base of posts (at breakaway connection elevation)

axialBase := loadWeightOfPanel + numPost·loadWeightOfSinglefPost

axialBase = 2.75·kip

shearBase := loadWindOnPanel + numPost·loadWindOnSinglePost

shearBase = 9.48·kip

momentBase := loadWindOnPanel·hPanelWindLoad + (numPost·loadWindOnSinglePost)·hPostWindLoad

momentBase = 151.6·kip·ft momentBase = 1820·kip·in

Compute design forces per post

Distribution factor for a representative post ...

distFactVar := 20·% ... account for potential variations in distribution factor (due to irregular spacings, etc.)

distFactVar = 0.20

$$distFactPost := \left(\frac{1 + distFactVar}{numPost}\right)$$ distFactPost = 0.40 ... distribution factor for representative post

Compute design forces for ***single post*** at base (i.e., at breakaway connection elevation)

distFactPost = 0.40

axialPost := distFactPost·axialBase

shearPost := distFactPost·shearBase

momentPost := distFactPost·momentBase

axialPost = 1.10·kip

shearPost = 3.79·kip

momentPost = 60.7·kip·ft

momentPost = 728·kip·in

Compute post stresses due to design forces ...

Axial stress:

axialPost = 1.10·kip $A = 7.61 \cdot in^2$

$fa := \frac{axialPost}{A}$ fa = 0.14·ksi

Shear stress:

shearPost = 3.79·kip Aw := d·tw $Aw = 2.69 \cdot in^2$

$fv := \frac{shearPost}{Aw}$ fv = 1.41·ksi

Bending stress:

momentPost = 60.7·kip·ft $Ix = 144 \cdot in^4$ $c := \frac{d}{2}$ $c = 5.17 \cdot in$

$fb := \frac{momentPost \cdot c}{Ix}$ fb = 26.11·ksi

Unbraced length of post (for allowable bending stress calculations) ...

$Lunbraced := hClear + \frac{1}{2} \cdot hPanel$

... assumes (conservatively) that wind beams are not able to brace the compression flange of the post, and that therefore the unbraced length spans from the base to the elevation of the resultant panel wind load.

Lunbraced = 17.0·ft

hPanelWindLoad = 17.0·ft

ALLOWABLE BENDING STRESS

Steel section classification: compact, non-compact, slender

AASHTO LTS-6, Section 5.5.3, Table 5.5.4-1 ...

Table 5.5.4-1—Width–Thickness Ratios for Nontubular Sections

Description of Section	Width–Thickness Ratio λ	Compact Limit λ_p	Noncompact Limit λ_r
Flanges of I-shaped Beams and Channels in Flexure	$\frac{b}{t}$	$0.38\sqrt{\frac{E}{F_y}}$	$0.56\sqrt{\frac{E}{F_y}}$
Unstiffened Elements (i.e., simply supported along one edge)	$\frac{b}{t}$	N/A	$0.45\sqrt{\frac{E}{F_y}}$
Stems of Tees	$\frac{d}{t}$	N/A	$0.75\sqrt{\frac{E}{F_y}}$
All Other Uniformly Compressed Stiffened Elements (i.e., supported along two edges)	$\frac{b}{t}$	N/A	$1.49\sqrt{\frac{E}{F_y}}$
	$\frac{h}{t_w}$		
Webs in Flexural Compression	$\frac{d}{t}$	$3.76\sqrt{\frac{E}{F_y}}$	N/A
	$\frac{h}{t_w}$	N/A	$4.46\sqrt{\frac{E}{F_y}}$
Webs in Combined Flexural and Axial Compression	$\frac{d}{t_w}$	$for\ \frac{f_a}{F_y} \le 0.16,\quad 3.76\sqrt{\frac{E}{F_y}}\left(1-3.74\frac{f_a}{F_y}\right)$ $for\ \frac{f_a}{F_y} > 0.16,\quad 1.51\sqrt{\frac{E}{F_y}}$	N/A

Where ...

λ for "Flanges of I-shapes beams ... in flexure" is $\lambda = \frac{b}{t} = \frac{bf \div 2}{tf}$

λ for "Webs in combined Flexural and Axial Compression" is $\lambda = \frac{d}{tw}$

Section classification "flags" ...

classCompact := 1

classNonCompact := 2

classSlender := 3

Function for converting numeric classification flags into readable strings ...

```
classString(class) := | out ← "COMPACT"     if class = classCompact
                      | out ← "NON-COMPACT"  if class = classNonCompact
                      | out ← "SLENDER"      if class = classSlender
                      | return out
```

Classify the flange (as compact, non-compact, or slender) ...

$\lambda := \frac{(bf \div 2)}{tf}$ $\lambda = 6.56$ $\sqrt{\frac{E}{Fy}} = 24.08$ $0.38 \cdot \sqrt{\frac{E}{Fy}} = 9.15$ $0.56 \cdot \sqrt{\frac{E}{Fy}} = 13.49$

flangeClass :=
- out ← classCompact if $\lambda \le 0.38 \cdot \sqrt{\frac{E}{Fy}}$
- out ← classNonCompact if $0.38 \cdot \sqrt{\frac{E}{Fy}} < \lambda \le 0.56 \cdot \sqrt{\frac{E}{Fy}}$
- out ← classSlender if $\lambda > 0.56 \cdot \sqrt{\frac{E}{Fy}}$
- return out

flangeClass = 1 flangeClassResult := concat("Flange is ", classString(flangeClass), ".")

Classify the web (as compact, or slender) ...

$\lambda := \frac{d}{tw}$ $\lambda = 39.73$ $\sqrt{\frac{E}{Fy}} = 24.08$ $1.51 \cdot \sqrt{\frac{E}{Fy}} = 36.37$

$fa = 0.14 \cdot ksi$ $Fy = 50.00 \cdot ksi$ $\frac{fa}{Fy} = 0.002895$ $3.76 \cdot \sqrt{\frac{E}{Fy}} \cdot \left[1 - 3.74 \cdot \left(\frac{fa}{Fy}\right)\right] = 89.57$

webClass :=
- if $\frac{fa}{Fy} \le 0.16$
  - out ← classCompact if $\lambda \le 3.76 \cdot \sqrt{\frac{E}{Fy}} \cdot \left[1 - 3.74 \cdot \left(\frac{fa}{Fy}\right)\right]$
  - out ← classSlender otherwise
- if $\frac{fa}{Fy} > 0.16$
  - out ← classCompact if $\lambda \le 1.51 \cdot \sqrt{\frac{E}{Fy}}$
  - out ← classSlender otherwise
- return out

webClass = 1 webClassResult := concat("Web is ", classString(webClass), ".")

Overall section classification based on worst-case of flange and web classifications ...

sectionClass := max(flangeClass, webClass)

sectionClassResult := concat("Section is ", classString(sectionClass), ".")

Classification results ...

flangeClassResult = "Flange is COMPACT."

webClassResult = "Web is COMPACT."

sectionClassResult = "Section is COMPACT."

AASHTO LTS-6 Section 5.7 Allowable bending stress for flanged I-shaped members

LTS-6 Section 5.7.1.1: Members with Compact and Noncompact Sections and Adequate Lateral Support:
For a flexural element to be considered "adequately laterally supported" per AASHTO, the unbraced length must be less than the limit given by ...

$$LsupMax := 0.45 \cdot bf \cdot \sqrt{\frac{E}{Fy}}$$ AASHTO LTS-6 Eqn. 5.7.1.1-1

$LsupMax = 5.2 \cdot ft$

$Lunbraced = 17.0 \cdot ft$

bracedStatus :=
msg ← "Adequate lateral support provided: Post is BRACED." if Lunbraced ≤ LsupMax
msg ← "Inadequate lateral support provided: Post is UN-BRACED." otherwise
return msg

bracedStatus = "Inadequate lateral support provided: Post is UN-BRACED."

Moment gradient coefficient, Cb :

$$Cb = 1.75 + 1.05 \cdot \left(\frac{M1}{M2}\right) + 0.3 \cdot \left(\frac{M1}{M2}\right)^2 \leq 2.3$$ AASHTO LTS-6 Eqn. 5.7.1.2-5

where:

M1 is the smaller end moment of the unbraced segment
M2 is the larger end moment of the unbraced segment
(M1/M2) is negative for single curvature
(M1/M2) is positive for reverse curvature

For the cantilever sign structure under consideration ...

$M2 := momentPost$ $M2 = 60.7 \cdot kip \cdot ft$ ... moment at base of post

$M1 := 0 \cdot kip \cdot ft$ $M1 = 0.0 \cdot kip \cdot ft$ ... moment at elevation of resultant panel wind load

$M1OverM2 := -(M1 \div M2)$ ... post is in single curvature, so (M1/M2) = negative (-)

$M1OverM2 = 0.00$

$$Cb := \min\left[1.75 + 1.05 \cdot (M1OverM2) + 0.3 \cdot (M1OverM2)^2, 2.3\right]$$ AASHTO LTS-6 Eqn. 5.7.1.2-5

$Cb = 1.75$

AASHTO LTS-6 Section 5.7.1.2 :
Members with Compact and Noncompact Sections and with Inadequate Lateral Support:

"For I-shaped members, symmetrical about and loaded in the plane of their minor axis, the allowable bending stress in compression *Fb,* shall be determined as the larger value from Eqs. 5.7.1.2-2, 5.7.1.2-3, and 5.7.1.2-4, but not more than *0.6Fy*" where ...

L = distance between cross-sections braced against twist or lateral displacement of the compression flange
rt = radius of gyration of a section comprising the compression flange plus 1/3 of the compression web area, taken about an axis in the plane of the web
Af = area of compression flange
Cb = the moment gradient coefficient

Allowable bending stress: Use the ***larger*** value computed from "Case 1" and "Case 2" calculations below, but limited to a maximum of 0.6Fy ...

Case 1 ...

$Fb = 0.6 \cdot Fy$ for $\frac{L}{rt} < \sqrt{3.52 \cdot Cb \cdot \frac{E}{Fy}}$

$Fb = 0.67 \cdot \left[1 - \left[\frac{0.03 \cdot \left(\frac{L}{rt} \right)^2}{Cb \cdot \frac{E}{Fy}} \right] \right] \cdot Fy$ for $\sqrt{3.52 \cdot Cb \cdot \frac{E}{Fy}} \le \frac{L}{rt} \le \sqrt{17.59 \cdot Cb \cdot \frac{E}{Fy}}$ AASHTO LTS-6 Eqn. 5.7.2-2

$Fb = \frac{5.86 \cdot Cb \cdot E}{\left(\frac{L}{rt} \right)^2}$ for $\frac{L}{rt} > \sqrt{17.59 \cdot Cb \cdot \frac{E}{Fy}}$ AASHTO LTS-6 Eqn. 5.7.2-3

Case 2 ...

$Fb = \frac{0.41 \cdot Cb \cdot E}{\frac{L \cdot d}{Af}}$ AASHTO LTS-6 Eqn. 5.7.2-4

Strength limit ...

$Fb \le 0.6 \cdot Fy$ maximum permissible allowable bending stress

---

$L := Lunbraced$ $L = 17.00 \cdot ft$

$L \div rt = 131.96$

$Af := bf \cdot tf$ $Af = 2.54 \cdot in^2$

$d = 10.33 \cdot in$

$Cb = 1.75$

$E = 29000 \cdot ksi$

$Fy = 50 \cdot ksi$

Maximum allowable bending stress ...

$FbMax := 0.6 \cdot Fy \qquad FbMax = 30.0 \cdot ksi$

Compute allowable bending stress ...

$$Fb := \left| \begin{array}{l} FbCase1 \leftarrow 0.6 \cdot Fy \quad \text{if} \quad \left(\frac{L}{rt}\right) < \sqrt{3.52 \cdot Cb \cdot \frac{E}{Fy}} \\ FbCase1 \leftarrow 0.67 \cdot \left[1 - \left[\frac{0.03 \cdot \left(\frac{L}{rt}\right)^2}{Cb \cdot \frac{E}{Fy}}\right]\right] \cdot Fy \quad \text{if} \quad \sqrt{3.52 \cdot Cb \cdot \frac{E}{Fy}} \le \left(\frac{L}{rt}\right) \le \sqrt{17.59 \cdot Cb \cdot \frac{E}{Fy}} \\ FbCase1 \leftarrow \frac{5.86 \cdot Cb \cdot E}{\left(\frac{L}{rt}\right)^2} \quad \text{if} \quad \left(\frac{L}{rt}\right) > \sqrt{17.59 \cdot Cb \cdot \frac{E}{Fy}} \\ FbCase2 \leftarrow \frac{0.41 \cdot Cb \cdot E}{\frac{L \cdot d}{Af}} \\ Fb \leftarrow \max(FbCase1, FbCase2) \\ Fb \leftarrow \min(Fb, FbMax) \\ \text{return } Fb \end{array} \right.$$

$Fb := \text{if}(sectionClass = classCompact, Fb, \text{"Error: Fb not computed because section is not compact."})$

$Fb = 25.1 \cdot ksi$

ALLOWABLE SHEAR STRESS

AASHTO LTS-6 Section 5.11.3: Allowable shear stress for I-shaped sections

$Fv = 0.33 \cdot Fy \quad \text{for} \quad \frac{h}{tw} \le 2.23 \cdot \sqrt{\frac{E}{Fy}}$ AASHTO LTS-6 Eqn. 5.11.3-1

$h = 9.45 \cdot in \qquad tw = 0.26 \cdot in \qquad \frac{h}{tw} = 36.35$

$$Fv := \left| \begin{array}{l} Fv \leftarrow 0.33Fy \quad \text{if} \quad \frac{h}{tw} \le 2.23 \cdot \sqrt{\frac{E}{Fy}} \\ Fv \leftarrow \text{"Error: Web slenderness limit exceeded. Allowable shear stress cannot be computed."} \quad \text{otherwise} \\ \text{return } Fv \end{array} \right.$$

$Fv = 16.5 \cdot ksi$

AASHTO LTS-6, Section 5.11.3:

"The allowable shear stress shall be applied over an effective area consisting of the full member depth (d) times the web thickness (tw)." Thus, the acting shear stress, fv, computed earlier uses an area of Aw = (d)*(tw).

ALLOWABLE AXIAL COMPRESSION STRESS

AASHTO LTS-6, Section 5.10:

The allowable axial compression stress Fa, shall be calculated as follows:

$$Fa = \frac{\left[1 - \frac{\left(\frac{k \cdot L}{r}\right)^2}{2 \cdot Cc^2}\right] \cdot Fy}{\frac{5}{3} + \frac{3 \cdot \left(\frac{k \cdot L}{r}\right)}{8 \cdot Cc} - \frac{\left(\frac{k \cdot L}{r}\right)^3}{8 \cdot Cc^3}} \quad \text{for} \quad \frac{k \cdot L}{r} < Cc \qquad \text{AASHTO LTS-6 Eqn. 5.10-1}$$

$$Fa = \frac{12 \cdot \pi^2 \cdot E}{23 \cdot \left(\frac{k \cdot L}{r}\right)^2} \quad \text{for} \quad \frac{k \cdot L}{r} \geq Cc \qquad \text{AASHTO LTS-6 Eqn. 5.10-2}$$

where...

kL/r is the largest effective slenderness ratio of any unbraced segment, and Cc is given by:

$$Cc := \sqrt{\frac{2 \cdot \pi^2 \cdot E}{Fy}} \qquad \text{AASHTO LTS-6 Eqn. 5.10-3)}$$

$Cc = 107.0$ ... transition slenderness (kL/r) between inelastic axial buckling and elastic axial buckling

Computation of slenderness ratio, kL/r ...

$k := 2.1$ ... AASHTO Section C5.10 "For a cantilever column, the effective length factor *k* may be taken as 2.1"

$L := hClear + \frac{hPanel}{2}$ ... conservatively assume that the majority of the axial load applied to the post comes from the sign panel weight, and assume (conservatively) that this weight is applied to post as a concentrated downward load acting at the mid-height elevation of the sign panel.

$L = 17.0 \cdot ft$

$rx = 4.35 \cdot in$

$ry = 1.36 \cdot in$

$r := \min(rx, ry)$ ... minimum radius of gyration will produce the largest kL/r (axial buckling will be about the axis with the minimum radius of gyration).

$r = 1.36 \cdot in$

$\frac{k \cdot L}{r} = 314.7$

Allowable axial compressive stress calculation ...

$$Fa := \left| \begin{array}{l} Fa \leftarrow \dfrac{\left[1 - \dfrac{\left(\frac{k \cdot L}{r}\right)^2}{2 \cdot Cc^2}\right] \cdot Fy}{\frac{5}{3} + \dfrac{3 \cdot \left(\frac{k \cdot L}{r}\right)}{8 \cdot Cc} - \dfrac{\left(\frac{k \cdot L}{r}\right)^3}{8 \cdot Cc^3}} \quad \text{if} \quad \left(\dfrac{k \cdot L}{r}\right) < Cc \\ Fa \leftarrow \dfrac{12 \cdot \pi^2 \cdot E}{23 \cdot \left(\frac{k \cdot L}{r}\right)^2} \quad \text{if} \quad \dfrac{k \cdot L}{r} \geq Cc \\ \text{return } Fa \end{array} \right.$$

$Fa = 1.51 \cdot ksi$

Load Combinations and allowable stress increase

AASHTO LTS-6, Section 3.4:

"The loads ... shall be combined into appropriate group load combinations as stipulated in Table 3.4-1. Each part of the structure shall be proportioned for the combination producing the maximum load effect, using allowable stresses increased as indicated for the group load."

Table 3.4-1—Group Load Combinations

Group Load	Load Combination[a]	Percentage of Allowable Stress[b]
I	*DL*	100
II	*DL* + *W*	133
III	*DL* + *Ice* + $^1/_2$(*W*)[c]	133
IV	Fatigue	[d]

AASHTO LTS-6 Table 3.4-1

Notes:

[a] See Article 3.6 regarding application of live load.

[b] Percentages of allowable stress are applicable for the allowable stress design method. No load reduction factors shall be applied in conjunction with these increased allowable stresses.

[c] *W* shall be computed based on the wind pressure. A minimum value of 1200 Pa (25 psf) shall be used for *W* in Group III.

[d] See Section 11 for fatigue loads and stress range limits

Increase allowable stresses for Group Load II : DL+W (dead load + wind load) ...

AASHTO Section 5.12, "Calculations of Fa, Fb, F'e, Fv, and 0.6Fy in Eqns. ... may be increased by 1/3 for Groups II and III, as allowed in AASHTO Section 3: Loads".

$strInc := 1.33$ ... stress increase factor for Group II : DL+W

AASHTO LTS-6, Section 5.12.2.1:

"All members that are subjected to axial compression, bending moment, shear, and torsion, except vertical cantilever pole-type supports, shall meet the following" [combined stress ratio (CSR) equations] :

$$\frac{fa}{strInc \cdot 0.6 \cdot Fy} + \frac{fb}{strInc \cdot Fb} + \left(\frac{fv}{strInc \cdot Fv}\right)^2 \le 1.0$$ AASHTO LTS-6 Eqn. 5.12.2.1-1

$$\frac{fa}{strInc \cdot Fa} + \frac{fb}{\left(1 - \frac{fa}{F'e}\right) \cdot strInc \cdot Fb} + \left(\frac{fv}{strInc \cdot Fv}\right)^2 \le 1.0$$ AASHTO LTS-6 Eqn. 5.12.2.1-2

where ...

$$F'e = \frac{12 \cdot \pi^2 \cdot E}{23 \cdot \left(\frac{k \cdot L}{r}\right)^2}$$

AASHTO LTS-6, Eqn. 5.12.2.1-3 "which is calculated in the plane of bending". F'e is used to compute a moment amplification correction term (1 - fa/F'e) related to axial load and lateral deflection (bending) of the section, which in the case of the sign post considered here occurs about the strong (x-) axis of the post. Therefore, use k = 2.1 (for a cantilever), L = same unbraced length used earlier to compute Fb, and radius of gyration rx (strong axis).

$k = 2.10$ ... value assigned earlier for Fb calculation (allowable bending stress calculation)

$L := Lunbraced$ $L = 17.0 \cdot ft$

$r := rx$ $r = 4.35 \cdot in$

$F'e := \frac{12 \cdot \pi^2 \cdot E}{23 \cdot \left(\frac{k \cdot L}{r}\right)^2}$ $F'e = 15.4 \cdot ksi$ $\frac{fa}{F'e} = 0.009402$ $1 - \frac{fa}{F'e} = 0.991$

Evaluate combined stress ratios (CSRs) ...

$CSR1 := \frac{fa}{strInc \cdot 0.6 \cdot Fy} + \frac{fb}{strInc \cdot Fb} + \left(\frac{fv}{strInc \cdot Fv}\right)^2$ $CSR1 = 0.79$ $\frac{fb}{strInc \cdot Fb} = 0.78$

$CSR2 := \frac{fa}{strInc \cdot Fa} + \frac{fb}{\left(1 - \frac{fa}{F'e}\right) \cdot strInc \cdot Fb} + \left(\frac{fv}{strInc \cdot Fv}\right)^2$ $CSR2 = 0.87$ $\frac{fb}{\left(1 - \frac{fa}{F'e}\right) \cdot strInc \cdot Fb} = 0.79$

$CSR := \max(CSR1, CSR2)$ $CSR = 0.87$

```
designResult := | strCSR ← num2str(round(CSR, 2))
                | msg ← concat(section, " section is adequate. Combined stress ratio = ", strCSR)  if  CSR ≤ 1
                | msg ← concat(section, " section is NOT ADEQUATE. Combined stress ratio = ", strCSR)  if  CSR > 1
                | return  msg
```

designResult = "W10x26 section is adequate. Combined stress ratio = 0.87"

APPENDIX B:
STRUCTURAL DRAWINGS FOR
HIGH-CAPACITY BREAKAWAY CONNECTION SYSTEM

Presented in this appendix are structural drawings for the high-capacity breakaway connection system developed and tested in this study.

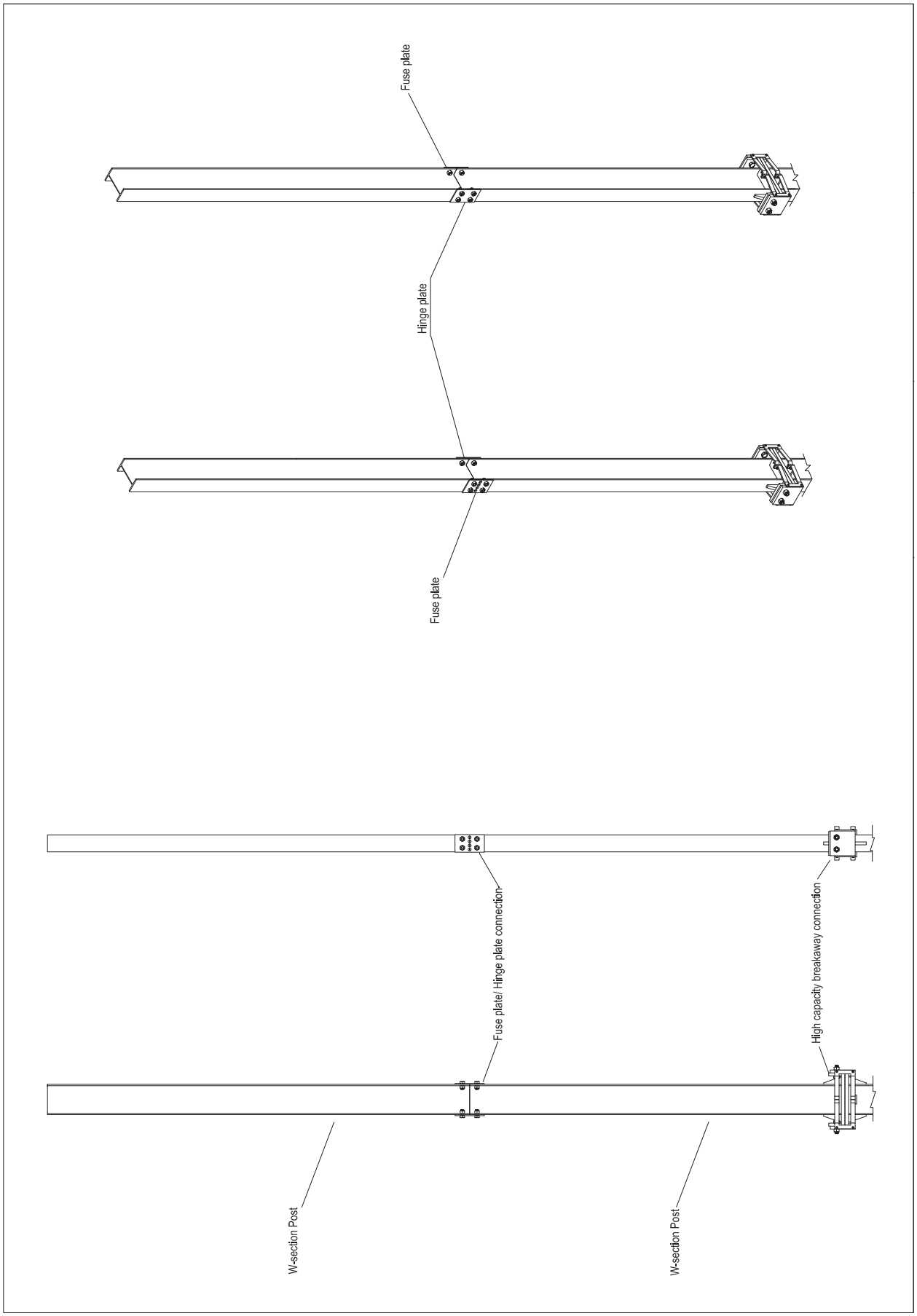
Fuse plate
Hinge plate
Fuse plate
Fuse plate/ Hinge plate connection
High capacity breakaway connection
W-section Post
W-section Post

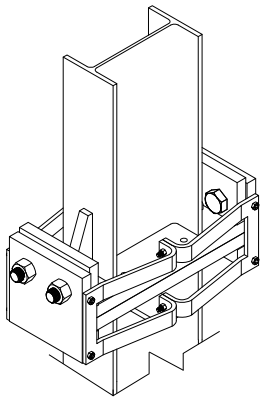

Assembled system

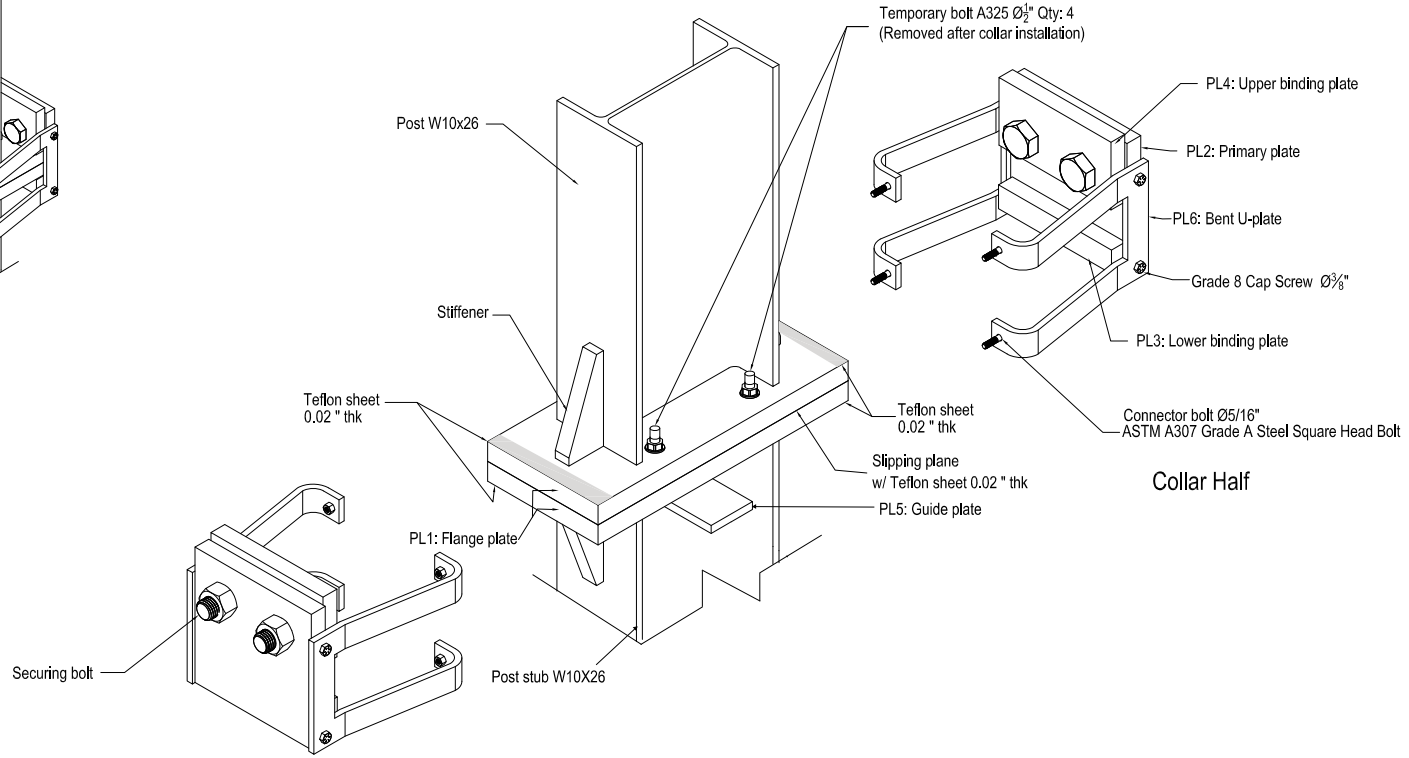

Note: All steel is A572 Gr. 50 unless otherwise noted.

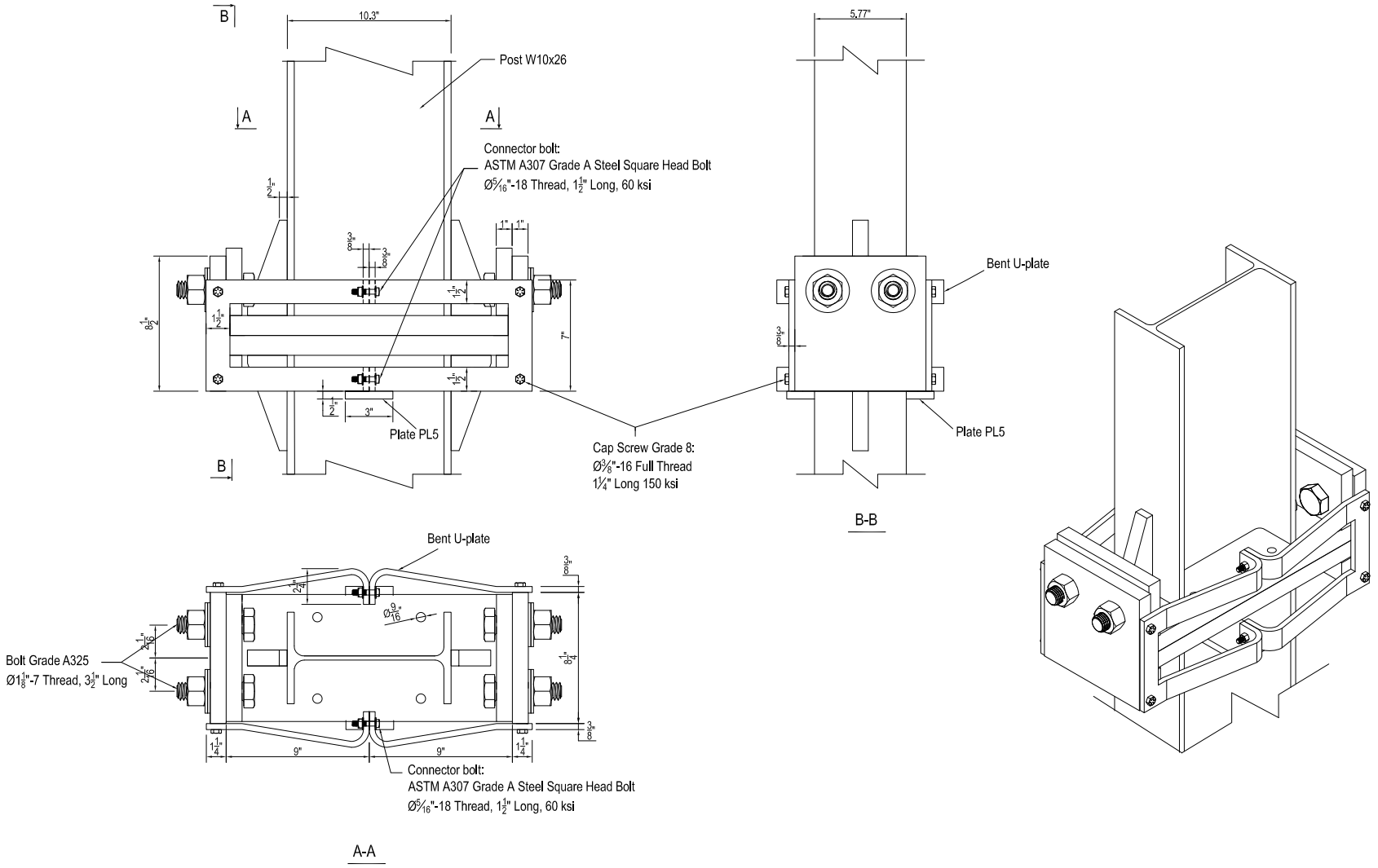
B
10.3"
Post W10x26
A
A
Connector bolt:
ASTM A307 Grade A Steel Square Head Bolt
Ø5/16"-18 Thread, 1 1/2" Long, 60 ksi
1/2"
1"
1"
3 cm
3 cm
1 1/2"
1 1/2"
1 1/2"
1 1/2"
7"
3"
Plate PL5
B
Cap Screw Grade 8:
Ø3/8"-16 Full Thread
1 1/4" Long 150 ksi
5.77"
Bent U-plate
3 cm
Plate PL5
B-B
Bent U-plate
2 1/2"
Ø9/16"
3 cm
Bolt Grade A325
Ø1 1/8"-7 Thread, 3 1/2" Long
1 3/16"
2 3/16"
8 1/4"
1 1/4"
9"
9"
1 1/4"
3 cm
Connector bolt:
ASTM A307 Grade A Steel Square Head Bolt
Ø5/16"-18 Thread, 1 1/2" Long, 60 ksi
A-A

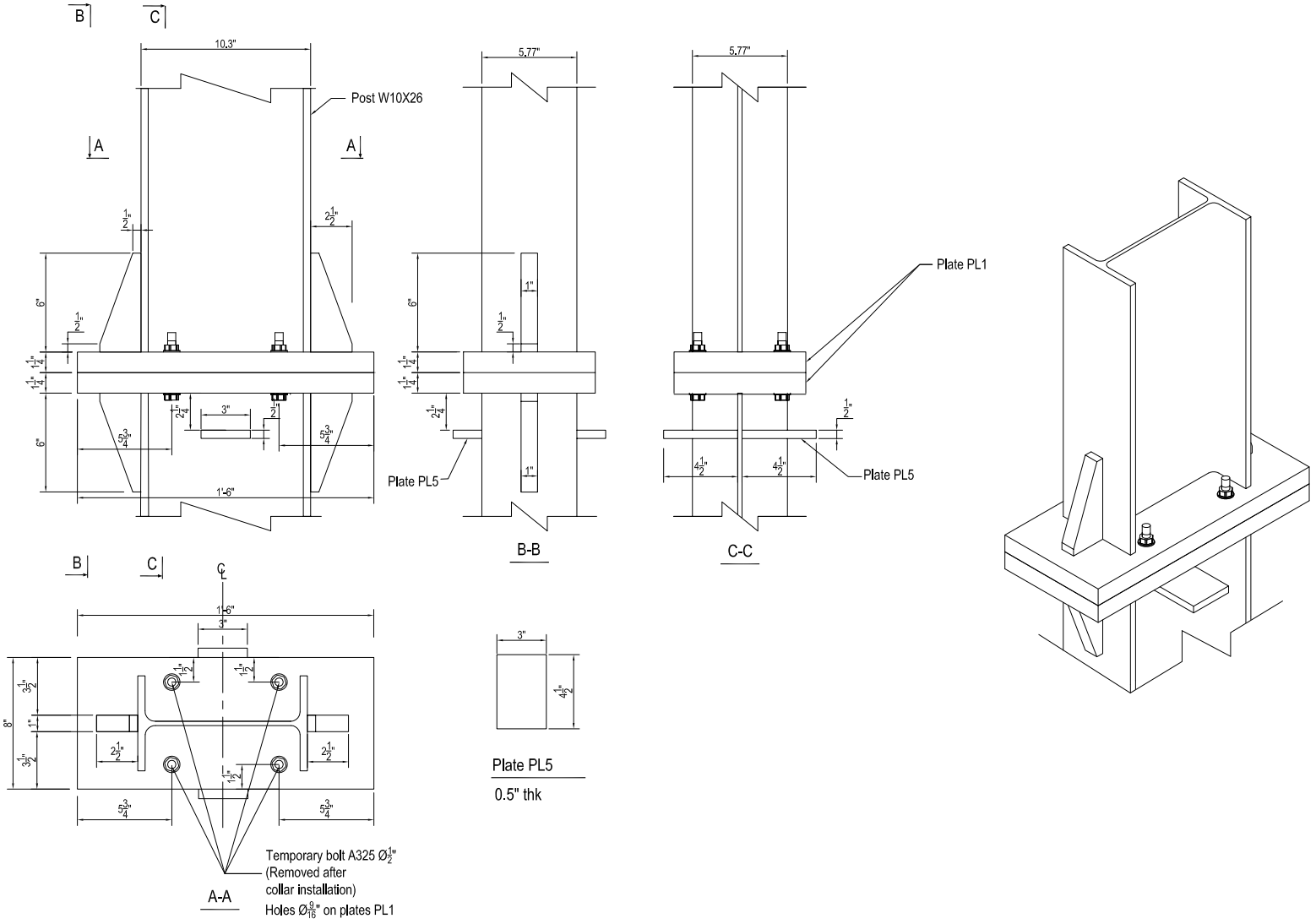
B
C
10.3"
Post W10X26
A
A
1/2"
2 1/2"
6"
1/2"
1 1/4"
1 1/4"
2 1/4"
3"
2 1/2"
5 3/4"
5 3/4"
6"
1'-6"
5.77"
1"
1/2"
6"
1 1/4"
1 1/4"
2 1/4"
Plate PL5
1"
B-B
5.77"
Plate PL1
1/2"
4 1/2"
4 1/2"
Plate PL5
C-C
B
C
C
1'-6"
2 1/4"
1 1/2"
1 1/2"
3 1/2"
8"
1"
3 1/2"
2 1/2"
2 1/2"
1/2"
5 3/4"
5 3/4"
Temporary bolt A325 Ø1/2"
(Removed after
collar installation)
Holes Ø9/16" on plates PL1
A-A
3"
4 1/2"
Plate PL5
0.5" thk

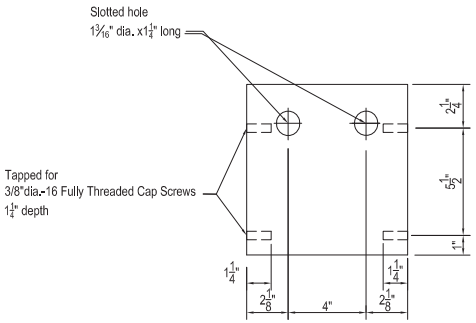

PRIMARY PLATE: PL2
Plate thickness= 1"

LOWER BINDING PLATE: PL3
Plate thickness= 1"

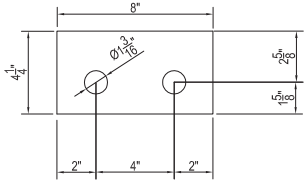

UPPER BINDING PLATE: PL4
Plate thickness= 1"

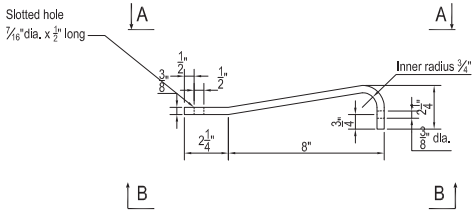

PLAN VIEW OF BENT U-PLATE: PL6
Plate thickness= 3/8"

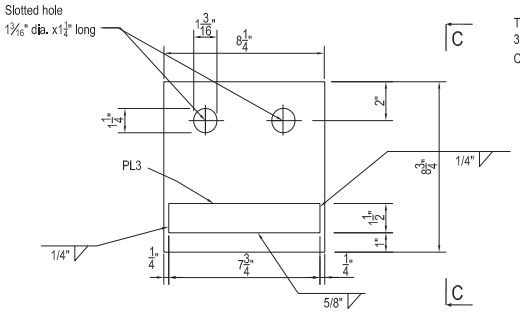

ASSEMBLY 3:
LOWER BINDING PLATE
WELDED TO PRIMARY PLATE

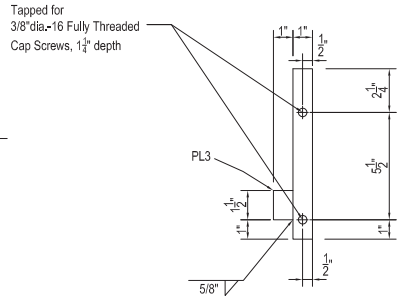

C-C

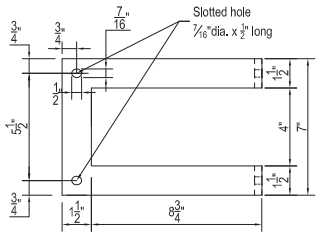

A-A

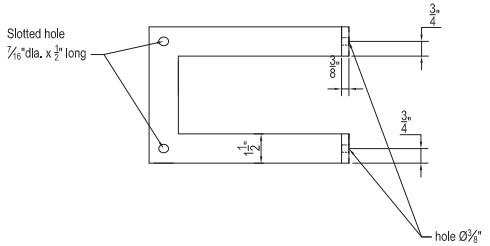

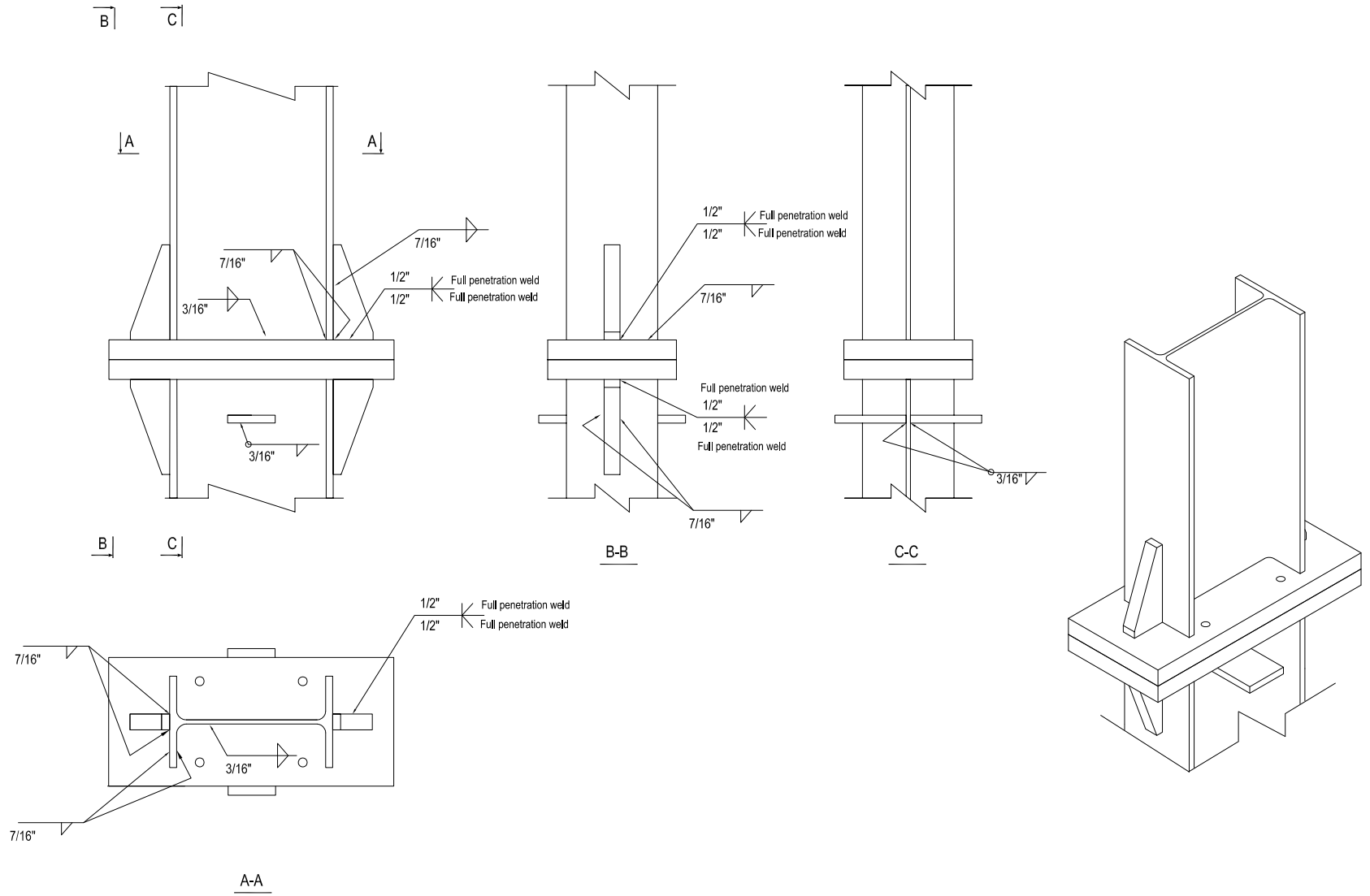
B
C
A
A
7/16"
7/16"
1/2"
1/2"
Full penetration weld
Full penetration weld
3/16"
3/16"
1/2"
1/2"
Full penetration weld
Full penetration weld
7/16"
Full penetration weld
1/2"
1/2"
Full penetration weld
7/16"
3/16"
B
C
B-B
C-C
1/2"
1/2"
Full penetration weld
Full penetration weld
7/16"
3/16"
7/16"
A-A

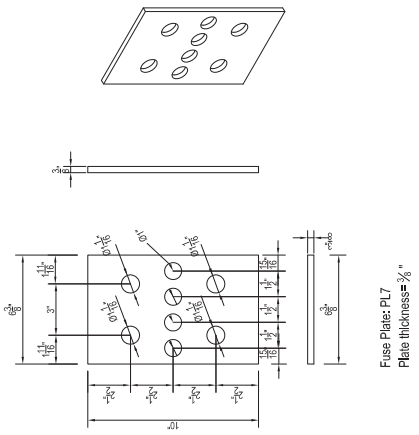
Fuse Plate: PL7
Plate thickness= ⅜"

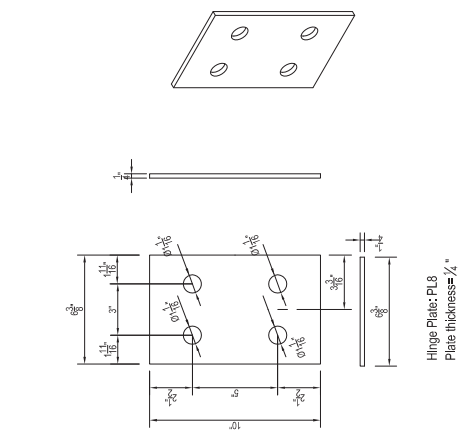
Hinge Plate: PL8
Plate thickness= ¼"

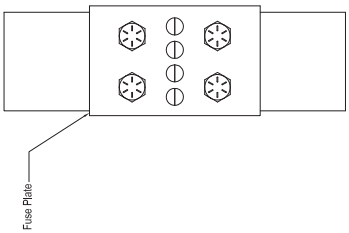
Fuse Plate

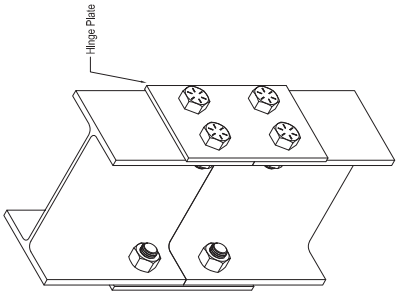
Hinge Plate

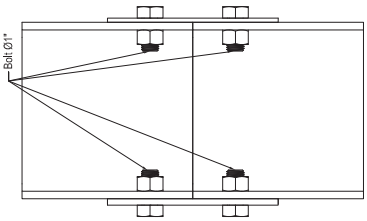
Bolt Ø1"

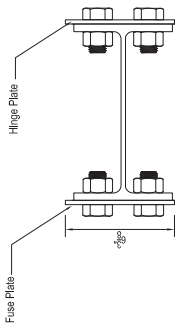
Hinge Plate
Fuse Plate

APPENDIX C:
STRUCTURAL DRAWINGS FOR
MEDIUM-CAPACITY BREAKAWAY CONNECTION SYSTEM

Presented in this appendix are structural drawings for the medium-capacity breakaway connection system developed and tested in this study.

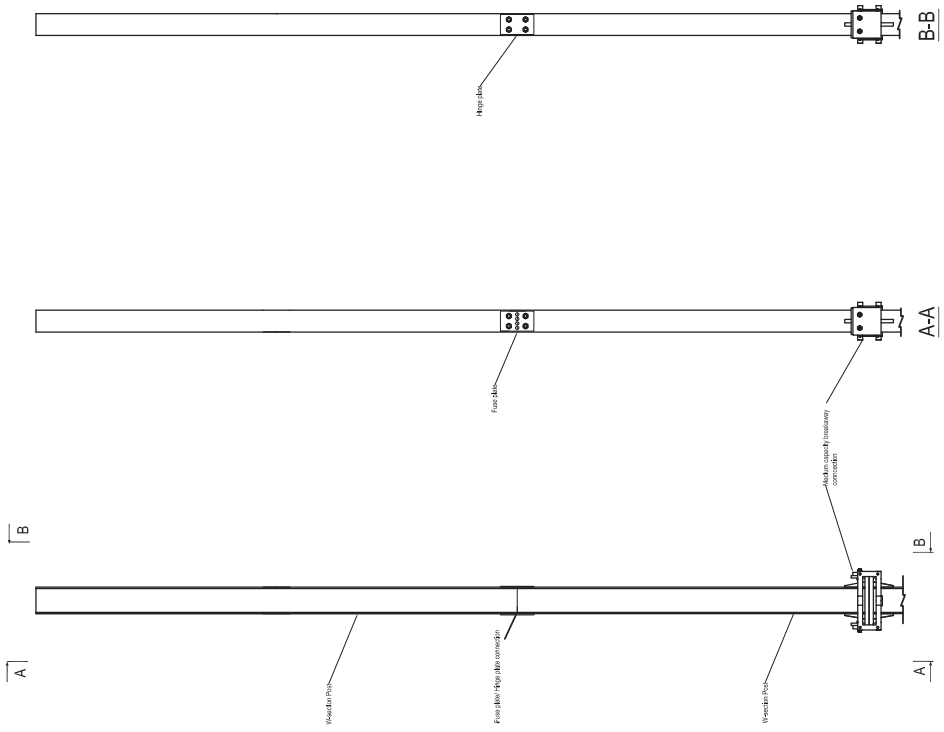
B-B
A-A
B
A
B
A

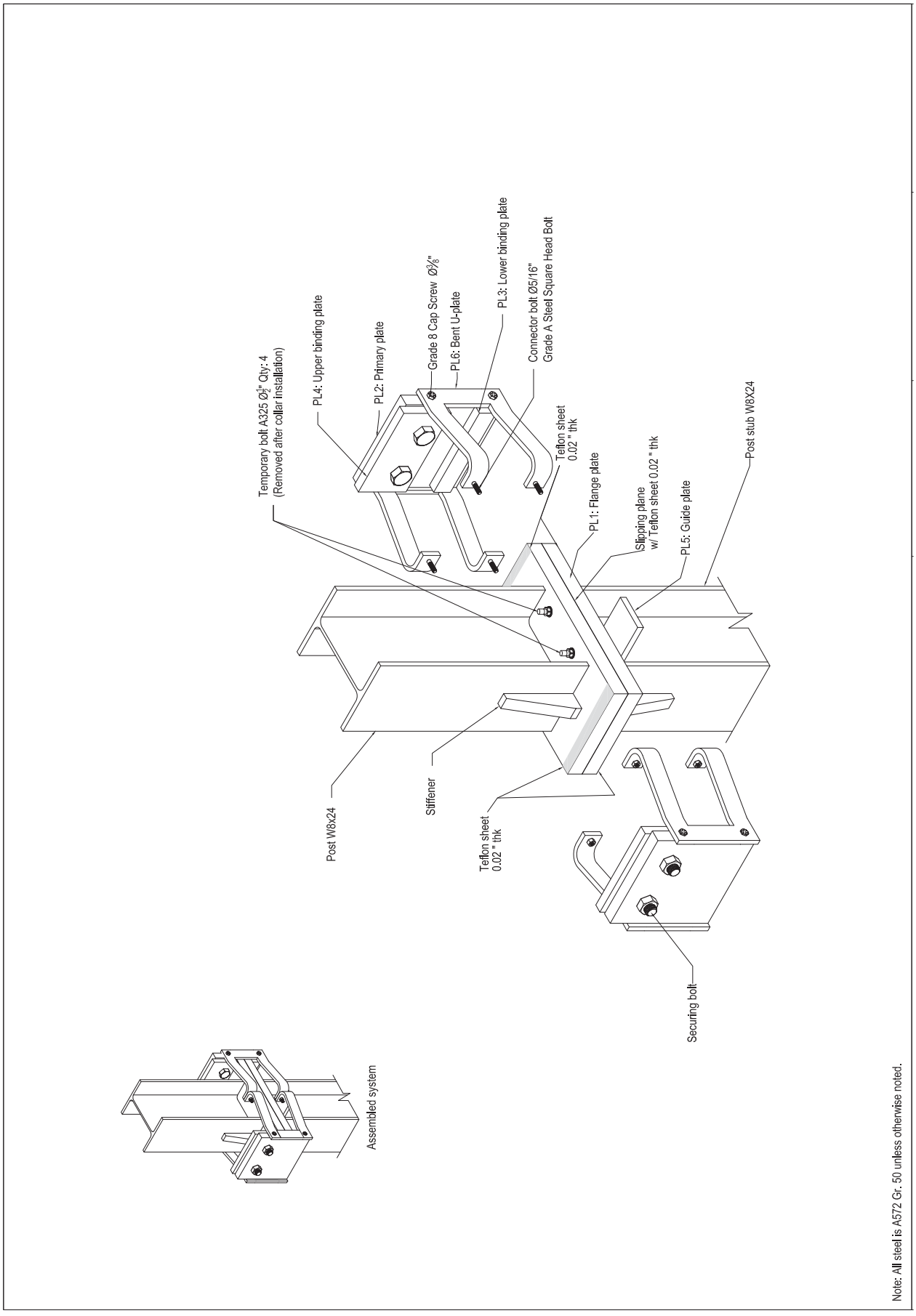
Temporary bolt A325 Ø3/4" Qty: 4
(Removed after collar installation)
PL4: Upper binding plate
PL2: Primary plate
Grade 8 Cap Screw Ø7/8"
PL6: Bent U-plate
PL3: Lower binding plate
Connector bolt Ø5/16"
Grade A Steel Square Head Bolt
Teflon sheet
0.02 " thk
PL1: Flange plate
Slipping plane
w/ Teflon sheet 0.02 " thk
PL5: Guide plate
Post stub W8X24
Post W8x24
Stiffener
Teflon sheet
0.02 " thk
Securing bolt
Assembled system
Note: All steel is A572 Gr. 50 unless otherwise noted.

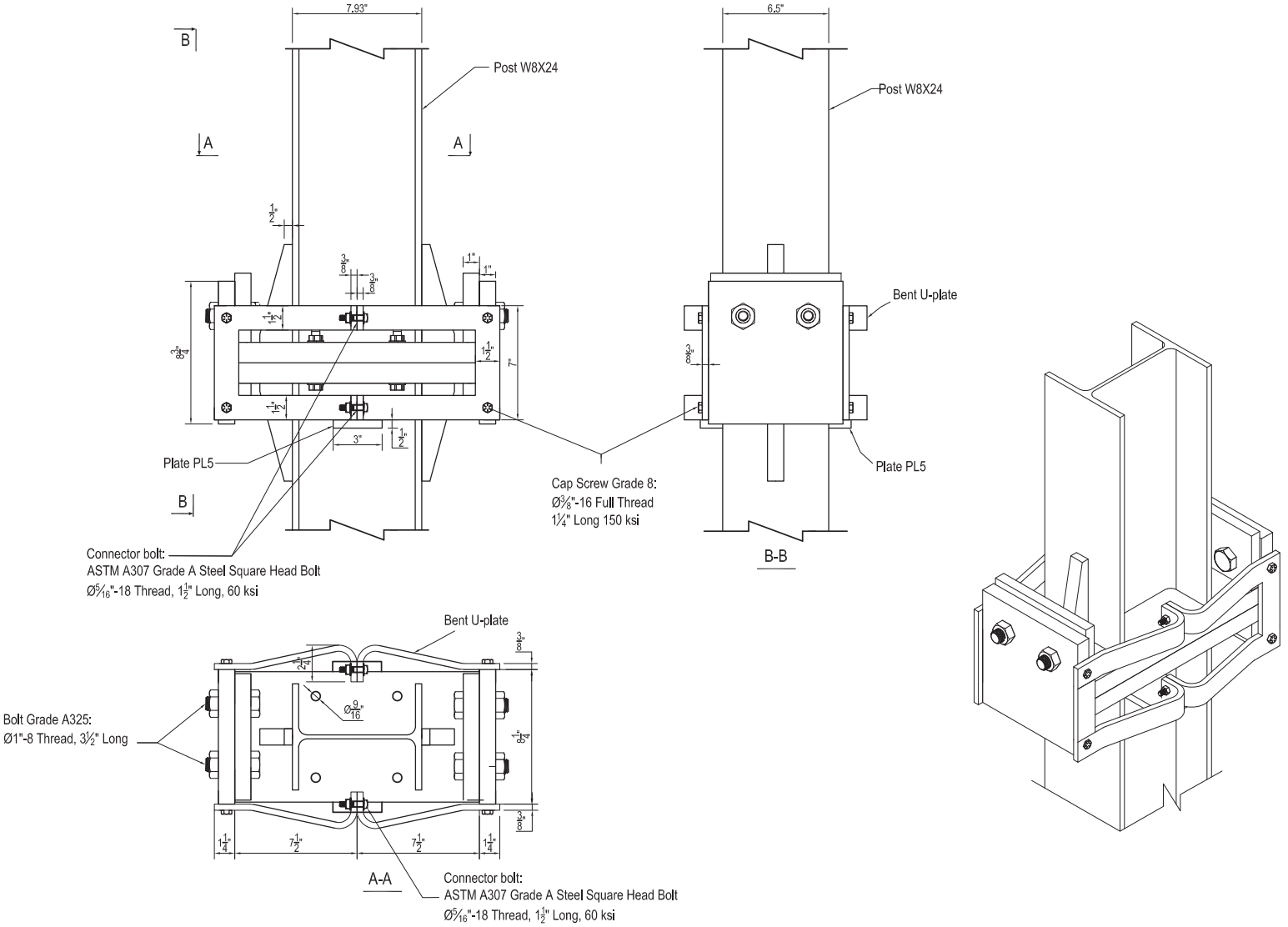
7.93"
6.5"
B
A
A
Post W8X24
Post W8X24
Bent U-plate
Plate PL5
Plate PL5
B
Cap Screw Grade 8:
Ø3/8"-16 Full Thread
1¼" Long 150 ksi
B-B
Connector bolt:
ASTM A307 Grade A Steel Square Head Bolt
Ø5/16"-18 Thread, 1½" Long, 60 ksi
Bent U-plate
Bolt Grade A325:
Ø1"-8 Thread, 3½" Long
A-A
Connector bolt:
ASTM A307 Grade A Steel Square Head Bolt
Ø5/16"-18 Thread, 1½" Long, 60 ksi

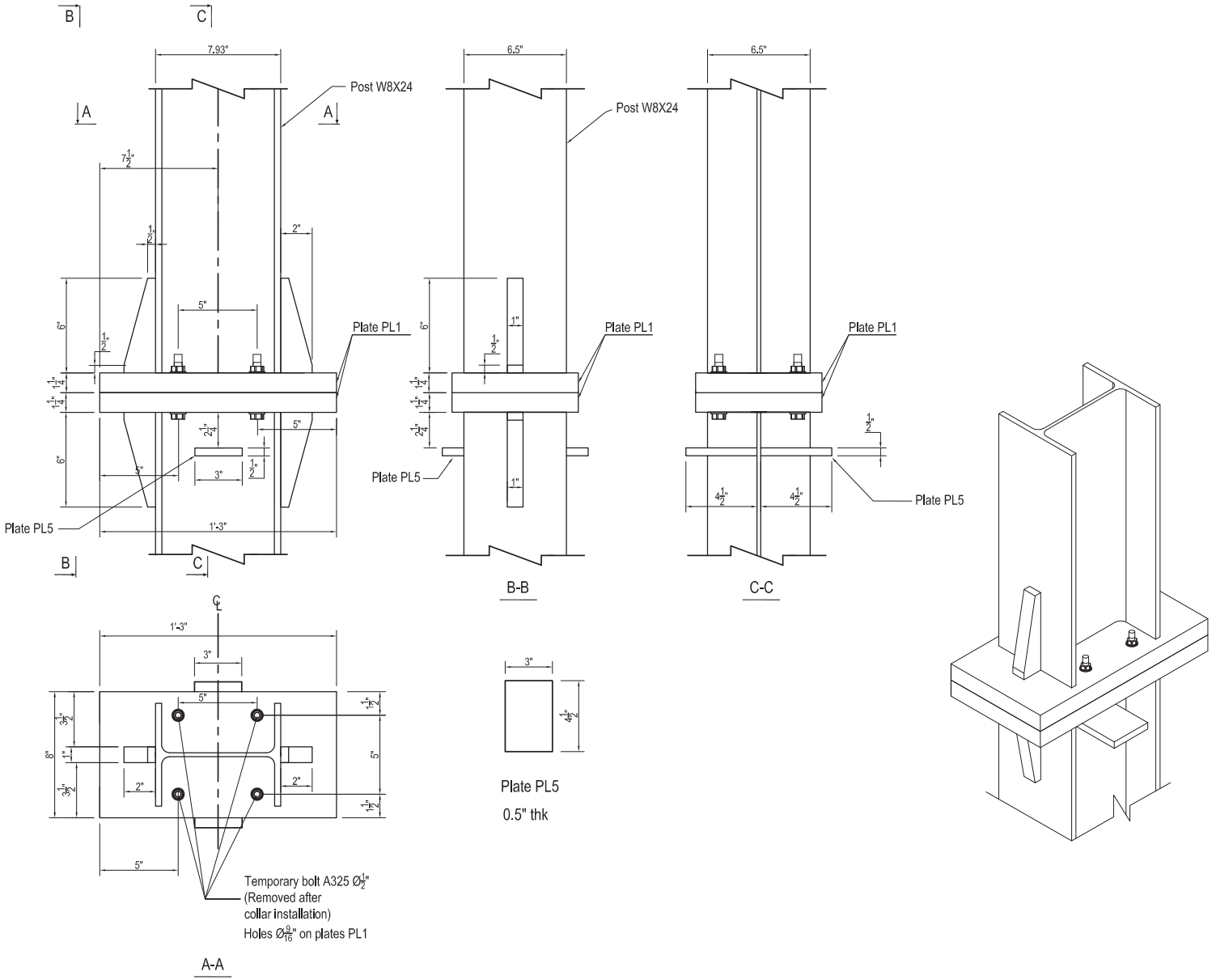
B
C
7.93"
Post W8X24
A
A
7½"
1½"
2"
5"
6"
½"
Plate PL1
1¼"
1¼"
2¼"
5"
6"
½"
5"
3"
Plate PL5
1'-3"
B
C
6.5"
Post W8X24
1"
½"
Plate PL1
Plate PL5
1"
B-B
6.5"
Plate PL1
1"
2
Plate PL5
4½"
4½"
C-A
1'-3"
3"
5"
3½"
1"
3½"
8"
2"
2"
5"
5"
Temporary bolt A325 Ø½"
(Removed after
collar installation)
Holes Ø9/16" on plates PL1
A-A
3"
4½"
Plate PL5
0.5" thk

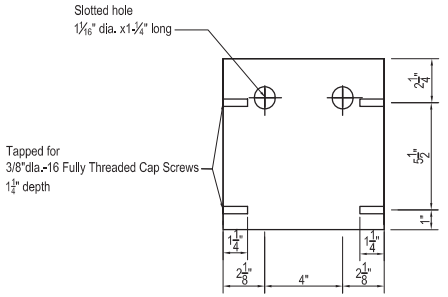

PRIMARY PLATE: PL2
Plate thickness= 1"

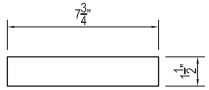

LOWER BINDING PLATE: PL3
Plate thickness= 1"

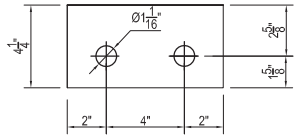

UPPER BINDING PLATE: PL4
Plate thickness= 1"

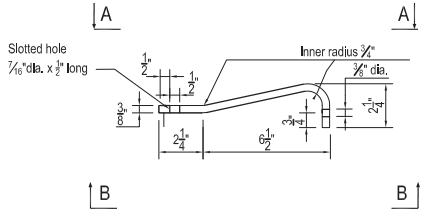

PLAN VIEW OF BENT U-PLATE: PL6
Plate thickness= 3/8"

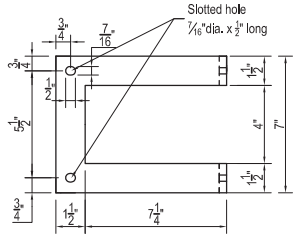

A-A

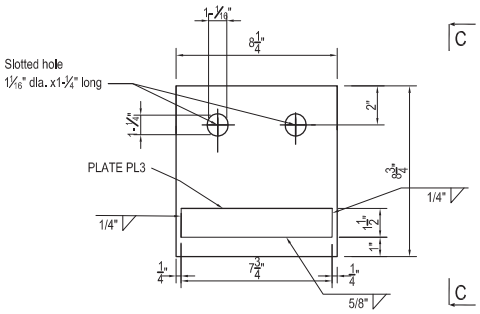

LOWER BINDING PLATE
WELDED TO PRIMARY PLATE

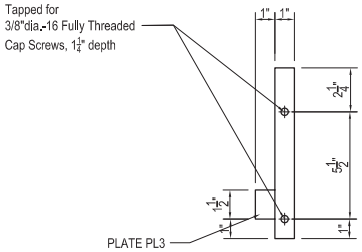

C-C

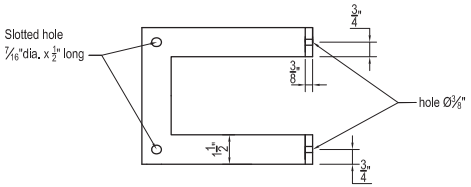

B-B

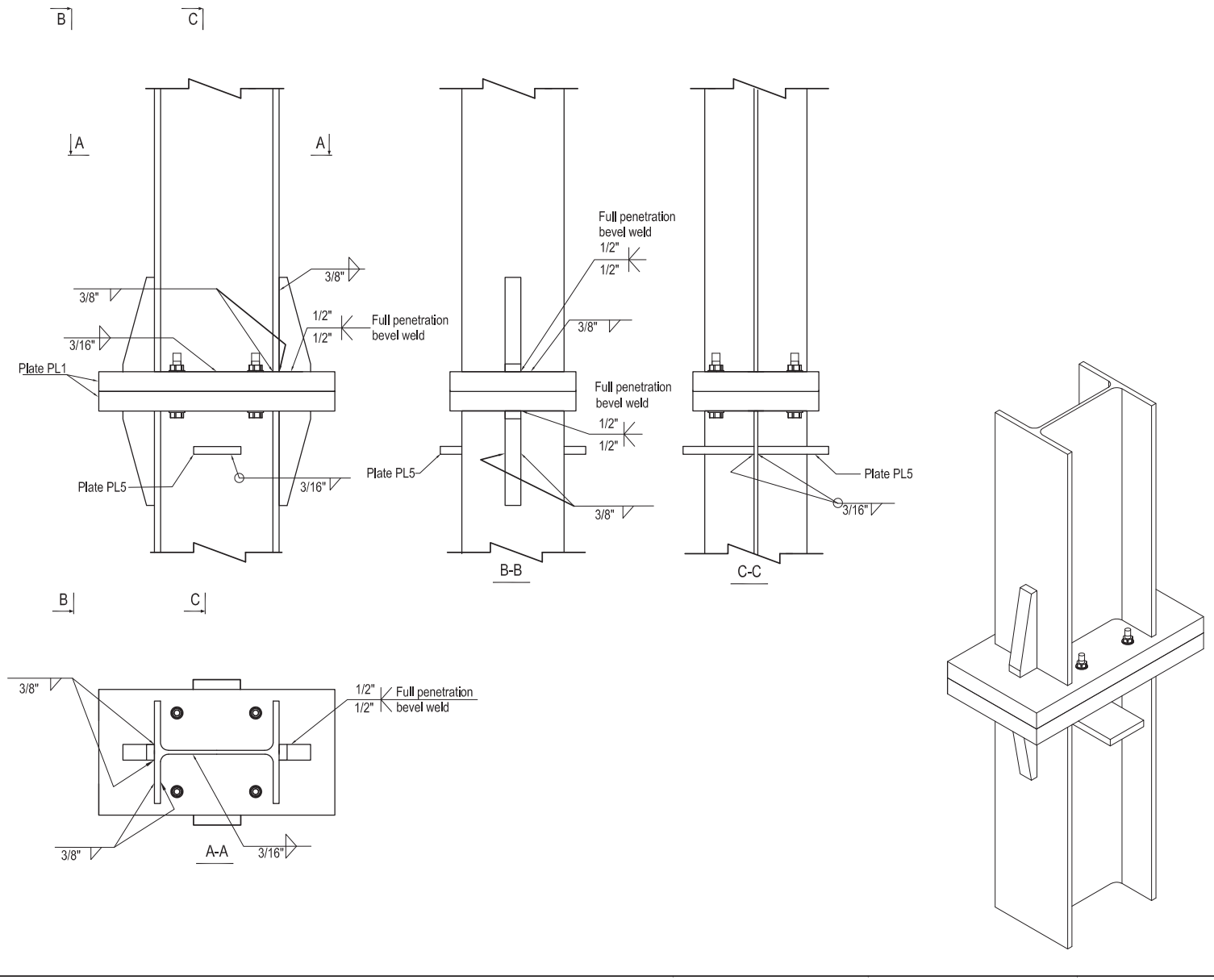
B
C
A
A
3/8"
3/8"
3/16"
1/2"
1/2"
Full penetration
bevel weld
Plate PL1
Plate PL5
3/16"
Full penetration
bevel weld
1/2"
1/2"
3/8"
Full penetration
bevel weld
1/2"
1/2"
Plate PL5
3/8"
B-B
Plate PL5
3/16"
C-C
B
C
3/8"
1/2"
1/2"
Full penetration
bevel weld
3/8"
3/16"
A-A

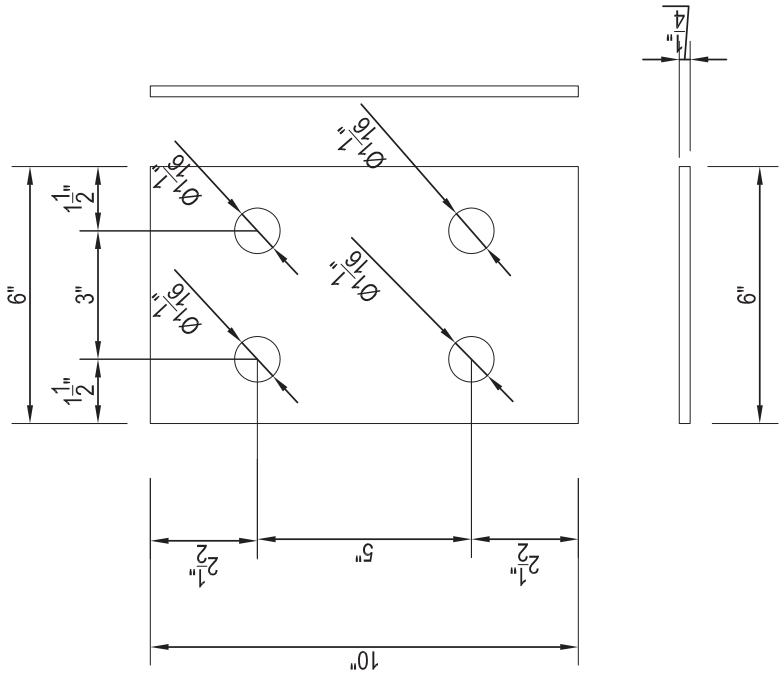

HINGE PLATE: PL8
Plate thickness= 1/4"

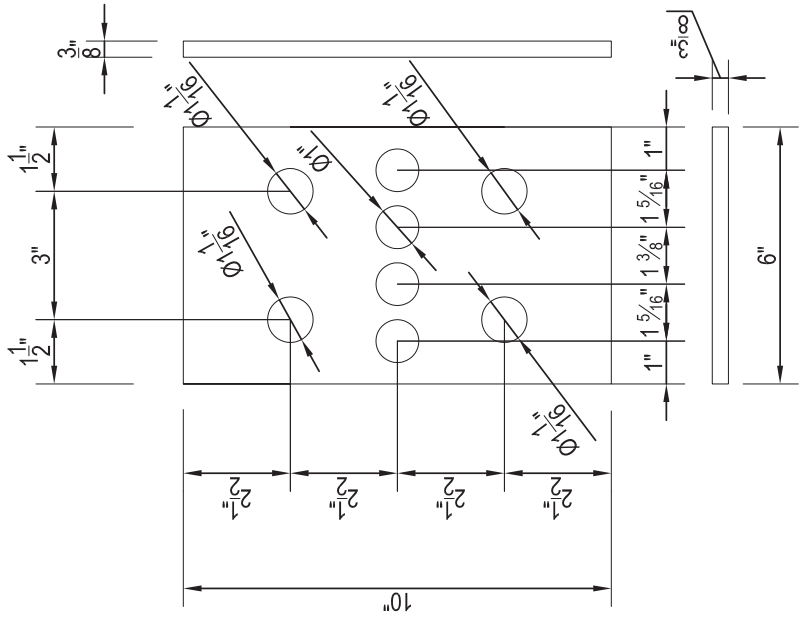

FUSE PLATE: PL7
Plate thickness= 3/8"

APPENDIX D:
STRUCTURAL DRAWINGS FOR
LOW-CAPACITY BREAKAWAY CONNECTION SYSTEM

Presented in this appendix are structural drawings for the low-capacity breakaway connection system developed and tested in this study.

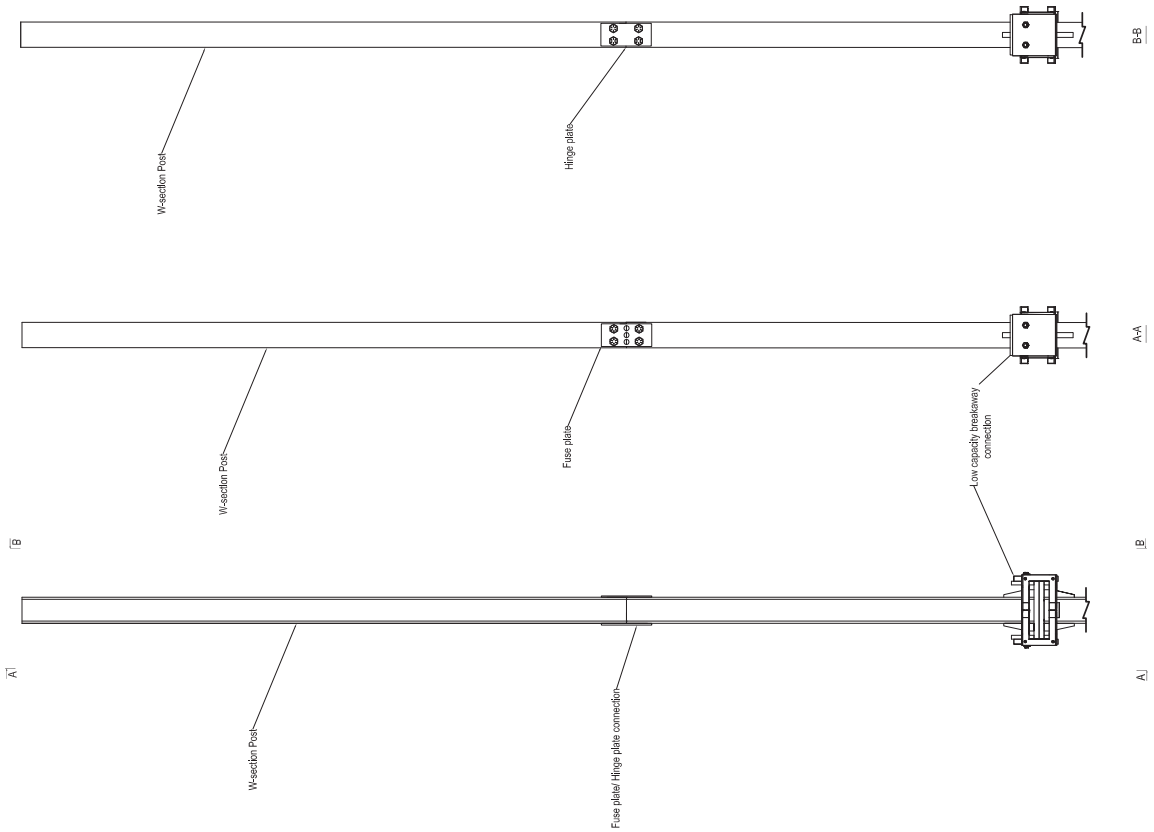
B-B
W-section Post
Hinge plate
A-A
W-section Post
Fuse plate
Low capacity breakaway connection
B
B
A
A
W-section Post
Fuse plate/ Hinge plate connection

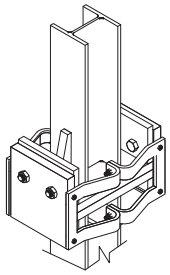

Assembled system

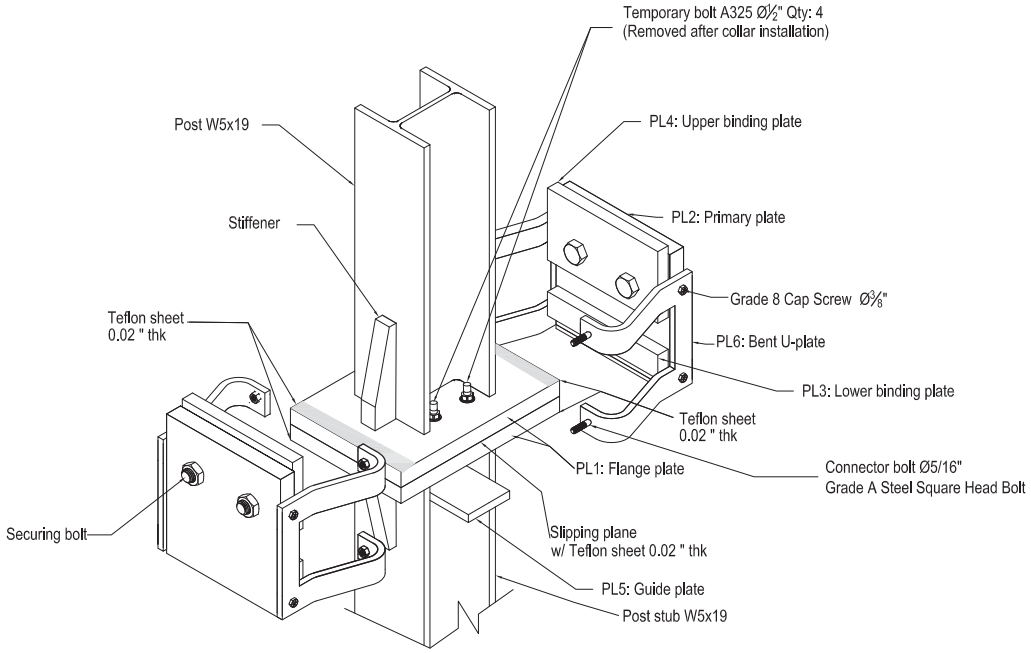

Note: All steel is A572 Gr. 50 unless otherwise noted.

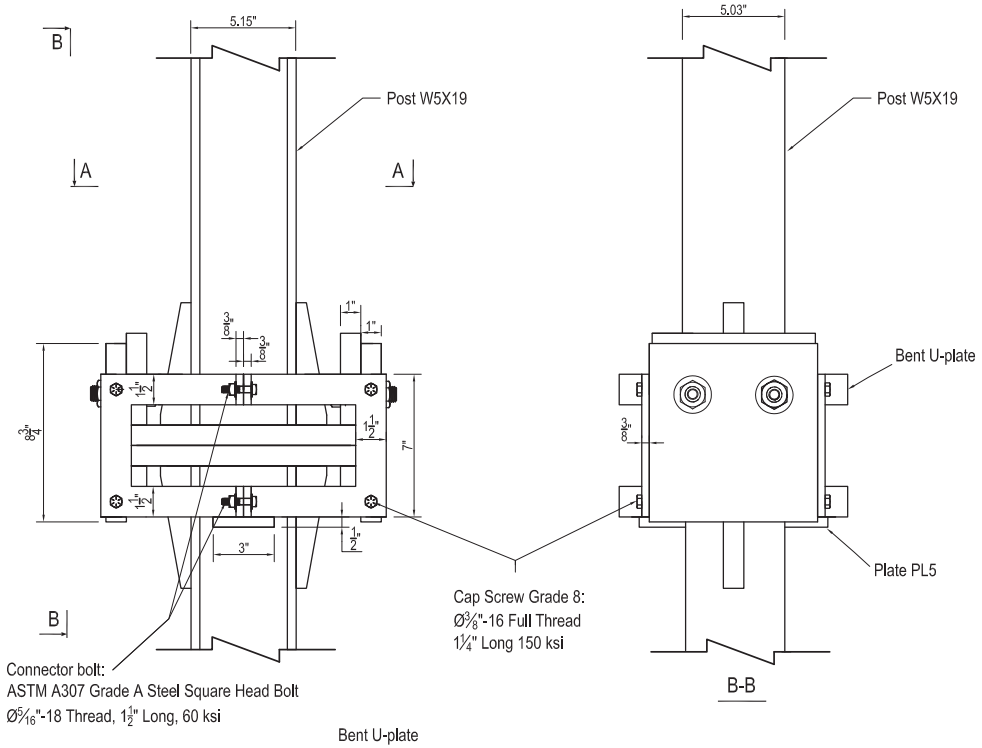
5.15"
B
Post W5X19
A
A
1"
1"
3"
7"
B
Connector bolt:
ASTM A307 Grade A Steel Square Head Bolt
Ø5⁄16"-18 Thread, 1½" Long, 60 ksi
5.03"
Post W5X19
Bent U-plate
Plate PL5
Cap Screw Grade 8:
Ø⅜"-16 Full Thread
1¼" Long 150 ksi
B-B

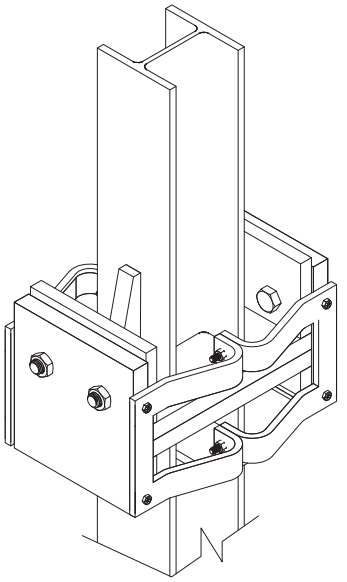

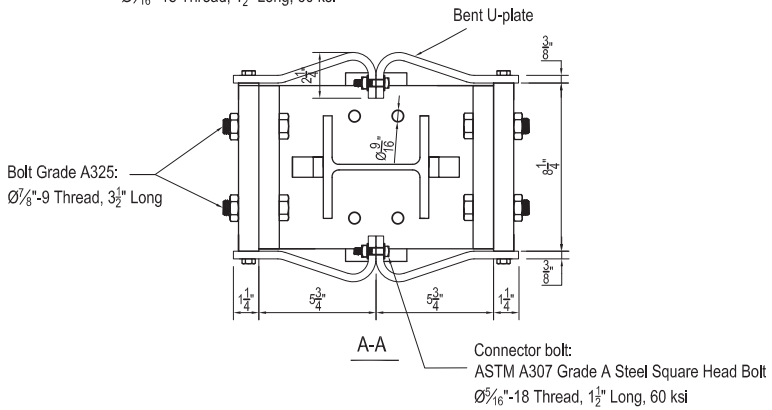
Bent U-plate
Bolt Grade A325:
Ø⅞"-9 Thread, 3½" Long
A-A
Connector bolt:
ASTM A307 Grade A Steel Square Head Bolt
Ø5⁄16"-18 Thread, 1½" Long, 60 ksi

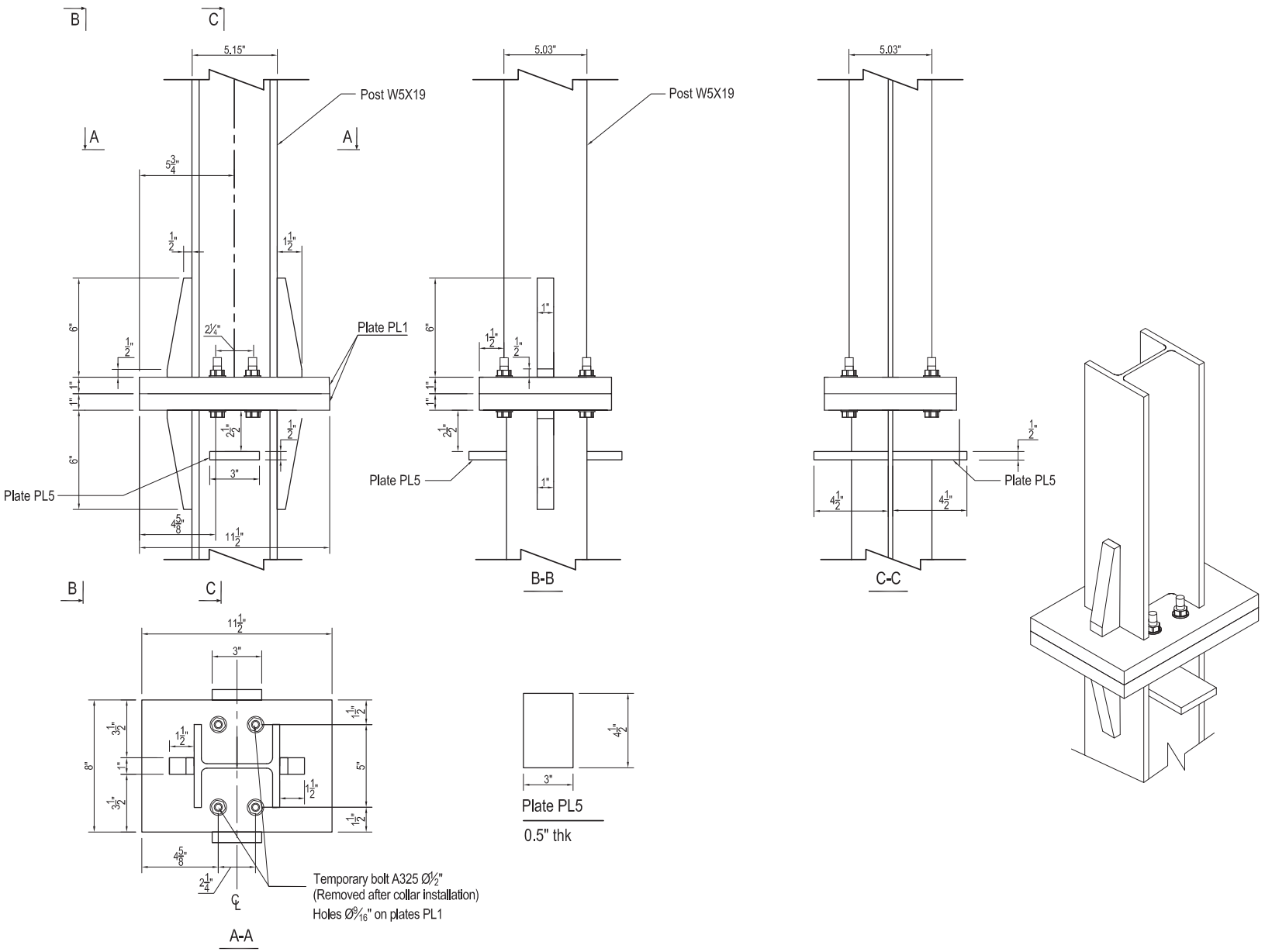
B
C
5.15"
Post W5X19
A
A
Plate PL1
Plate PL5
3"
5.03"
Post W5X19
Plate PL5
B-B
5.03"
Plate PL5
C-C
B
C
3"
Temporary bolt A325 Ø½"
(Removed after collar installation)
Holes Ø⁹⁄₁₆" on plates PL1
A-A
Plate PL5
0.5" thk

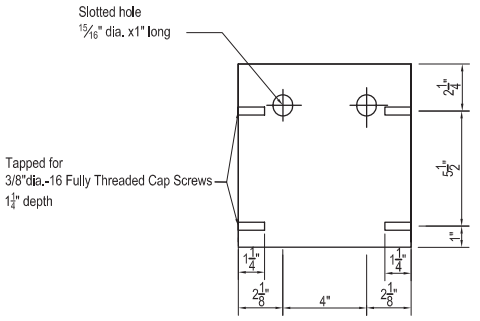

PRIMARY PLATE: PL2
Plate thickness= 1"

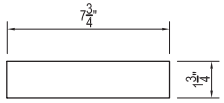

LOWER BINDING PLATE: PL3
Plate thickness= 1"

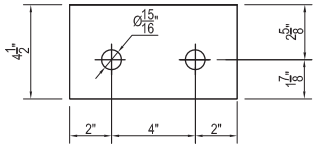

UPPER BINDING PLATE: PL4
Plate thickness= 1"

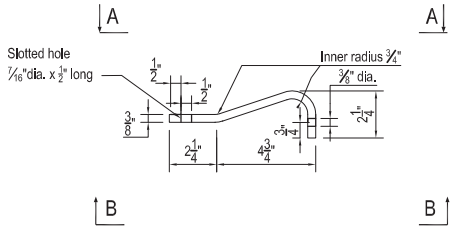

PLAN VIEW OF BENT U-PLATE: PL6
Plate thickness= 3/8"

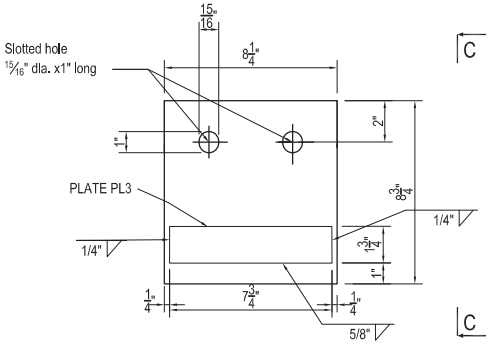

LOWER BINDING PLATE
WELDED TO PRIMARY PLATE

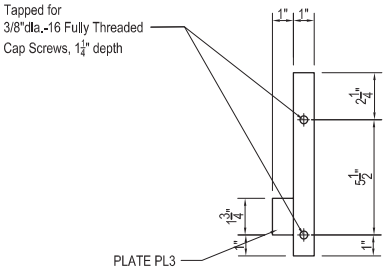

C-C

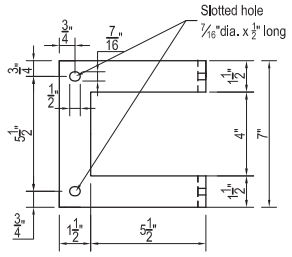

A-A

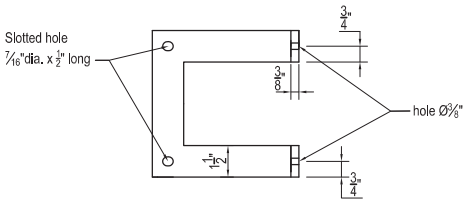

B-B

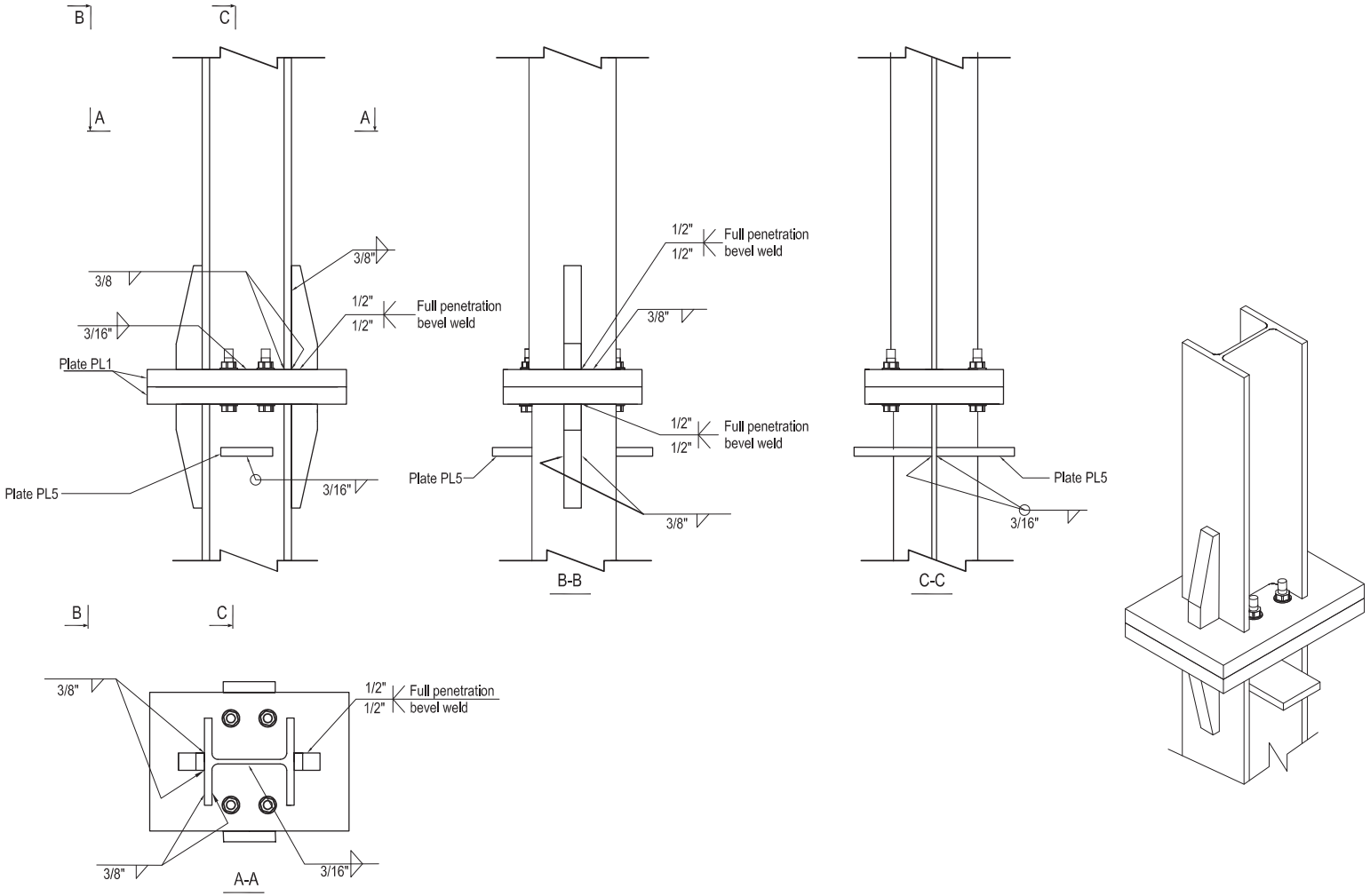
B
C
A
A
3/8"
3/8
1/2"
1/2"
Full penetration
bevel weld
3/16"
Plate PL1
Plate PL5
3/16"
1/2"
1/2"
Full penetration
bevel weld
3/8"
Plate PL5
1/2"
1/2"
Full penetration
bevel weld
3/8"
B-B
Plate PL5
3/16"
C-C
B
C
3/8"
1/2"
1/2"
Full penetration
bevel weld
3/8"
3/16"
A-A

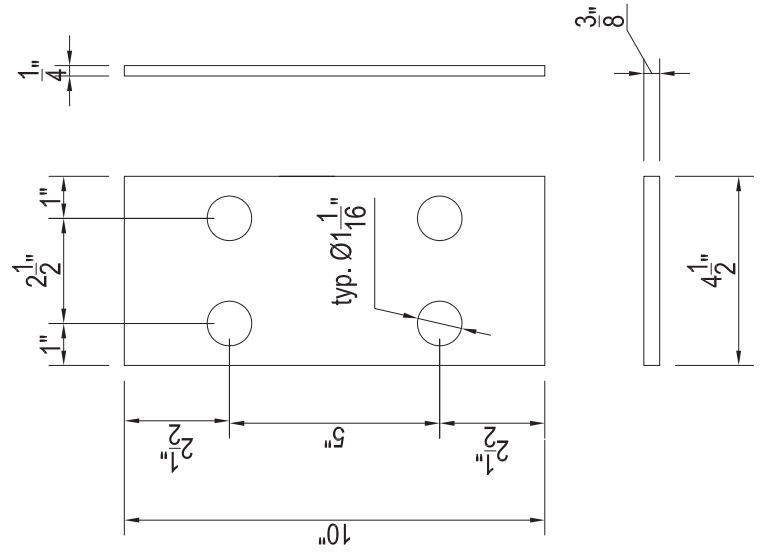

HINGE PLATE: PL8
Plate thickness= 1/4"

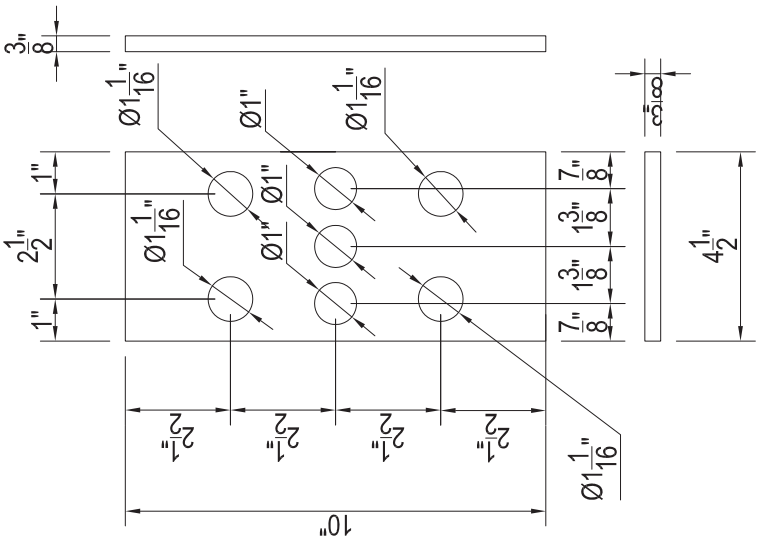

FUSE PLATE: PL7
Plate thickness= 3/8"

APPENDIX E:
STRUCTURAL DRAWINGS FOR
FUSE-PLATE AND HINGE-PLATE EXPERIMENTAL TEST SETUP

Presented in this appendix are structural drawings for the test setup that was used in this study to conduct isolated impact testing of a fuse-plate and hinge-plate assembly. The sizes of fuse-plate and hinge-plate tested corresponded to those that would be employed in a high-capacity breakaway connection system.

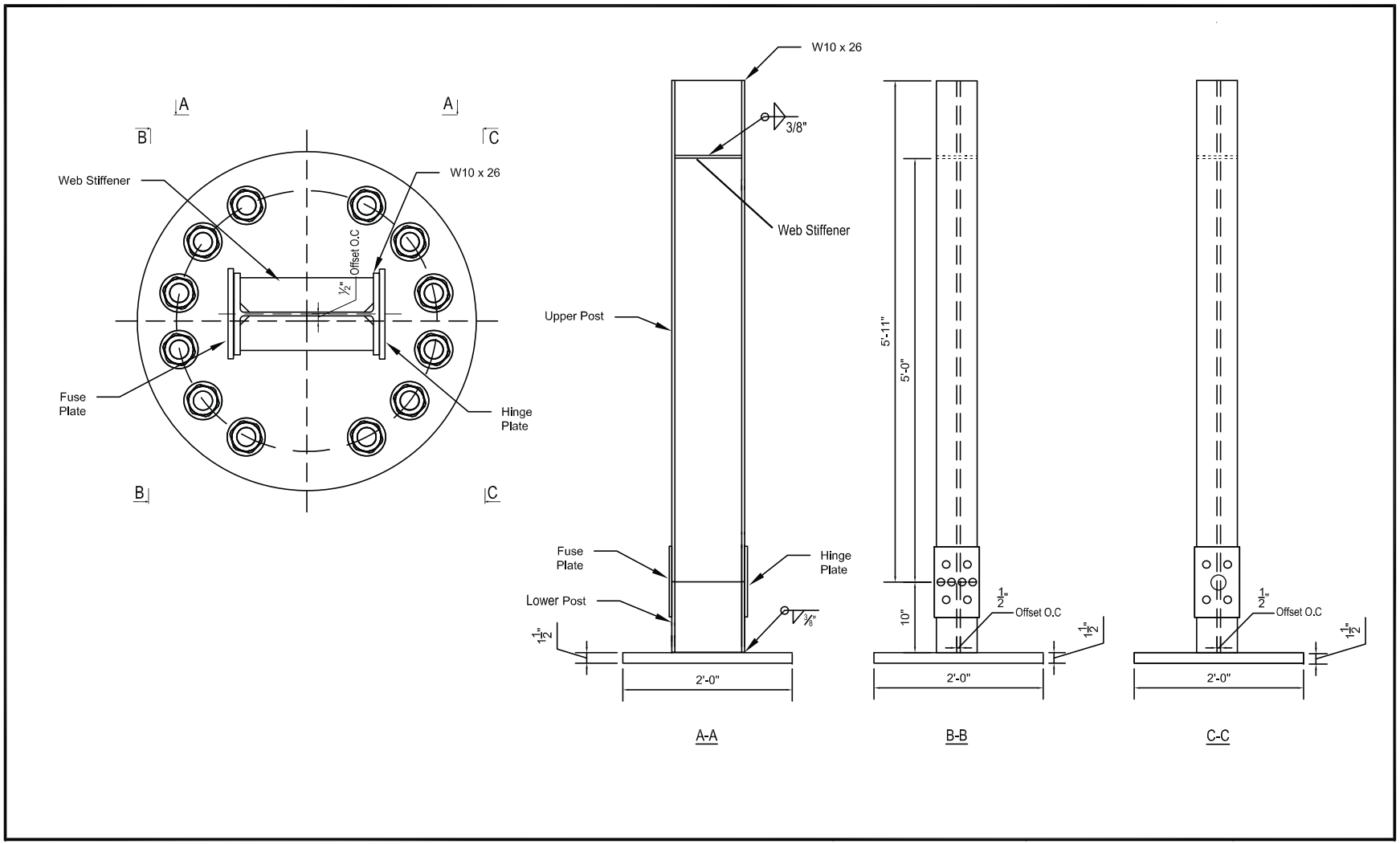
A
A
B
C
Web Stiffener
W10 x 26
Offset O.C
½"
Fuse Plate
Hinge Plate
B
C
W10 x 26
3/8"
Web Stiffener
Upper Post
Fuse Plate
Hinge Plate
Lower Post
1½"
2'-0"
A-A
5'-11"
5'-0"
10"
½"
Offset O.C
1½"
2'-0"
B-B
½"
Offset O.C
1½"
2'-0"
C-C

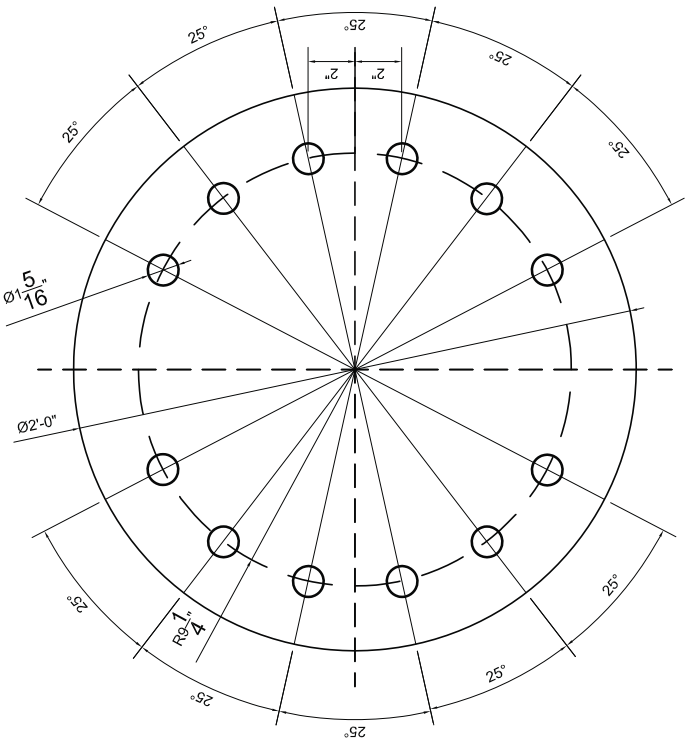

ROUND PLATE: PL1
1-1/2" thick

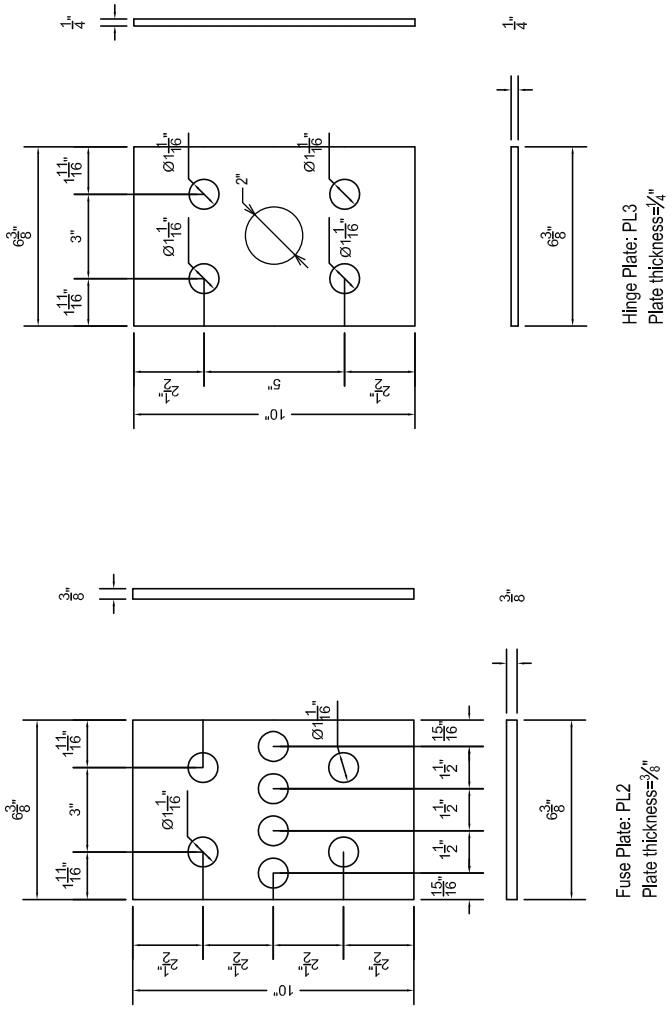
Hinge Plate: PL3
Plate thickness=¼"
Fuse Plate: PL2
Plate thickness=⅜"

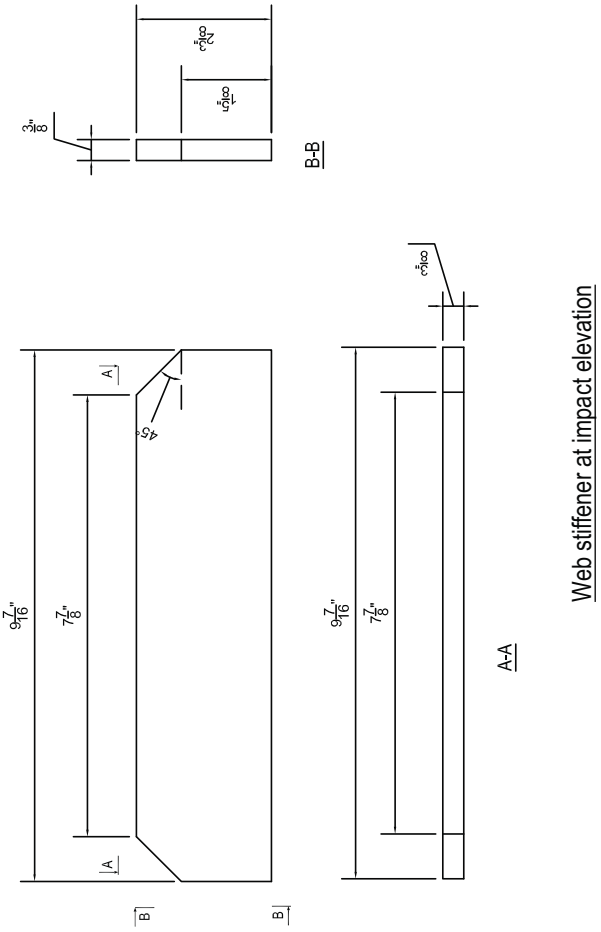

Web stiffener at impact elevation